2012

Particle interaction and rheological behavior of cement-based materials at micro- and macro-scales

Gilson Lomboy
Iowa State University

Particle interaction and rheological behavior of cement-based materials at micro- and macro-scales

by

Gilson Rescober Lomboy

A dissertation submitted to the graduate faculty

in partial fulfillment of the requirements for the degree of

DOCTOR OF PHILOSOPHY

Major: Civil Engineering (Civil Engineering Materials)

Program of Study Committee:
Kejin Wang, Major Professor
Vernon Schaefer
Shankar Subramaniam
Sriram Sundararajan
R. Christopher Williams

Iowa State University

Ames, Iowa

2012

TABLE OF CONTENTS

LIST OF FIGURES

LIST OF TABLES

ABSTRACT

Rheology of cement based materials is controlled by the interactions at the particle level. The present study investigates the particle interactions and rheological properties of cement-based materials in the micro- and macro-scales. The cementitious materials studied are Portland cement (PC), fly ash (FA), ground granulated blast furnace slag (GGBFS) and densified silica fume (SF).

At the micro-scale, aside from the forces on particles due to collisions, interactions of particles in a flowing system include the adhesion and friction. Adhesion is due to the attraction between materials and friction depends on the properties of the sliding surfaces. Atomic Force Microscopy (AFM) is used to measure the adhesion force and coefficient of friction. The adhesion force is measured by pull-off force measurements and is used to calculate Hamaker constants. The coefficient of friction is measured by increasing the deflection set-points on AFM probes with sliding particles, thereby increasing normal loads and friction force. AFM probes were commercial Si_3N_4 tips and cementitious particles attached to the tips of probe cantilevers. SF was not included in the micro-scale tests due to its limiting size when attaching it to the AFM probes. Other materials included in the tests were silica, calcite and mica, which were used for verification of the developed test method for the adhesion study. The AFM experiments were conducted in dry air and fluid environments at pH levels of 7, 8, 9, 11 and 13. The results in dry air indicate that the Hamaker constant of Class F FA can be similar to PC, but Class C FA can have a high Hamaker constant, also when in contact with other cementitious materials. The results in fluid environments showed low Hamaker constants for Class F fly ashes compared to PC and also showed high Hamaker constants for PC and Class C fly ash. The results for the friction test in dry air indicated that the coefficient of friction of PC is lower than fly ashes, which is attributed to the asperities present on the particle surface.

At the macro-scale, flow of cementitious materials may be in its dry or wet state, during transport and handling or when it is used in concrete mixtures, respectively. Hence, the behavior of bulk cementitious materials in their dry state and wet form are studied. In the

dry state, the compression, recompression and swell indices, and stiffness modulus of plain and blended cementitious materials are determined by confined uniaxial compression. The coefficients of friction of the bulk materials studied are determined by a direct shear test. The results indicate that shape of particles has a great influence on the compression and shear parameters. The indices for PC blends with FA do not change with FA replacement, while it increases with GGBFS replacement. Replacement with GGBFS slightly decreases coefficient of friction, while replacement with FA significantly decreases coefficient of friction. At low SF replacement, coefficient of friction decreases. In wet state, unary, binary, ternary and quaternary mixes with w/b of 0.35, 0.45 and 0.55 were tested for yield stress, viscosity and thixotropy. It is found that fly ash replacement lowers the rheological properties and replacement with GGBFS and SF increases rheological properties.

The distinct element method (DEM) was employed to model particle interaction and bulk behavior. The AFM force curve measurement is simulated to validate the adhesion model in the DEM. The contact due to asperities was incorporated by considering the asperities as a percentage of the radius of the contacting particles. The results of the simulation matches the force-curve obtained from actual AFM experiments. The confined uniaxial compression test is simulated to verify the use of DEM to relate micro-scale properties to macros-scale behavior. The bulk stiffness from the physical experiments is matched in the DEM simulation. The particle stiffness and coefficient of friction are found to have a direct relation to bulk stiffness.

CHAPTER 1. INTRODUCTION

1.1. Background

Concrete workability is the ease of placing, consolidating and finishing fresh concrete and the degree to which it resists segregation. Desirable workability in concrete is essential in every step of a project, from manufacturing to transportation to construction. Sufficient workability contributes to proper construction, which has an impact to the long-term performance of hardened concrete. In recent years, concrete technology has advanced dramatically due to the use of numerous supplementary cementitious materials and chemical admixtures as well as the development of various new types of concretes, such as self-consolidating concrete and high performance concrete. Demands for rapid construction, high performance, and excellent durability of concrete have been increasing. As a result, there is a need for the measurements, predictions, and acceptances of flow or rheological behavior of various concretes.

The rheology of cement-based materials is the quantitative property that describes the mixture's deformation and flow. Recent research has demonstrated that rheology characterization allows researchers and engineers to have a fundamental understanding of cement-based material flow behavior, to formulate optimal mix design, and to control mixture homogeneity during the manufacturing and construction processes (Sobolev, 2004). Characterization and control of cement-based material rheological behavior is becoming a powerful tool for the concrete industry.

The rheological behavior of a cement-based material is strongly influenced by interparticle forces and spatial particle distribution. At present, there is a wide variation in most results from experimental studies on cement and concrete rheological behavior vary largely because of different materials investigated, equipment used, and test methods applied (Banfill, 2003). In practice, prediction of concrete rheological behavior largely depends on the results of trial and error tests and the field engineer's experience and judgment. Besides being time-consuming and expensive, such an experimental approach is also not reliable

because of the complexities of the materials and experiments. An alternative approach is to develop computational tools for predictive simulation.

In the particles suspension simulation, cement-based materials (such as paste, mortar, and concrete) are commonly considered as a two-phase material that contains a group of rigid particles suspended in a fluid matrix, and continuum approaches and other theoretical concepts (such as fluid dynamics, double-layer theory, particle collision and packing theories, etc.) can be applied (Lu et al., 2008). Nevertheless, most of these theoretical approaches do not permit researchers to understand the concrete flow at an individual particle level, thus limiting improvements in concrete mix design. In discrete particle simulation, the bulk behavior of concrete flow is described by the characteristics of individual particles and the interactions between the particles. Numerical modeling based on the discrete element method (DEM) is often used to obtain such microscopic information of the individual particles, for which conventional experimental techniques and other simulations are rarely practical (Cundall and Strack, 1979). The behavior of a DEM model largely depends on the particle contact mechanics, particle shape and size distribution. Although previous DEM simulations have demonstrated their ability to describe the overall flow behavior of a fresh mortar or concrete mixture, the flow behavior of the materials at a micro- or nano-scale level, such as the forces generated in the mortar or concrete system during the aggregate particle approach, contact, and separation, has not been well understood. More importantly, the underlying assumptions for the particle movements in the material system have not been clarified.

To address the above-mentioned concerns, an innovative solution is needed for optimizing and predicting concrete rheological behavior rationally and effectively. Since the behavior of cement-based materials is determined by the complex interplay of inter-particle forces and spatial particle distribution, a predictive model that incorporates the fundamental physical interactions of the materials is essential. Here, a multi-scale, multiphase approach is conducted to study the rheological parameter and behavior of cement based materials.

1.2. Objectives

The goal of this study is obtain a better understanding of the flow behavior of cement-based materials through multi-scale and multiphase experiments and modeling. The objectives of the present research are:

(1) Utilize atomic force microcopy (AFM) experiments to measure interparticle interactions in cementitious materials.

(2) Study the rheological properties of bulk cementitious materials in their dry state and wet form.

(3) Study rheological behavior of bulk cementitious materials using the distinct element method (DEM) with micro-scale data obtained from AFM experiments as input parameters

1.3. Research Approach

The outline of the research is shown in Figure 1.1. The research was divided into three parts. The first part was the study of the micro-scale properties of cement-based materials using AFM. The adhesion forces and Hamaker constants of cementitious materials were measured in dry air, water and sodium hydroxide solution with pH 8, 9, 11 and 13. The coefficients of friction between cementitious materials were also measured in different dry and fluid environments.

The second part was the study of the macro-scale behavior of cementitious materials in dry state and paste form. The bulk stiffness and coefficient of friction were determined in their dry state, by uniaxial compression and direct shearing. In paste form, the viscosity, yield stress and thixotropy were studied. The cementitious materials used in the study were ordinary Portland cement, fly ash, ground granulated blast furnace slag and densified silica fume.

The third part of the study was the simulation of bulk behavior using the micro-scale properties as input parameter. The simulations were carried out using the distinct element method. Simulations were done on single particle adhesion by AFM pull-off deflection and compression to determine bulk behavior.

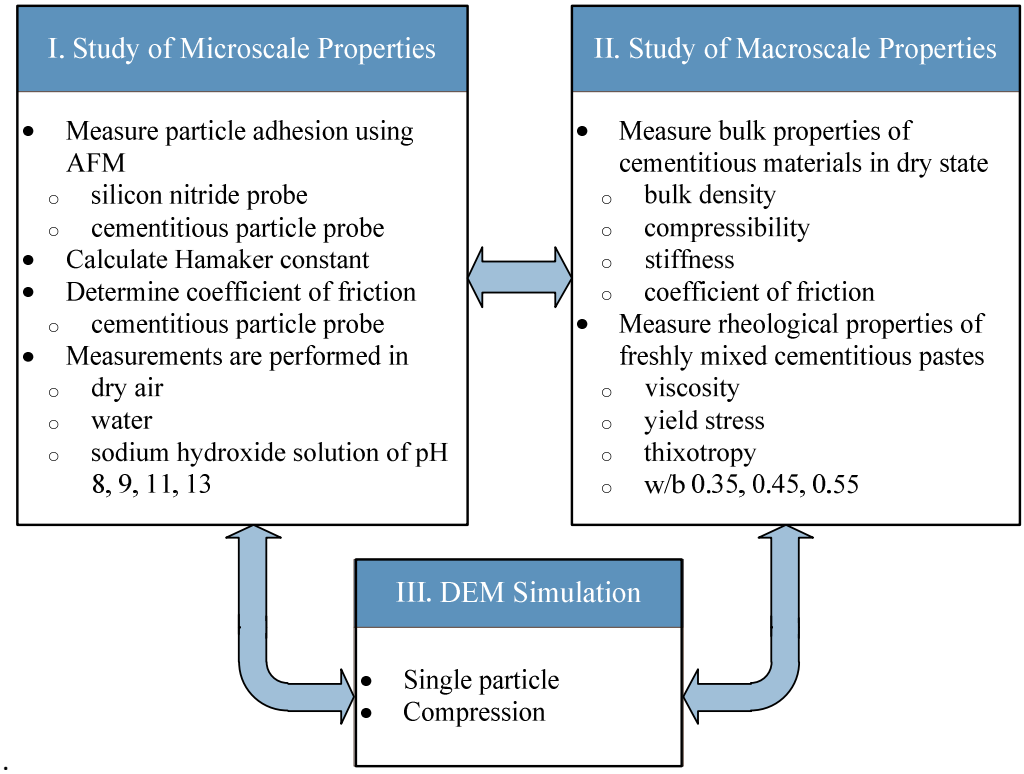

Figure 1.1. Outline of research and interrelations of objectives

1.4. Dissertation Organization

This dissertation is divided into six chapters. Chapter 1 provides the background, objectives and the research approach. Chapter 2 is the review of literature. The chapter is divided into three sections: micro-scale properties of cementitious materials that affect rheology, macro-scale rheological properties of cement-based materials, and simulation of cement-based materials using DEM.

Chapter 3 covers test methods and results of the micro-scale studies using AFM with cementitious particles. The studies were on adhesion and friction of cementitious particles in dry air and aqueous environments. In the adhesion force measurements, the Hamaker constants were computed from the pull-off forces using appropriate contact mechanics models, and considering particle asperities and double layer effects. The coefficients of friction between cementitious particles were determined in the friction studies. The results were discussed based on known theoretical quantities, testing condition and rheological implications.

Chapter 4 presents the macro-scale testing and properties of bulk cementitious materials in dry state and paste form. The methods adopted for compression testing in dry state and shear testing in dry and wet state of bulk samples are presented. In the compression tests, the bulk density, void ratio, compression, swell and recompression indices and bulk stiffness were determined. In the shear testing of dry powders, the coefficients of friction were determined. While in paste form, the viscosity, yield stress and thixotropy were measured. The test results in dry state and in paste form are discussed and compared. Statistical models of the rheological properties of pastes are also presented.

Chapter 5 presents the DEM simulation of cementitious materials. The modeling conditions, assumptions and input data are discussed. The modeling of AFM pull-off deflection is presented as verification of cohesion implementation in the DEM program. Simulations of compression and its relation to experimental results are discussed.

Finally, Chapter 6 provides a summary of this research, overall conclusions and provides recommendations for future research.

CHAPTER 2. REVIEW OF LITERATURE

2.1 Atomic Force Microscopy Cement-based Materials

AFM is a powerful tool to image surface topography. It has been increasingly used on surface imaging of cementitious particles (Demanet, 1995, Bosbach and Enders, 1997, Mishraa et al., 2003) and cement hydration and microstructure evolution (Mitchell et al., 1996, Yang, et al., 2002, 2003, Papadakis, et al., 1999, Mondal, et al., 2006). For the study of the rheology of cement-based materials at the micro-scale, the following subsections focuses on measurement of adhesion and friction forces with AFM.

2.1.1 Adhesion Forces Measurement with AFM

AFM is also used for measurement of force-distance curves and adhesion force between materials at different ambient conditions (Cappella and Dietler, 1999, Butt, et al. 2005). A few researchers have attempted to measure adhesion forces and Hamaker constant of cement-based materials. Uchikawa, et al. (1997) determined the steric repulsive force between polished clinker and silicon in solutions with different admixtures. They found that the fluidity of fresh cement pastes was correlated to the repulsive forces of their particles. Kauppi, et al. (2005) measured the interaction forces between spherical and flat MgO particles using an AFM in a solution containing superplasticizer. They discovered that superplasticizers contributed to both electrostatic and steric repulsion. Lesko, et al. (2001) and Plassard, et al. (2005) evaluated the forces between calcium silicate hydrate (C-S-H) layers in different solutions. They reported that in the solution similar to the pore solution of a cement paste, the adhesion force between C-S-H layers was approximately 30 MPa and the force increased with increasing calcium concentration.

Force measurements are performed by acquiring force-distance curves using the AFM (Butt, et al., 2005). A schematic of a typical force-distance curve is shown in Figure 2.1. In a typical measurement, the tip (at the end of the probe) is initially held far from the sample (a). It is then brought into contact with the stationary sample using a piezo-motor. As the probe approaches the sample, the attractive force gradient of the probe-sample interaction exceeds

the normal spring constant at a location close to contact. This causes an instability whereby the probe tip snaps into contact with the sample and probe is seen to deflect past the "zero force" level (b). As the probe continues to advance, it presses on the sample and further deflects to its maximum value (c). Subsequently, the probe is retracted or "withdrawn" away from the sample. During this process, the probe keeps in contact with the sample (d) until the spring constant overcomes the attractive force gradient that results in the cantilever "snapping back" to its undeflected position (e). The deflection of the probe (and hence the force obtained by multiplying deflection with probe normal stiffness) is continuously recorded as a function of piezo displacement.

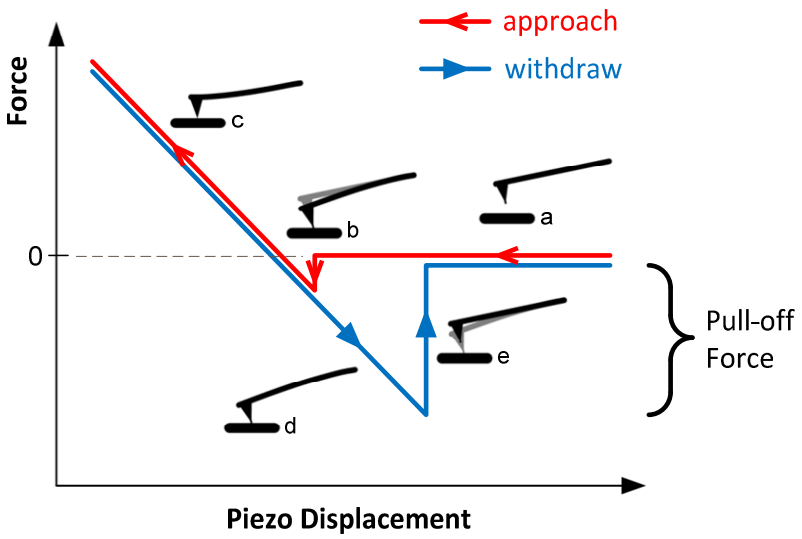

Figure 2.1. Sketch of a typical force curve

The pull-off force (F) between the two materials tested is calculated from the cantilever pull-off deflection (δ) and normal stiffness (k) as:

$$F = k\delta \tag{2.1}$$

The pull-off deflection, as indicated in Figure 2.1 is the distance from the initial/neutral position of the probe to the of the probe tip-sample separation.

The pull-off force (F) evaluated from the experiment computed by equation (2.2) may be expressed in terms of work of adhesion (W) of the interface and AFM probe tip radius (R). Work of adhesion is the decrease in free energy per unit area when an interface is formed from two individual surfaces 1 and 2. Depending on the stiffness of the material, the JKR model (Johnson, et al., 1971) or DMT (Derjaguin, et al., 1975) for a spherical particle in contact with a plane surface applies. The JKR and DMT models are expressed as

$$F = c\pi R W_{12} \tag{2.2}$$

The constant c is 3/2 for the JKR model and is 2 for the DMT model. The work of adhesion can be expressed as a function of Hamaker constant (A_{12}) between two contacting bodies and cut-off distance (D_0). The cut-off distance is the interfacial separation between two contacting materials (Israelachvili, 1991).

$$W_{12} = \frac{A_{12}}{12\pi D_0^2} \tag{2.3}$$

The application of the two models is usually chosen based on the Tabor parameter (μ_T) (Tabor, 1977). The parameter is a function of the probe tip radius, adhesion energy (γ_{12}), cut-off distance, elastic modulus of the contacting materials (E) and Poisson's ratio (ν).

$$\mu_T = \left[\frac{R\ \gamma_{12}^2}{E^{*2}\ D_0^3} \right]^{1/3} \tag{2.4}$$

where E* is the equivalent elastic modulus and $E^* = E'_1\, E'_2 / \left(E'_1 + E'_2 \right)$ and $E' = E / \left(1 - \nu^2 \right)$. γ_{12} is the interfacial surface energy, $\gamma_{12} = A_{12} / \left(24\pi D_0^2 \right)$. When $\mu_T > 5$, the JKR model applies, and when $\mu_T < 1$, the DMT model applies.

2.1.2 Friction Force Measurement

The coefficient of friction at the micro-scale is measured using an AFM, which was first by done Mate, et al. (1987) by modifying an AFM to measure both the normal and friction forces. Ruan and Bhushan (1994) and Bhushan and Ruan (1994) had presented

calibration procedures for converting measured data from a commercial AFM to normal and friction forces. They had also compared micro-scale friction data for selected materials with Si_3N_4 tips with macro-scale friction against Si_3N_4 balls. They found that the micro-scale friction was significantly smaller than macro-scale friction of the tested materials. At the micro- and nano-scales, it has been observed that the frictional force measured depends upon the contact area between the tested material and the applied normal load. The frictional force does not vary linearly with normal force in such situations, Karuppiah, et al. (2009). The micro-scale friction plays vital role in understanding the flow behavior of bulk materials, including grinding and wearing of materials, where particle contacts, plastic deformation, micro-friction are treated separately, Jones and Hodges (2004) and Cleary, et al. (2008).

At the micro-scale, flowing particles will collide. Collision force has a normal and/or tangential component. The tangential component of a collision force involves the friction forces resulting from the particles that slide against each other. The amount of frictional force (f) is proportional on the normal force (N) and the coefficient of friction (μ) between the particles.

$$f = \mu N \tag{2.5}$$

The normal force between particles depends on the momentum of the particles and the weight of the particles for dense flows. The coefficient of friction depends on the properties of the material contact surfaces. To quantify the friction force, the coefficient of friction of the interested material needs to be determined.

The test method introduced by Ruan and Bhushan (1994) using friction force microscopy is the most commonly used method for determining the coefficient of friction at the micro-scale. To measure the friction force using an AFM, the probe is lowered down gradually until the tip comes to contact with the sample and the cantilever deflects to apply a normal force (N_0) between the two contacting materials. The normal force is given by N_0 = cantilever vertical deflection H_0 × normal spring constant k.

The AFM is engaged in a scanning motion where the probe is moved parallel to the cantilever's long axis. The cantilever deflects due to the sample surface topography and also due to the friction force between the probe and the sample surface. The friction force acts in

the opposite direction of the probe motion (Figure 2.2a and Figure 2.2c). To maintain the deflection of the cantilever to a given value or set-point, the AFM piezo adjusts by retracting or extending, thus decreasing or increasing the normal load by ΔN_1 or ΔN_2, respectively (Figure 2.2b and Figure 2.2d). The change in normal load is given by ΔN_1 = piezo retraction $\Delta H_1 \times k$ or ΔN_2 = piezo extension $\Delta H_2 \times k$.

To calculate for the coefficient of friction (μ), it is first recognized that since the cantilever deflection in Figure 2.2b and Figure 2.2d are the same, then, the sum of the moments acting about the root of the cantilever at point P are the equal, i.e.

$$(N_0 - \Delta N_1)L + (f)(l) = (N_0 + \Delta N_2)L - (f)(l) \tag{2.6}$$

The friction force can be solved as

$$f = \frac{(\Delta N_1 + \Delta N_2)L}{2l} \tag{2.7}$$

The coefficient of friction can be solved with equation (2.5) as

$$\mu = \frac{f}{N} = \frac{(\Delta N_1 + \Delta N_2)}{N_0}\frac{L}{2l} \tag{2.8}$$

L and l are functions of the distance of the probe tip to the root of the cantilever L_c and the height of the tip h_t, making

$$\begin{aligned} L &= L_c \cos\theta \\ l &= L_c \sin\theta + h_t \cos\theta \end{aligned} \tag{2.9}$$

where θ is the angle between the cantilevers and the sliding surface.

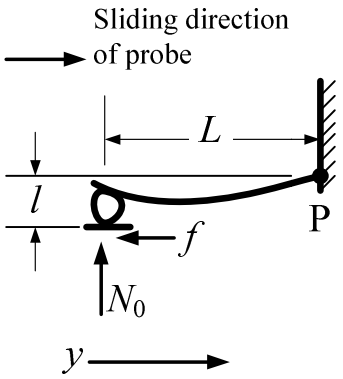

a) Additional deflection is caused by friction force as the probe slides in the positive y direction

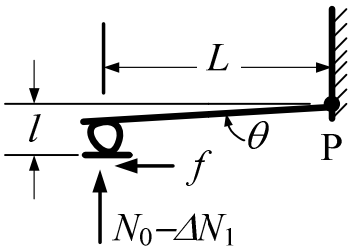

b) The effect is cancelled by retracting the piezo, thus reducing the normal force

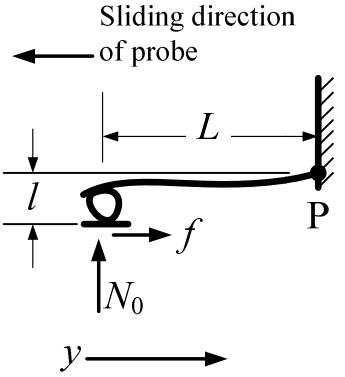

c) Additional deflection is caused by friction force as the probe slides in the negative y direction

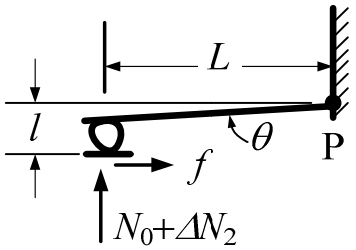

d) The effect is cancelled by extending the piezo, thus increasing the normal force

Figure 2.2. Schematic showing additional bending of cantilever due to friction force when the probe slides in the positive y and negative y directions and subsequent piezo adjustment to maintain an initial cantilever deflection

2.2 Rheology of Cement Based Materials

The rheological behavior of a cement-based material is commonly expressed by the relationship between shear stress and shear rate of the material under shearing. In its dry state, bulk cementitious materials are transported by rail, truck or ship. Pressurized air through pipe is commonly used for loading and unloading of the transporting vehicle. The design of hoppers (Descher, 1998), silos (Nielsen, 1998), and chutes (Jyotsna and Rao, 1997) in an effective and economical way requires a thorough understanding of the various factors governing the flow characteristics of granular materials must be obtained (Marcus, et al., 1990). When cementitious materials are used in concrete, it is mixed with water, aggregates and chemical admixtures. The rheological properties of the concrete affect concrete construction process, such as its transportation, placing and consolidation, which in turn influences hardened properties of the concrete such as uniformity, strength and durability, Banfill (2003).

2.2.1 Granular Flow of Dry Powders

Factors affecting the flow of dry materials are particle stiffness, mean particle size, shape and distribution, bulk and particle density (Littman, et al., 1995, Mills, 2004). Stresses increases with increase in particle stiffness at dense granular flows, Campbell (2006). Sufficient pressure should be maintained along a pipe for proper transport and to avoid blockages. Wall and material friction causes a drop in pressure drop along the pipe. This friction effect is being studied for dilute and dense flows (Pan, 1999, Jones and Williams, 2003 and Makkawi, et al., 2006). Other factors that affect friction such as particle degradation and inclination were also being studied (Wilson and Addie, 1997, Carpinlioglu, et al., 2002). The angle of repose can give an indication of the flowability of a material. When the angle of repose of a material is low, it is considered easily flowing while when it is high, it is considered cohesive and difficult to flow. The angle of repose is the angle between the horizontal and the natural slope of a heap of the material. For dry fine materials, a correlation exists between angle of repose and bulk coefficient of friction measured from a direct shear test (Chik and Vallejo, 2005, Ghazavi, et al., 2008).

Cementitious materials are often packed in bags or stored in barrels or silos. The behavior of bulk materials when under storage and transport, such as fluffing, consolidation

and ease/difficulty of filling and discharging to/from containers, are affected by its compression and shearing properties and its friction with contacting walls (Schulze, 2008). These behaviors also depend on particle characteristics such as particle size, size distribution, shape and roughness (Gu, et al., 1992). Although millions of tons of cementitious materials are used each year, little is known with regards to its bulk flow and storage properties. Many problems occur such as bridging, ratholing, flooding or uncontrolled flow and caking, which has a negative impact on production efficiency (Maynard, 2004).

2.2.2 Rheology of Pastes

Many constitutive models have been developed to represent the relationship, among which the Bingham model and Herschel-Bulkley models are the most commonly used for cement-based flow because of their simplicity and good representation for the majority of concrete mixtures (Ferraris, 1999). The Bingham model is a linear relation between shear stress τ, yield stress τ_0, plastic viscosity η and strain rate $\dot{\gamma}$. It is expressed as

$$\tau = \tau_0 + \eta\dot{\gamma} \tag{2.10}$$

The Herschel-Bulkley model is expressed as

$$\tau = \tau_0 + K\dot{\gamma}^n \tag{2.11}$$

where K is consistency and n is a constant that measures the amount of shear thinning or thickening. These models have been applied to study the flow behavior of cement pastes (Atzeni et al., 1985; Papo, 1988; Nehdi and Rahman, 2004) and SCC (de Larrard et al., 1988). Besides yield stress and viscosity, thixotropy, a property showing the time-dependent change in viscosity, is also observed and used for characterizing concrete rheological behavior.

Almost all components of a concrete mixture as well as the concrete manufacturing conditions affect rheology of the concrete. Most of these factors have been studied to some extent through experimental tests. Many of the studies have been focused on paste and mortar due to equipment limitations. Research has shown that the water content, the physical and chemical characteristics of cementitious materials, the type, surface texture, angularity,

particle size, and volume fraction of aggregate, and the type and dosage of admixtures all influence concrete rheological behavior (Hobbs, 1976; Rosquoet et al., 2003; Svermova et al., 2003; Vom Berg, 1979; Metha and Monteiro, 1993; Geiker et al., 2002; Badger et al., 2004; Chia and Zhang, 2004; Golaszewski and Szwbowski, 2004; Lachemi et al., 2004; Assaad et al., 2004).

Some models for predicting concrete rheological parameters have been developed with a consideration of concrete composition and mixture proportion (Hu et al., 1995; Roshavelov, 2005; De Larrard, 1999). Topcu and Kocataskin (1995) developed a model based on a two-phase approach and the law of plastic viscosity. Kennedy proposed the excess paste theory and explained its effect on concrete flowability (Kennedy, 1940). Oh et al. (1999) investigated and found that an increase in excess paste decreases both yield stress and viscosity of concrete. As mentioned previously, most existing studies on cement and concrete rheological behavior are experimentally dependent. The experimental results vary largely because of different materials investigated, equipment used, and test methods applied.

To measure the rheological properties of cementitious materials, it is typically loaded with an increasing and subsequent decreasing shear rate. A typical loading history is shown in Figure 2.3. The shear stress for the applied shear rate is recorded and a typical flow curve showing stress vs. shear rate for pastes is shown in Figure 2.4. The paste viscosity and yield stress were calculated from the down curve of the flow curve. The down curve follows a Bingham model. To calculate for the paste viscosity, a regression line is made. The slope of the regression line was the mixture viscosity. The zero intercept of the regression line was the calculated yield stress. The typical flow curve in Figure 2.4 shows the up curve higher than the down curve. This hysteresis loop was caused by the decrease in the viscosity due to colloidal structure breakdown with increasing time of shearing. Therefore, the thixotropy was calculated as the area between the up-curve and down-curve.

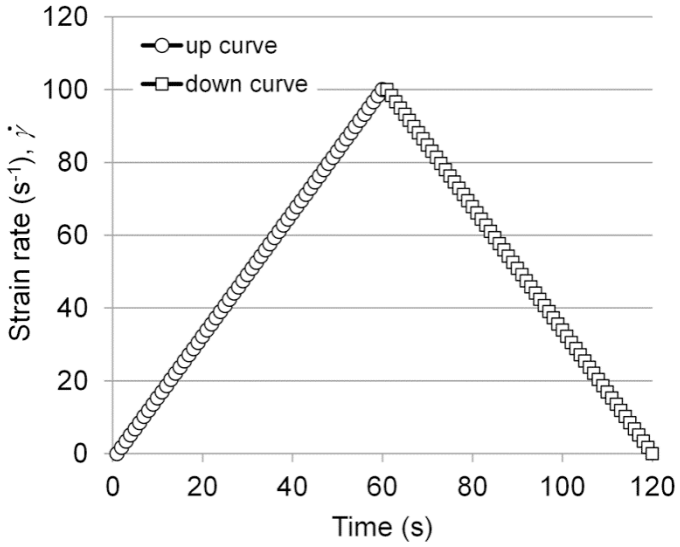

Figure 2.3. Loading history of paste rheology test

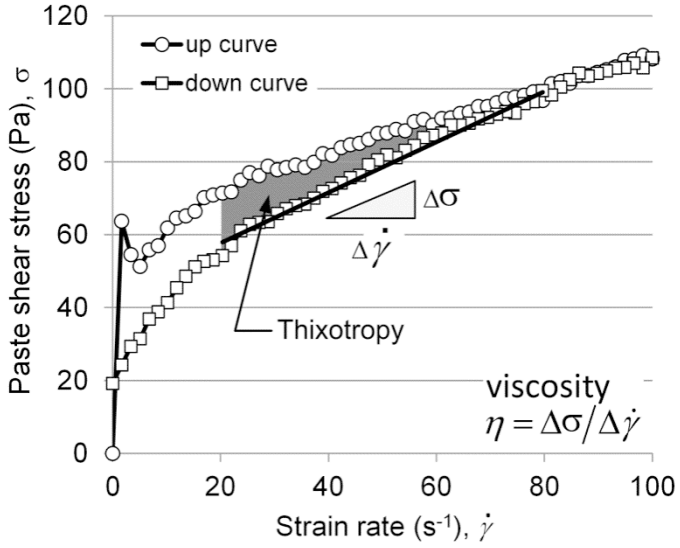

Figure 2.4. Flow curve of cementitious paste

2.3 Distinct Element Method (DEM) for Cement-Based Materials

The DEM was first introduced by Cundall and Strack (1979) for rock and granular flow simulation. After years of improvement (Campbell and Brennen, 1985; Walton and Braun, 1986), it was then used for flow analysis of fresh concrete by Nabeta (1994). Since then, the method has been the most successful method in simulating a wide variety of

concrete flow conditions including slump, L1-box, U-Box, V-funnel tests and shotcrete simulations, both in 2D and 3D models (Chu and Machida, 1996; Chu et al., 1996; Noor and Uomoto, 1999; Petersson, 2003; Petersson and Hakami, 2001; Puri and Uomoto, 2002). The advantages of DEM are that the scale of observation can be of the same size as the coarsest particle, the free surface of particles can be examined in detail, and a study of segregation is possible.

The basic concept in the DEM is the representation of concrete constituents into simple, spherical particles, Figure 2.5 and Figure 2.6. Other geometries may be used but could greatly increase the complexity of the solution. The particles may be representations of the coarse aggregate, fine aggregate, cement particles in concrete, mortar, or paste respectively. When the particles are in motion, they may collide and/or rub against each other. The contact constitutive model for these moving particles can be described as a combination of a spring, a slip and a dashpot as show in Figure 2.6. The DEM parameters are commonly determined indirectly by a sphere dragging viscometer (SDV) (Chu et al., 1996; Noor and Uomoto, 1999; Puri and Uomoto, 2002). To make it applicable to fresh concrete, an allowance of tension can be added to account for ductility or cohesion of mortar. Figure 2.7 shows the assumption made by Puri and Uomoto (2002), where coarse aggregate particles are coated with mortar. On collision of a pair of the aggregate particles, the mortar coating comes into contact first, then followed by the core aggregate particle. During separation, the mortar was assumed to be under tension, and breaks upon reaching a limiting distance.

The assumption of the separation behavior of aggregates and mortar has only been intuitively based. Though success has been made in modeling the macro behavior of concrete, the basic understanding of the micro behavior of its constituent materials still needs clarification (during approach, contact and separation).

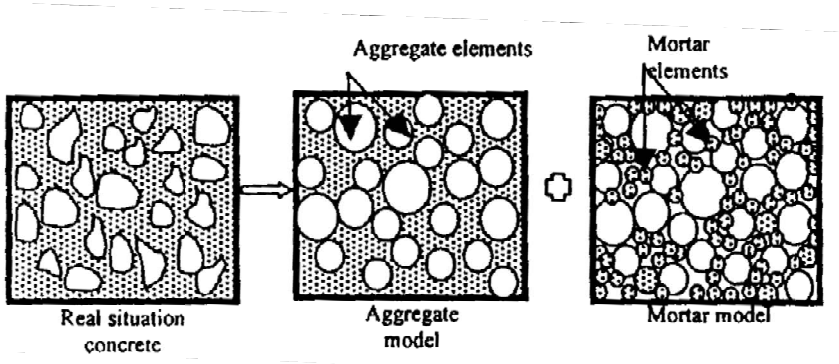

Figure 2.5. Two phase concrete model (Noor and Uomoto, 1999)

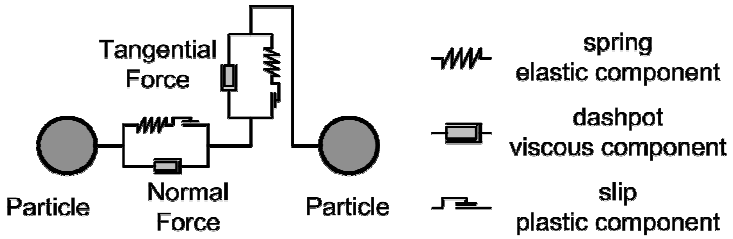

Figure 2.6. Standard contact law in DEM

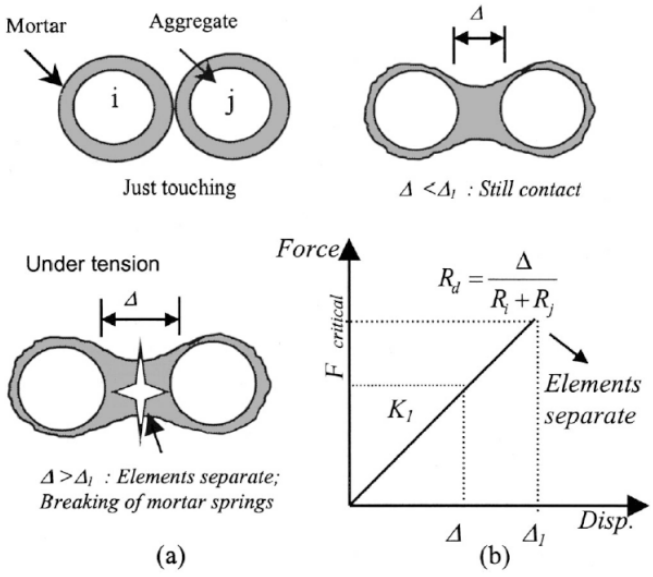

Figure 2.7. Consideration of mortar spring in tension using force-displacement law by Puri and Uomoto (2002)

The behavior of a DEM model depends on the contact mechanics, particle shape and size distribution. Common contact mechanics used are the linear spring–dashpot–slider system (Cundall and Strack, 1979) and more detailed models are based on the classical Hertz (1882) theory for the normal direction and the Mindlin and Deresiewicz (1953) model for the tangential direction. Other contact models are of an elastic-plastic type (Vu-Quoc and Zhang, 1999). In this case, particles undergo purely elastic collision when the contact force is less than a specified yield value. Above the yield value, particles undergo elastic–plastic deformation, and the loading–unloading force curve exhibits hysteretic behavior, finishing at a non-zero displacement as the repulsive contact force returns to zero.

Common applications of DEM deal with free flowing or non-cohesive problems (Nakamura et al., 2007, Coetzee et al., 2007, Tibor et al., 2005, Hoomans et al., 1996). Cohesion models can be applied by using liquid bridge force (Lian et al., 1993), square-well potential (Mehrotra et al., 2009), JKR model which extends the Hertzian contact law by introducing the work of adhesion per unit contact area (Johnson et al., 1971), and van der Waals forces (Moreno-Atanasio et al., 2007, Limtrakul et al., 2007, Zhang et al., 2005).

For modeling of concrete behavior, the linear spring–dashpot–slider system (Chu and Machida, 1996; Puri and Uomoto, 2002) is commonly adopted, with the separation model being assumed. Despite the common use of these models, the determination of suitable values for the contact parameters such as stiffness, damping coefficient, coefficient of restitution are not obvious (Malone and Xu, 2008) and an assessment of the suitability of these models for diverse DEM applications is still open (Di Renzo and Di Maio, 2004).

CHAPTER 3. ADHESION AND FRICTION OF CEMENTITIOUS MATERIALS AT THE MICRO-SCALE

3.1 Introduction

Several factors at the level of the particles affect the flow behavior of cement-based materials. These are particle adhesion, friction, size, shape, and spatial and size distribution. Adhesion force between particles tends to increase the stresses (Aarons and Sundaresan, 2006) and resistance to shearing (Rognon, et al., 2008) in a flowing system. The friction between particles acts in the opposite direction of the motion of the particles, thus increase the difficulty to flow. Hu (2005) studied the effects of fine aggregate size on viscosity and yield stress of cementitious mortars. His results showed that increasing the size of fine aggregates while maintaining the same volume fraction decreases viscosity and yield stress. This may be due to increase in particle spacing and reduction in number of particle in the system that the probability of collisions between particles is decreased. Hu also found that a well graded particle size distribution produces a lower viscosity and yield stress compared to uniform sized particles. The small size of silica fume particles (~100nm) is also often attributed to increase in viscosity and yield stress because of it high surface area compared to its volume that it requires more water to lubricate particle surfaces (Ferraris, et al., 2001). As with shapes, it has been widely accepted that a spherical shape, such as in fly ashes, improves flowability due to its ability to roll over one another (Ramachandran, 1995). Compared to other geometries, a sphere also has the least surface area for a given volume, thereby reducing water demand (Ploya and Szego, 1951). Other contributing factors are the rheological properties of the suspending fluid and its physical and chemical interactions with cementitious materials, such as the effects of chemical admixtures.

This chapter discusses two factors affecting rheological properties of cement-based materials at the micro-scale, adhesion and friction of cementitious materials. The study includes three parts. The first part is on the development of a methodology for measuring the adhesion forces and calculation of the Hamaker constant between cementitious materials and a commercially available AFM probe. The second part is the measurement of adhesion forces

between cementitious particles. The third part is the determination of the coefficient of friction between cementitious materials.

3.2 Materials

Six types of commercially available cementitious materials were used in the adhesion and friction studies at the micro-scale, ordinary Portland Cement (PC), Ground Granulated Blast Furnace Slag (GGBFS), Class C Fly Ash (CFA), and three Class F Fly Ashes (FFA1 to FFA3). Reference materials with known Hamaker constants were also used in the development and verification of the validity of the methodology for measuring adhesion forces. The reference materials used were mica, silica, and calcite. Silica and calcite are commonly found in concrete as aggregate, and their Hamaker constants have been previously studied, Bergstrom (1996). Different from silica and calcite that have granular particles, mica has a sheet structure and is commonly used in AFM-based adhesion and friction studies (Eastman and Zhu, 1996, Hu, et al., 1995 and Carpick and Salmeron, 1997) and can help verify the test methodology developed. The chemical properties of the cementitious materials are given in Table 3.1.

Scanning electron microscope (SEM) micrographs of the cementitious materials are shown in Figure 3.1. PC and GGBFS have angular particles due to the grinding during their production, while the fly ashes have rounded edges and spherical shaped particles, which are formed by fusing in suspension of exhaust gases.

Table 3.1. Chemical components (%) of cementitious materials

	Material					
	PC	CFA	GGBFS	FFA1	FFA2	FFA3
Na_2O	0.1	1.64	0.29	1.08	2.63	1.53
MgO	3.07	4.87	9.63	1.73	2.44	1.27
Al_2O_3	4.24	17.68	8.54	27.52	23.63	19.63
SiO_2	21.16	31.92	36.5	54.87	49.30	43.52
SO_3	2.63	1.68	0.6	0.36	1.91	6.24
K_2O	0.66	0.43	0.44	4.36	1.22	2.31
CaO	64.39	30.9	41.1	1.70	11.56	11.41
Fe_2O_3	3.07	6.54	0.83	6.92	5.83	12.80
Others	0.68	4.34	2.07	1.46	1.48	1.29

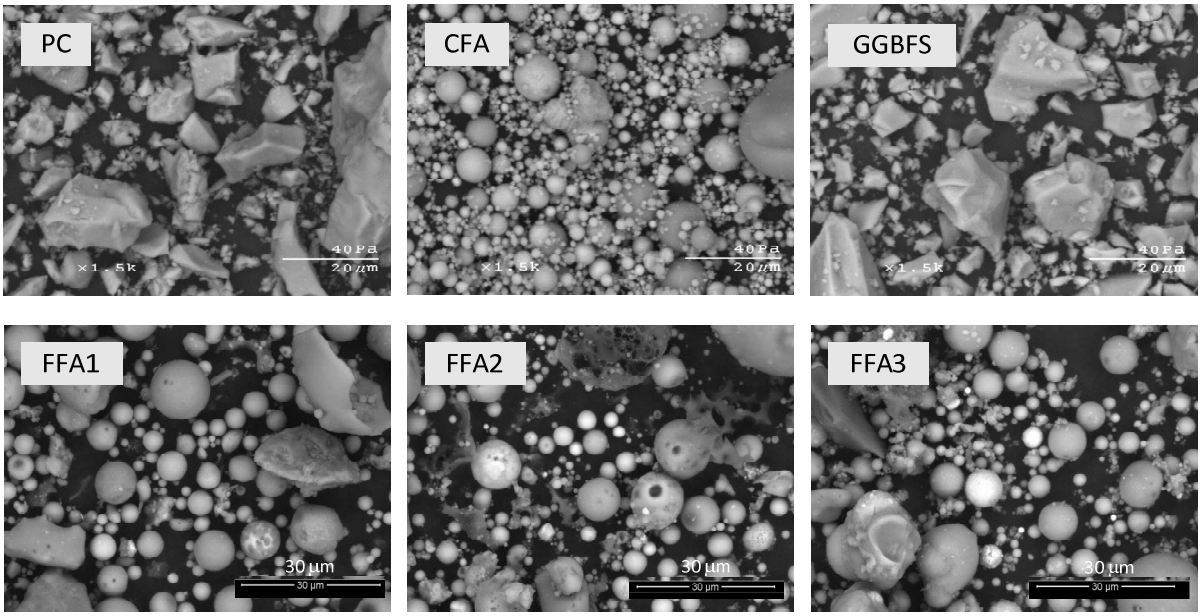

Figure 3.1. SEM micrograph of cementitious powders

3.3 Measuring Hamaker Constant of Cementitious Materials

The following section presents the measurement of adhesion and determination of Hamaker constant of commercially available cementitious materials using AFM. The method

contains two steps: (1) measuring the adhesion force between the tested material and a selected probe using AFM and (2) calculating the Hamaker constant of the tested material from the measured adhesion force using established contact mechanics models. The materials used were PC, GGBFS and the reference materials silica, calcite and mica. The adhesion force measurements are performed in both dry air and water.

3.3.1 Adhesion Force Measurement

Sample Preparation

All materials investigated, except for mica, were in a powder form. Since mica has a thin sheet structure, it only needed to be freshly cleaved before testing. The tested material was first mixed with a two-part fast setting epoxy at a powder-to-epoxy ratio of 1:3 by weight. After mixing, the sample was placed on a glass slide and cured at 80º C for 8 hours. After cooling down, the sample was sanded flat and the surface of the sample was polished with a set of sandpapers from coarse to fine grits of 150, 400, 800, 1000 and 2000. During polishing, the sample was blown with pressurized line air to prevent dust accumulation. After polishing, the samples were cleaned with compressed nitrogen gas.

Figure 3.2 illustrates representative 5 μm × 5 μm images of the polished samples obtained using atomic force microscopy in the standard contact mode. The roughness of the polished samples could influence the results of the adhesion force measurements. A high roughness of a sample can change the contact area and thus affect the adhesion measurements. Therefore, the root mean square (RMS) surface roughnesses of the resulting surfaces were evaluated. The RMS roughnesses of five polished materials were determined and their average RMS_{ave} are given in Figure 3.2. The results indicate that the examined sample surfaces had an RMS roughness ranging from 9.5 to 37.5 nm for a 5 μm × 5 μm scan. Among surfaces scanned, the calcite sample had the highest RMS, while the PC had the lowest RMS values.

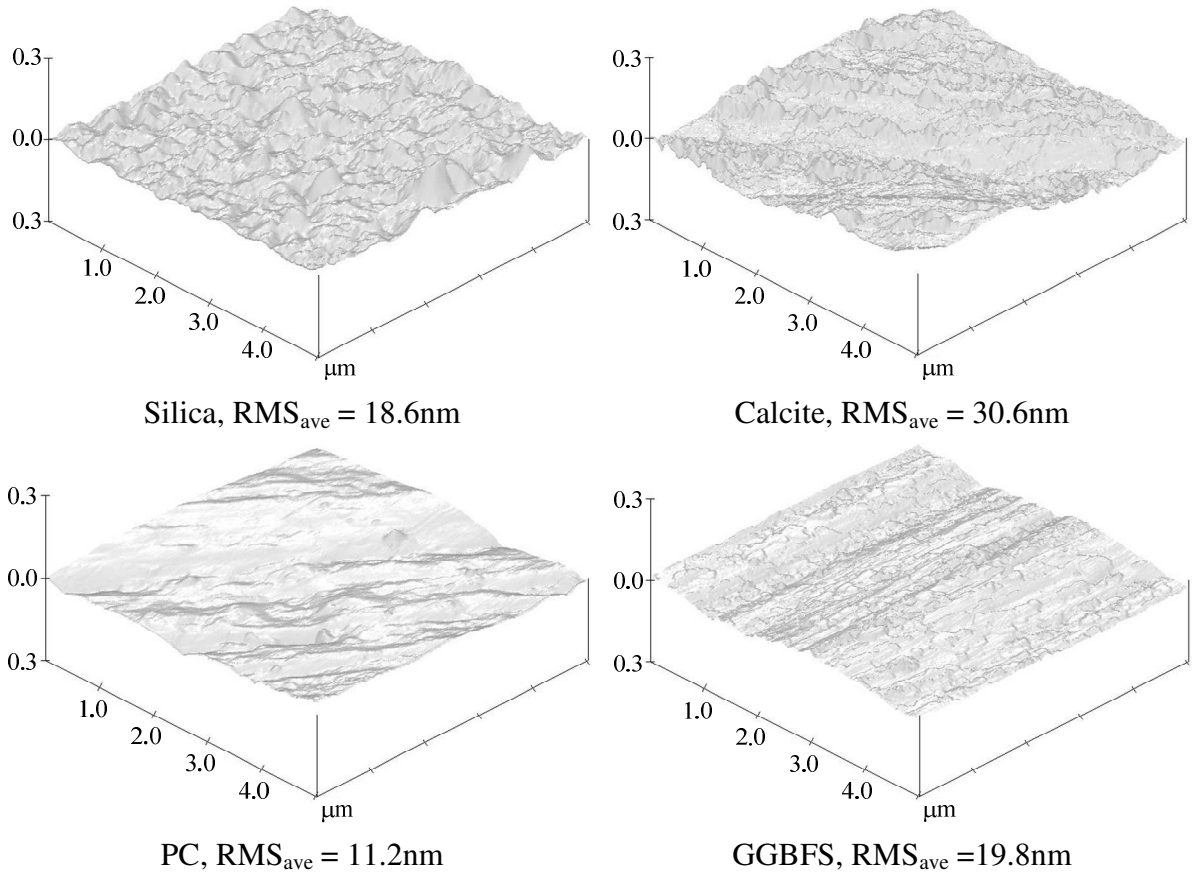

Figure 3.2. Scanned images from the surface of the sandpaper polished samples with average roughness values

AFM Test Setup

The AFM used was the model Dimension 3100, Nanoscope IV of Veeco Instruments, CA, and the test set up is shown in Figure 3.3. Standard commercially available silicon nitride (Si_3N_4) probes were used.

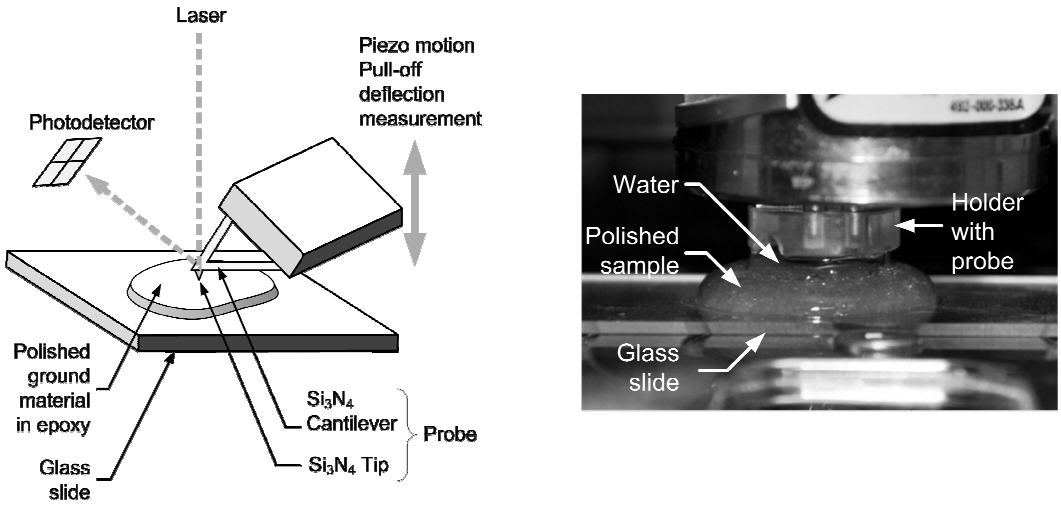

Figure 3.3. Schematic of pull-off deflection measurement and set up for test in water

The AFM measurements were conducted in both dry air and water. Dry N_2 gas was used for the air environment, and Milli-Q ultrapure water was used as the water environment. When a test was performed in water, both the polished powder material and probe were completely submerged in the water.

To assess the pull-off force, the normal stiffness of the probes must be known. The normal stiffness of each probe used in the present study was determined according to the method outlined by Torii et al. (1996). Two reference probes with a known normal stiffness of 0.164 and 1.28 N/m were employed. The probes used in the present study had normal stiffness ranging from 0.16 to 0.74 N/m with a deviation of 1.2% from the average.

The amount of pull-off force measured with AFM is also dependent on the geometry of the probe tip, which directly impacts the contact area. AFM probe tips have a parabolic shape and the vertex is defined by a spherical radius (Wilson, et al., 1996 and Carpick, et al., 1996). The probe tip was imaged to determine its radius with a diffraction grating TGT1

from NT-MDT, Switzerland, as shown in Figure 3.4a. From the image, perpendicular sections were obtained. The image cross-section was fitted with a curve to get a radius of curvature, Figure 3.4b-c. The radius of the probe tip was the average of the radius from perpendicular sections. For each probe used, scans were taken from three grating tips. The variation in radius measurement for a single probe was within 13.5% of the average.

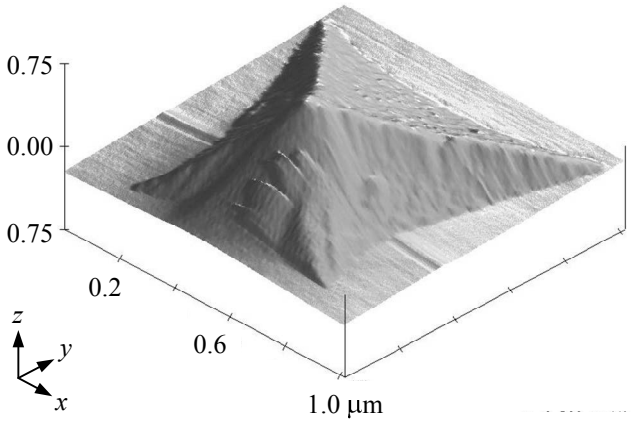

a) AFM image of Si_3N_4 tip obtained using a tip characterization grating

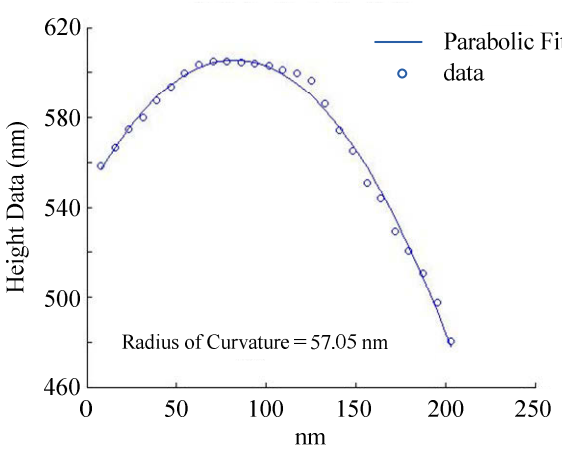

b) Cross section of tip along x direction

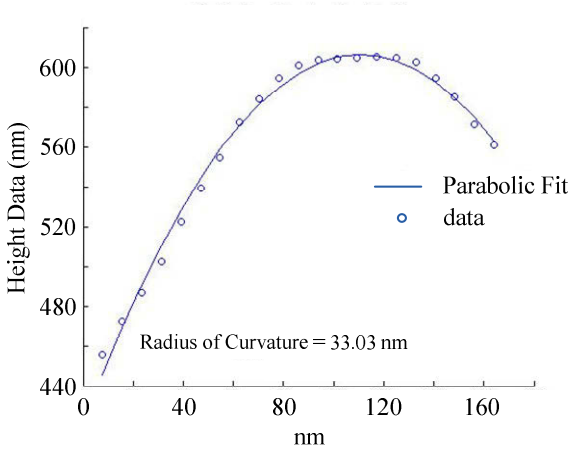

c) Cross section of tip along y direction

Figure 3.4. Image of Si_3N_4 tip using AFM and parabolic curve fit of tip scan data points along the x and y directions

Force Measurements

Force measurements are performed by acquiring force-distance curves using the AFM, Butt, et al. (2005). A schematic of a typical force-distance curve is shown in Figure

3.5. In a typical measurement, the tip (at the end of the probe) is initially held far from the sample (a). It is then brought into contact with the stationary sample using a piezo-motor. As the probe approaches the sample, the attractive force gradient of the probe-sample interaction exceeds the normal spring constant at a location close to contact. This causes an instability whereby the probe tip snaps into contact with the sample and probe is seen to deflect past the "zero force" level (b). As the probe continues to advance, it presses on the sample and further deflects to its maximum value (c). Subsequently, the probe is retracted or "withdrawn" away from the sample. During this process, the probe keeps in contact with the sample (d) until the spring constant overcomes the attractive force gradient that results in the cantilever "snapping back" to its undeflected position (e). The deflection of the probe (and hence the force obtained by multiplying deflection with probe normal stiffness) is continuously recorded as a function of piezo displacement. The velocity of the probe for the whole process is 1.0×10^{-6} m/s.

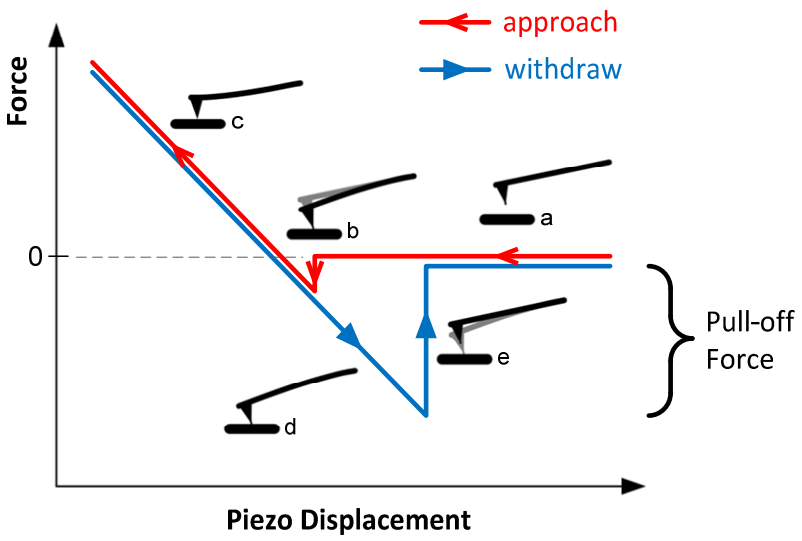

Figure 3.5. Sketch of a typical force curve

The pull-off force (F) between the two particles tested was calculated from the cantilever pull-off deflection (δ) and normal stiffness (k) as:

$$F = k\delta \tag{3.1}$$

The pull-off deflection (δ), as indicated in Figure 3.5 is the distance from the initial/neutral position of the probe to the of the probe tip-sample separation.

To start the test measurements in dry air, the AFM chamber was closed and purged with N_2 gas to reach experimental conditions of RH (relative humidity) $\leq$ 8 % to eliminate the effects of humidity on the measured forces. To test the samples in water, a droplet of water was placed on the polished sample surface. The droplet was then approached by the probe until it was fully submerged. When both the probe and polished particle were completely submerged in water, the probe approached the particle until it contacted and it was then pulled off from the particle in the same manner as the test in air.

For each material (reference or cementitious materials) tested under each environment (in air or water), five particles on a polished sample were selected. On each particle, 5 locations (1μm apart) were chosen. For each location, 3 measurements were recorded. Thus, a total of 75 measurements were taken for each material tested under each environmental condition.

Results from Force Measurements

All inter-particle forces measured are at the nano-Newton (nN) level. Figure 3.6 shows typical force curves for measurements conducted in air. The negative force corresponds to attraction and a positive force corresponds to repulsion. The slope of the repulsive region and the pull-off force varies because it depends on the properties of the contacting materials and geometry of the probe tips. Based on contact mechanics models, it is expected that as the adhesion force and the radius of the probe tip increases, the pull-off force increases.

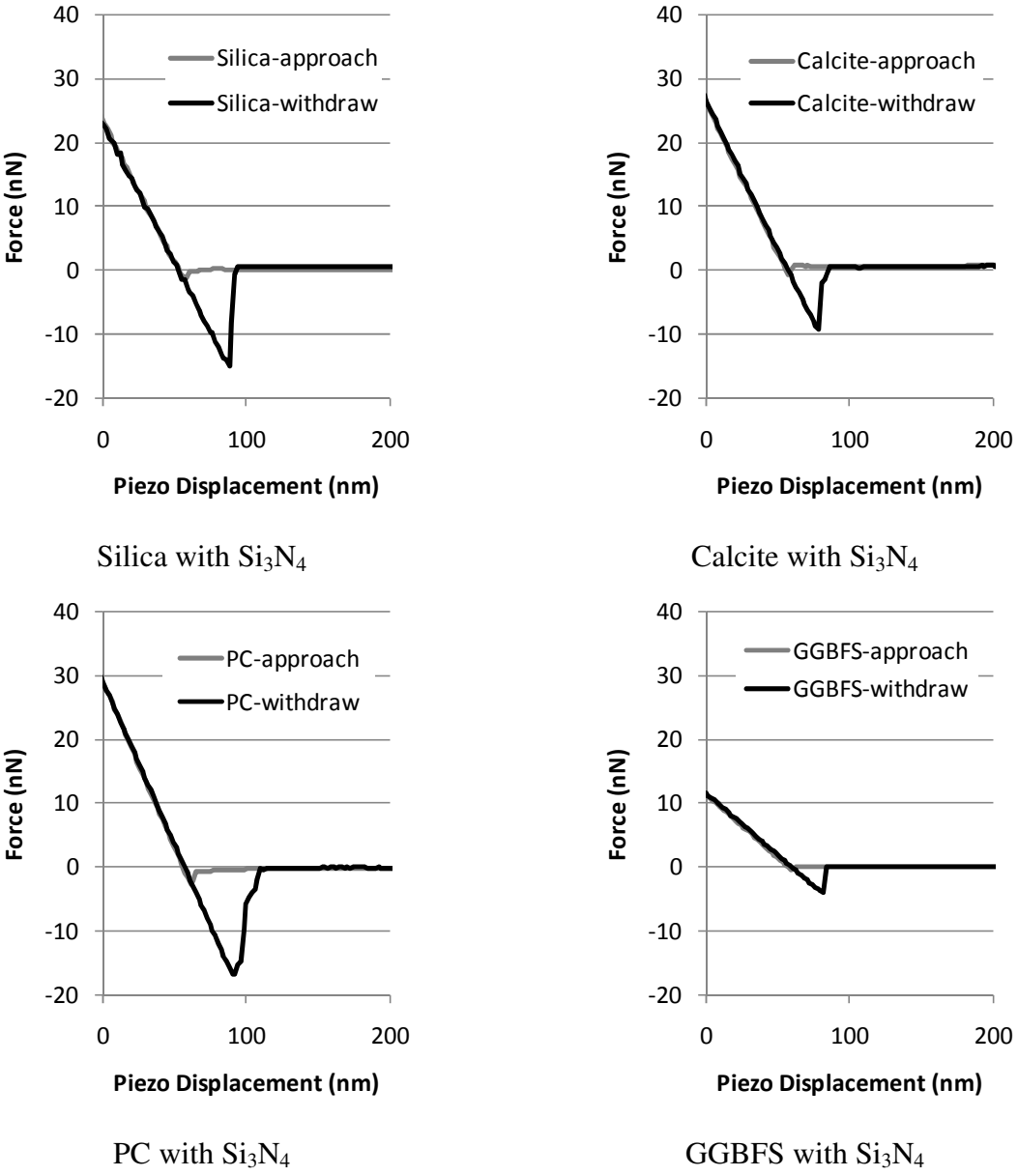

Figure 3.6. Typical force curves measured from tested materials and probe (Si_3N_4) in air

Typical force curves for measurements conducted in water are shown in Figure 3.7. The jump-to-contact between the probe and a particle was not seen in the approach part of the curve that resulted from measurement in water. This is attributed to the double layer effects of the tested materials that typically exist in water.

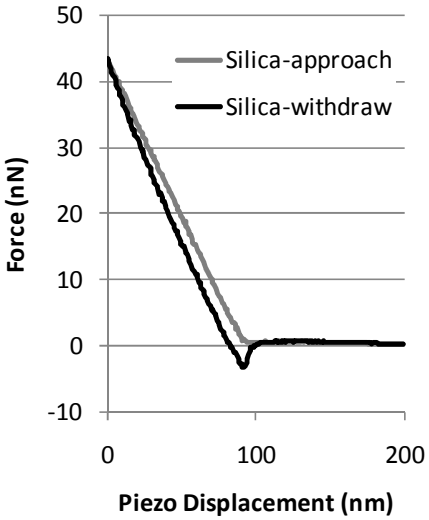

Silica with Si_3N_4

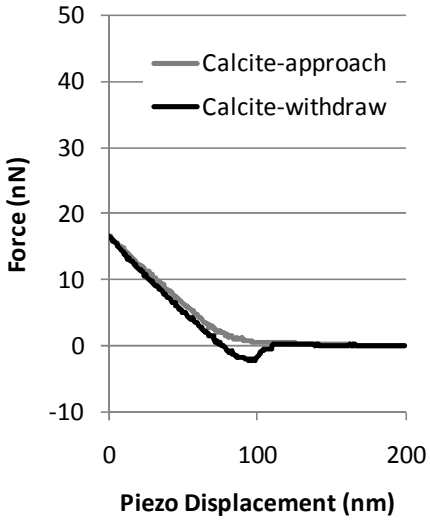

Calcite with Si_3N_4

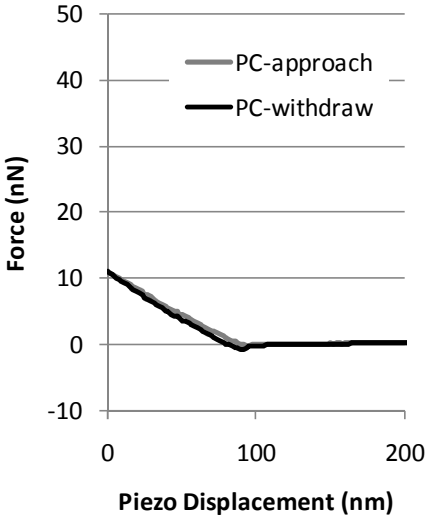

PC with Si_3N_4

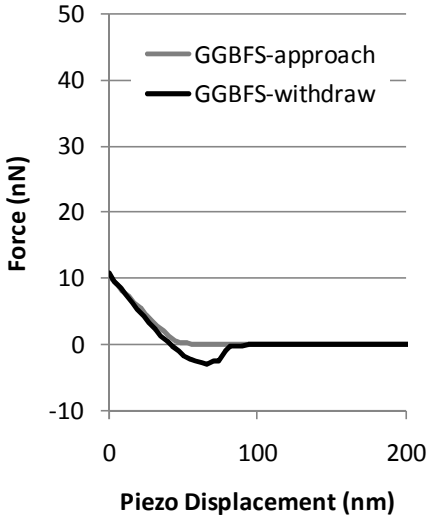

GGBFS with Si_3N_4

Figure 3.7. Typical force curves measured from tested materials and probe (Si_3N_4) in water

As shown in Figure 3.8, the double layer refers to two parallel layers of charge on the surface of the submerged particle. The first layer is a compact layer that is made of absorbed ions due to chemical interaction. The second layer is a diffuse layer composed of ions attracted to the surface charge, Lyklema (2005). Because of the double layer, a repulsive

force is exerted on the probe tip, which tends to reduce the jump-to-contact tendency of the probe when compared with the interaction in air.

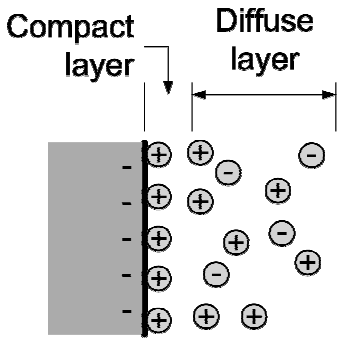

Figure 3.8. Schematic of double layer formation on the surface of a submerged material

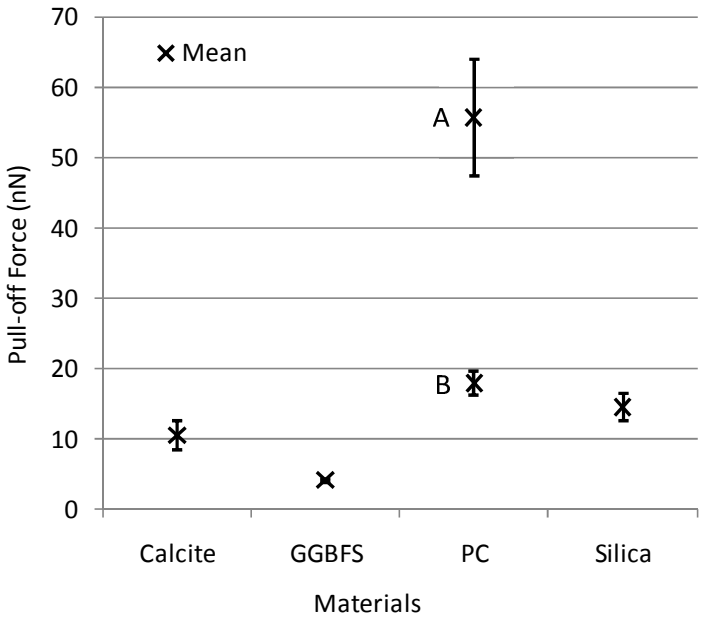

Figure 3.9. Distribution of pull-off forces for different materials tested

The distribution of the calculated pull-off forces in air is shown in Figure 3.9. The lines above and below the mean identify one standard deviation of the data. It is noted PC exhibits two distinct values of pull-off forces (indicated as group A and group B). The force of Group A was about 56.4 nN and Group B was around 17.9 nN. As explained later, this is most likely due to the different phases in the particles of Portland cement, and the two

groups' forces were also observed in the tests in water. Table 3.2 gives the mean pull-off force calculated in both air and water.

Table 3.2. Pull-off forces of materials interacting Si_3N_4 with in air and water (nN)

Material	In Air	In Water
Mica	50.70±0.68	
Silica	14.66±0.57	2.47±0.27
Calcite	10.19±0.55	1.90±0.46
PC (Group A)	56.42±2.94	6.39±2.28
(Group B)	17.91±0.67	1.11±0.11
GGBFS	4.06±0.09	2.77±0.58

3.3.2 Hamaker Constant Determination

Work of Adhesion

The pull-off force (F) evaluated from the experiment and equation (3.1) may be expressed in terms of work of adhesion (W) of the interface and AFM probe tip radius (R). Work of adhesion is the decrease in free energy per unit area when an interface is formed from two individual surfaces 1 and 2. The tested material will be referred to with subscript 1 and the silicon nitride probe with subscript 2. Depending on the stiffness of the material, the models by Johnson, Kendall and Roberts, (1971, JKR) or by Derjaguin, Muller and Toporov (1975, DMT) for a spherical particle in contact with a plane surface applies. The JKR and DMT models are expressed as

$$F = c\pi R W_{12} \tag{3.2}$$

The constant c is 3/2 for the JKR model and is 2 for the DMT model. The work of adhesion can be expressed as a function of Hamaker constant (A_{12}) between two contacting bodies and cut-off distance (D_0). The cut-off distance is the interfacial separation between two contacting materials, Israelachvili (1991).

$$W_{12} = \frac{A_{12}}{12\pi D_0^2} \tag{3.3}$$

The application of the two models is usually chosen based on the Tabor parameter (μ_T), Tabor (1977). The parameter is a function of the probe tip radius (R), adhesion energy (γ_{12}), cut-off distance (D_0), elastic modulus of the contacting materials (E) and Poisson's ratio (ν).

$$\mu_T = \left[\frac{R\ \gamma_{12}^2}{E^{*2}\ D_0^3} \right]^{1/3} \tag{3.4}$$

where E^* is the equivalent elastic modulus and $E^* = E'_1\ E'_2 / \left(E'_1 + E'_2 \right)$ and $E' = E / \left(1 - \nu^2 \right)$. γ_{12} is the interfacial surface energy, $\gamma_{12} = A_{12} / \left(24\pi D_0^2 \right)$. When $\mu_T > 5$, the JKR model applies, and when $\mu_T < 1$, the DMT model applies. In the present study, the average probe tip radius was 35 nm and the cut-off distance was assumed as 0.165 nm. The Tabor parameters of mica, silica, and calcite interacting with a silicon nitride probe were calculated and are listed in Table 3.3. Since the calculated μ_T values were all much less than 1, use of the DMT model is appropriate.

Table 3.3. Reference material properties

Material	E (GPa)	ν	A_{12} ($\times 10^{-20}$ J)		μ_T	
			air	water	air	water
Mica	70.7	0.25	12.80	2.45	0.20	0.07
SiO_2	72.4	0.17	10.38	1.90	0.18	0.06
$CaCO_3$	75.0	0.30[a]	12.90	2.53	0.20	0.07
Si_3N_4	280.0	0.20				

[a]assumed value

For the cementitious materials studied, their elastic modulus, Poisson's ratio and Hamaker constants in interaction with silicon nitride are unknown. Thus, their μ_T values

cannot be determined. Therefore, the Hamaker constants resulting from both JKR and DMT models are presented in this paper.

Random Errors from Experimental Measurements

The Hamaker constants (A_{12}) of the materials tested with their interaction with silicon nitride can be estimated by combining Equations (3.1), (3.2), and (3.3). The resulting relationship is

$$A_{12} = \frac{12 D_0^2 \delta k}{cR}, \quad c = \begin{cases} 3/2 & \text{for JKR model} \\ 2 & \text{for DMT model} \end{cases} \tag{3.5}$$

Equation (3.5) expresses that the Hamaker constant (A_{12}) is a function of three parameters (δ, k, and R) that are obtained from experimental measurements. We therefore report the Hamaker constant as

$$A_{12} = \bar{A}_{12} \pm u_A \tag{3.6}$$

where, $\bar{A}_{12}$ is the calculated Hamaker constant based on the mean value as expressed in Equation (3.7)

$$\bar{A}_{12} = \frac{12 \bar{D}_0^2 \bar{\delta} \bar{k}}{c \bar{R}} \tag{3.7}$$

and u_A is the 95% uncertainty due to combined random errors in the individual measurements.

$$u_A = \left[\left(\frac{\partial \bar{A}}{\partial D_0} u_{D_0} \right)^2 + \left(\frac{\partial \bar{A}}{\partial \delta} u_\delta \right)^2 + \left(\frac{\partial \bar{A}}{\partial k} u_k \right)^2 + \left(\frac{\partial \bar{A}}{\partial R} u_R \right)^2 \right]^{1/2} \tag{3.8}$$

u_{D_0}, u_δ, u_k and u_R are the individual uncertainties resulting from measurements of D_0, δ, k and R, respectively. The instrument error was calculated to be 61.0 picometer, SBO

(2010), which is relatively small compared to random errors and are not included in the analysis.

Different values of D_0 have been reported for various materials. Plassard, et al. (2005) used 0.2 nm for the interaction of silica with mica, calcite or gypsum. Bhattacharya, et al. (2008) suggested that D_0 for polymers might vary from 0.165 to 0.185. Matsuoka, et al. (2010) reported that D_0 could be as low as 0.132 nm. Israelachvilli (1991) recommended the mean value of $\bar{D}_0$ used in the calculation of interfacial surface energy as 0.165 nm. Using this value, he obtained results with an accuracy of 10-20% for most materials. We therefore assume the uncertainty of D_0 as $\pm 0.10\,\bar{D}_0$.

As shown in Table 3.4 and Table 3.5, the uncertainty for the measurements of the pull-off deflection (δ), probe stiffness (k) and probe tip radius (R) were based on the 95% confidence interval of the measurement. The random error in the pull-off deflection was from 75 sample measurements in each material. The variation in the measurement of the cantilever stiffness was based on the data from measurements with two reference cantilevers.

Table 3.4. Mean and uncertainty values of measurements in air

	Mica	Silica	Calcite	PC (A)	PC (B)	GGBFS
δ (nm)	104.54±1.40	30.23±1.17	21.02±1.14	116.33±6.06	36.93±1.38	20.29±0.46
k (N/m)	0.485±0.006	0.485±0.006	0.485±0.006	0.485±0.006	0.485±0.006	0.200±0.002
R (nm)	76.98±10.39	19.70±2.66	19.70±2.66	38.30±5.17	38.30±5.17	12.84±1.73

Table 3.5. Mean and uncertainty values measurements in water

	Silica	Calcite	PC (A)	PC (B)	GGBFS
δ (nm)	3.57±0.395	8.02±1.96	28.9±10.29	5.02±0.50	13.6±2.86
k (N/m)	0.693±0.008	0.237±0.003	0.221±0.003	0.221±0.003	0.204±0.003
R (nm)	20.60±3.86	30.22±2.90	36.12±5.17	36.12±5.17	57.88±8.29

Another aspect of water exposure and phase formation is the potential for changes in surface roughness. Drastic changes in roughness can significantly alter the contact area and

contribute to large errors in the obtained constants. To determine the change in the surface roughness of the tested PC samples due to exposure to water, the RMS roughness of a polished PC was measured before and after 45 minutes of wetting. The results showed that the change is less than ±10 percent. This amount of change in the surface roughness would have negligible impact on the contact area and test results. An example of a PC surface before and after wetting is shown in Figure 3.10.

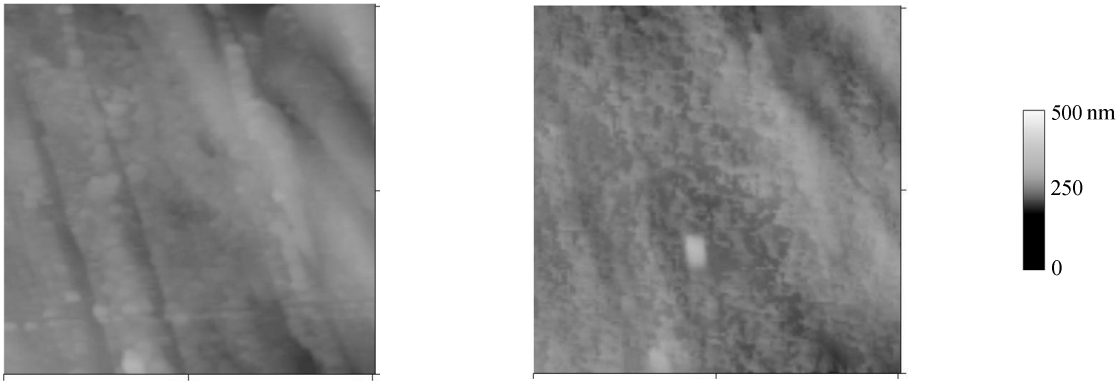

Figure 3.10. 5×5 μm AFM surface scan of polished Portland cement particles before and after wetting for 45 minutes

Hamaker Constants in Air

With consideration of the random errors in the experimental measurement, the Hamaker constants of the reference and cementitious materials with its interaction with silicon nitride (the probe) in air are given in Table 3.6.

Table 3.6. Hamaker constants A_{12} of tested materials interacting with Si_3N_4 in air ($\times 10^{-20}$ J)

Tested Material	DMT	JKR	Reference
Mica	10.76±2.60		12.80
Silica	12.16±2.97		10.38
Calcite	8.45±2.09		12.90
PC (Group A)	24.06±5.95	32.08±7.93	
(Group B)	7.64±1.87	10.19±2.49	
GGBFS	5.15±1.25	6.88±1.67	

The table shows that the values determined by the present method for reference materials studied are consistent with those published by previous researchers. Since the Tabor parameter μ_T <1, only the DMT model was used. The DMT model is well suited for mica and silica, but it resulted in a lower Hamaker constant for calcite when compared with the value published by previous researchers. We attribute the difference to the relatively high RMS of the sample, which was 30.6nm, while the RMS of mica, silica and cementitious materials studied were below 20nm. The contact models assume contact between smooth surfaces. Our results suggest they provide meaningful results even for surfaces with RMS values < 20 nm (5 μm scan).

Because of the two groups of pull-off forces, Table 3.6 shows the corresponding two values of Hamaker constants of PC. The Hamaker constant of GGBFS is lower than that of PC. The difference in the Hamaker constant values obtained from the two models (DMT and JKR) is not significant for the cementitious materials.

Hamaker Constants in Water

Due to the effect of the double layer formed in the materials tested in water, a repulsive force is exerted on the probe tip. Thus, the Hamaker constant cannot be directly computed. Rather, we refer to the computed value from Equation (3.6) as an "effective" Hamaker constant. Figure 3.11 and Figure 3.12 shows the force interaction curves (Cappella and Dietler, 1999) for tested reference and cementitious materials with Si_3N_4 probe in water with respect to the tip separation from the sample surface, respectively. It can be observed in

the figure that most of the materials tested exhibited a repulsive long range force. Consistent with the results in air, PC showed two different groups of interaction curves labeled as PC(A) and PC(B). PC(A) does not have a repulsive regime which indicates a long range adhesive property.

The electric double layer on the surface of a material in water can be influenced by the ionic strength of the liquid (Pendersen and Bergström, 1999 and Ferrari, et al., 2010). For the case of calcite, its dissolution will change the ionic charge in the liquid and affect the double layer characteristics. The effects of ionic charge of the liquid on the double layer and interparticle force of commercially available cementitious materials is of interest and is part of a study currently being conducted.

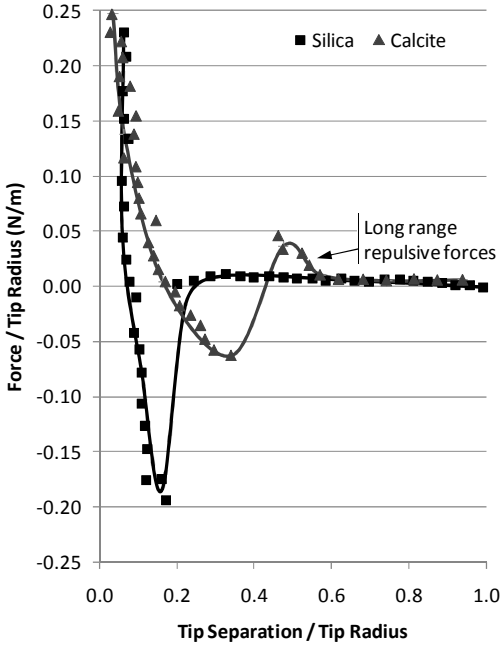

Figure 3.11. Force interaction curves for tested reference materials with Si_3N_4 in water

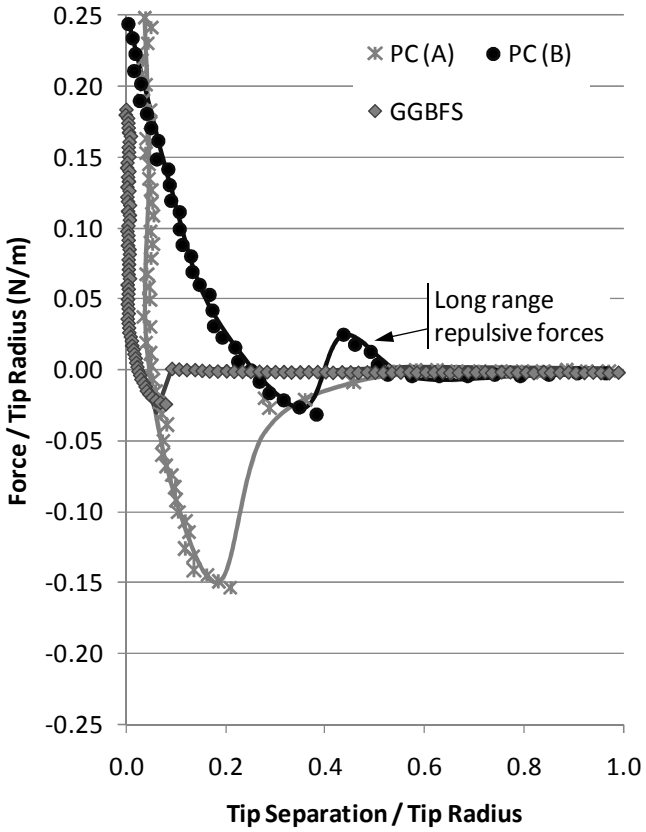

Figure 3.12. Force interaction curves for tested cementitious materials with Si_3N_4 in water

Table 3.7. Effective Hamaker constants of tested materials interacting with Si_3N_4 in water ($\times 10^{-20}$ J)

	DMT	JKR	Reference
From Direct Measurement (A_{132})*			
Silica	1.96±0.58		1.90
Calcite	1.03±0.34		2.53
PC (Group A)	2.89±1.25	3.85±1.67	
(Group B)	0.50±0.13	0.67±0.18	
GGBFS	0.78±0.25	1.04±0.71	
Derived with Equation (3.9) (A_{131})*			
PC (Group A)	1.72±1.49		1.60
(Group B)	0.05±0.03		
GGBFS	0.12±0.09		

*subscripts 1, 2, 3 indicates the sample material, Si_3N_4 and water, respectively

The computed effective Hamaker constants in water are given in Table 3.7. It can be noted that the effective Hamaker constant of silica in water is still close to that reported in the previous study, while the effective Hamaker constant of calcite is much lower than that reported in the previous study. This is probably related to the relatively high dissolution of calcite in water, which enhances the double layer effect. Although much lower than those measured in air, the Hamaker constant values of PC measured in water can again be divided into two groups. The Hamaker constant values of GGBFS measured in water is also relatively lower than the reference materials. The values obtained for the two contact models (DMT and JKR) for both PC and GGBFS are not significantly different.

Energy Dispersive X-ray Spectroscopy (EDS) was employed to determine the properties of the tested sample. Figure 3.13 shows the element map of polished PC with an epoxy matrix. The sample was wetted for 45 minutes, which was the duration of testing. The map shows the presence of different phases in the cement by the distribution of calcium, silicon, aluminum and iron in the particles. Analysis of sample at different points in particles indicated the presence of unhydrated C3S and C2S.

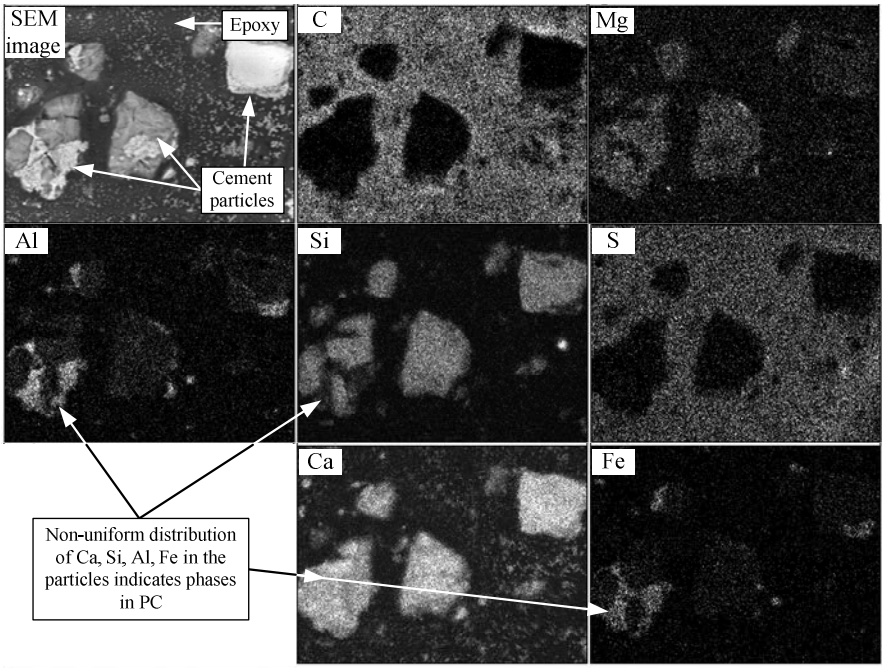

Figure 3.13. Element map of polished Portland cement particles in epoxy that was wetted for 45 minutes (bright/dark regions indicates presence/absence of the element)

In the work conducted by Flatt (2004), a method of determining the approximate Hamaker constants of the different phases of partially hydrated cement in water was introduced. Based on this work, the Hamaker constants were approximately 1.6×10^{-20}J for C3S, 0.055×10^{-20}J for ettringite, and 0.20×10^{-20}J and 0.70×10^{-20}J for C-H-S with and without nonstructural water, respectively. It is noted that the unhydrated cement compound C3S had a much higher Hamaker constant than cement hydration products, such as ettringite.

To compare results from the present study with that from Flatt for PC in water, the Hamaker constant of PC phases can be estimated as follows:

$$A_{PC/Si3N4} = \sqrt{A_{Si3N4} A_{PC}} \tag{3.9}$$

Hamaker constant of silicon nitride in water (A_{Si3N4}) is equal to 4.85×10^{-20}J, Bergstrom, 1996. Taking two values of PC from Table 3.7 (DMT) as $A_{PC/Si3N4}$, the Hamaker constants of PC (A_{PC}) obtained from equation (3.9) are $1.72\pm1.49\times10^{-20}$J for Group A and

$0.05\pm0.03\times10^{-20}$J and for Group B. The Hamaker constant derived from Group A is similar to the Hamaker constant estimated by Flatt for C3S, which is present in the wetted sample based on the EDS analysis. This comparison further suggests that the present test method for determining the Hamaker constant is valid and can be used to differentiate phases in cementitious materials, provided that the different Hamaker constant values of the phases are larger than the uncertainty values. Further examination may be needed for the Hamaker constant from Group B when considering the values from Flatt (2004) and the EDS analysis. The Hamaker constant for GGBFS (A_{GGBFS}) can also be computed using the same method, and is equal to $0.12\pm0.09\times10^{-20}$J.

3.4 Particle-Particle Adhesion

This section presents the measurement of adhesion forces between cementitious particles by applying the developed method in the previous section to particles affixed on a slide and a particle attached to the tip of an AFM probe. The materials used are the six cementitious materials mentioned in Section 3.2. The tests were done in dry air, water and sodium hydroxide solution with varying pH.

3.4.1 AFM probes and sample preparation

AFM probes were prepared by attaching PC and fly ash particles to the ends of AFM cantilevers. Figure 3.14 shows AFM probes attached with a PC particle and fly ash particles on their tips. The normal stiffness of the cantilever used ranged from 0.17 to 0.39 N/m, which was determined using the reference cantilever method proposed by Torii, et al. (1996).

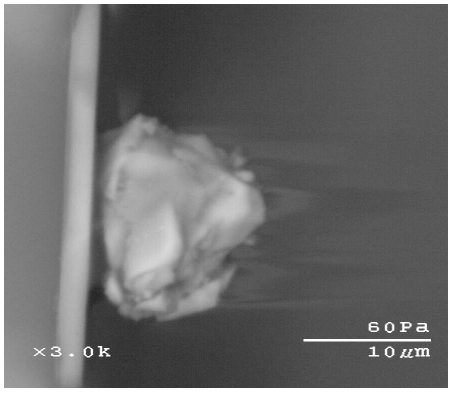

a) PC tip viewed from end of cantilever

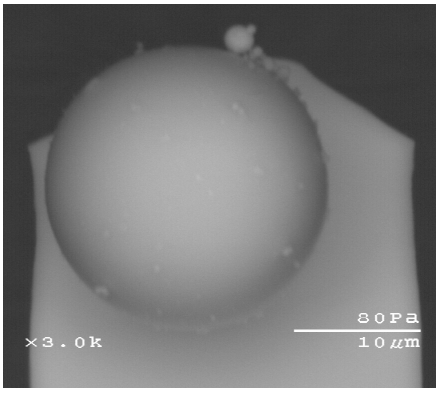

b) CFA tip viewed from top of cantilever

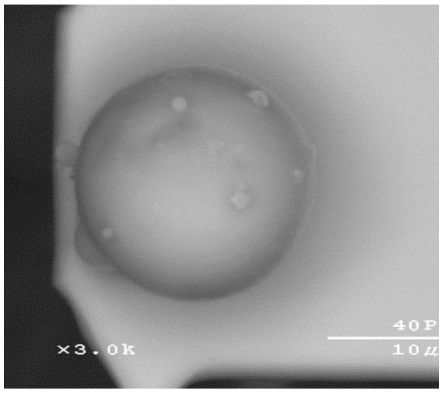

c) FFA1 tip

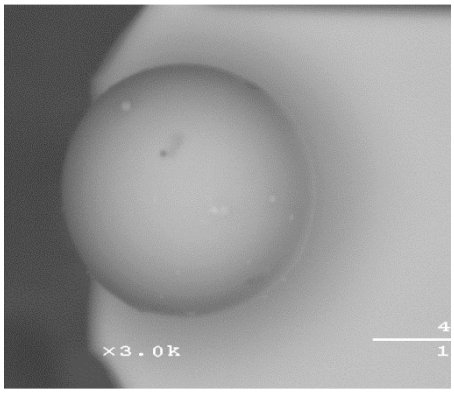

d) FFA2 tip

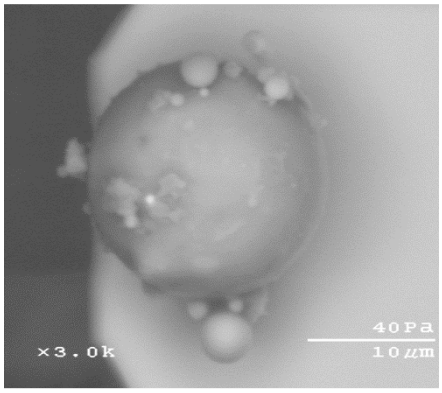

e) FFA3 tip

Figure 3.14. SEM images of PC and fly ash particles attached to the end of the rectangular AFM cantilever

Six sets of microscope slide samples were prepared, PC, CFA, FFA1 to FFA3 and GGBFS. PC and GGBFS were mixed with fast setting epoxy, adhered on glass slides, and then polished to make a flat surface as described in Section 3.3.1, while the fly ashes were adhered to a glass slide with a thin film of UV cured epoxy. The AFM scans of the sample surfaces are shown in Figure 3.15. The scan sizes were 5×5 μm and the average RMS roughness are from five particles.

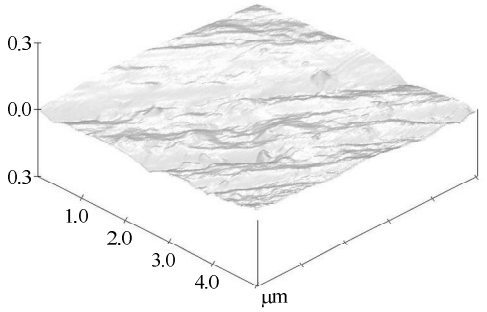

PC, RMS_{ave} = 11.2nm

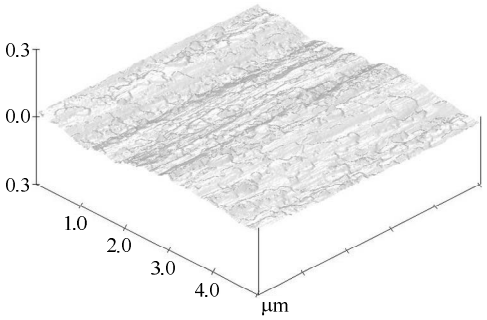

GGBFS, RMS_{ave} =19.8nm

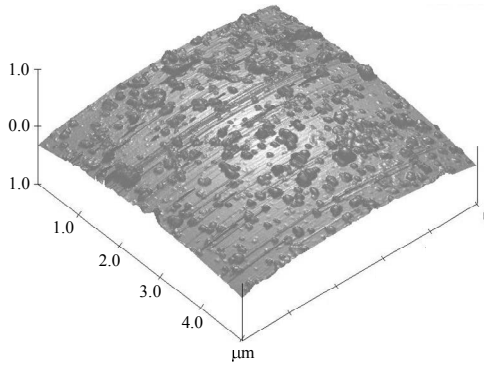

CFA, RMS_{ave} =28.3nm

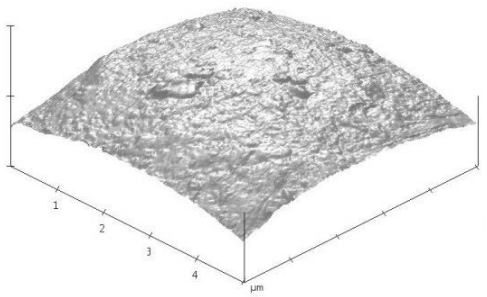

FFA1, RMS_{ave}=16.2nm

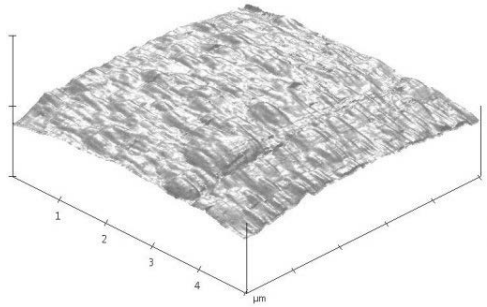

FFA1, RMS_{ave}=21.9nm

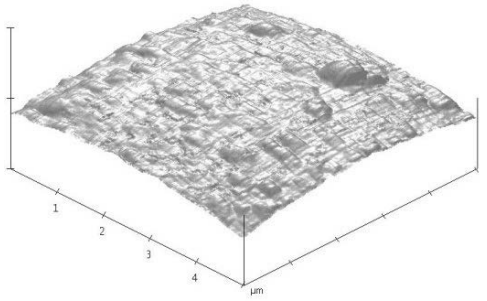

FFA1, RMS_{ave}=25.3nm

Figure 3.15. AFM scanned image of the sample surfaces, along with RMS roughness

3.4.2 Adhesion Forces and Hamaker Constant

The adhesion forces of the cementitious materials were measured in dry air and water, similar to Section 3.3.1. In addition, measurements were also made in a solution of sodium hydroxide with pH values of 8, 9, 11 and 13. The change in pH value of the surrounding fluid may change the adhesion force between particles, and was thus tested. In the study conducted by Plassard, et al. (2005) on calcium silicate hydrate (C-S-H), it was found that an increase in pH value increases C-S-H cohesion.

Adhesion force measurements were performed in the following combinations: PC-PC, PC-GGBFS, CFA-PC, CFA-GGBFS and CFA-CFA, FFA1-FFA1, FFA2-FFA2 and FFA3-FFA3. The first symbol denotes the probe tip while the second denotes the sample fixed on the slide. The testing sequence for adhesion and friction testing is in the order given in Table 3.8.

Table 3.8. Test sequence using cementitious particle probe

No	Test type	Environment
1	adhesion	dry air
2	friction	dry air
3	adhesion	pH 7,8,9,11,13
4	friction	pH 7,8,9,11,13

The probe tips were scanned before and after testing. To do this, a commercial Si_3N_4 AFM probe was glued to a slide with the tip facing upward. The probe tips were then scanned on the inverted Si_3N_4 tip. Samples of probe tip scans from the different tips are shown in Figure 3.16. Friction force testing was done immediately after the adhesion force measurements, thus the probe tip images that were taken after testing in solution were after friction force measurements. As seen, there is only a slight change in tip morphology after testing. Friction testing is discussed in the next section.

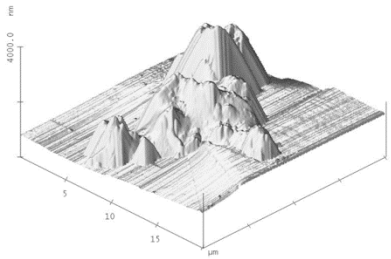

PC before testing

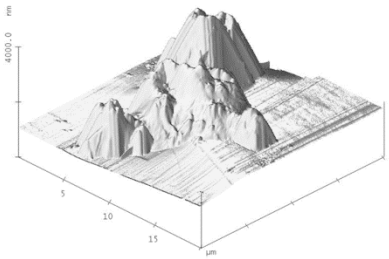

PC after testing in solution

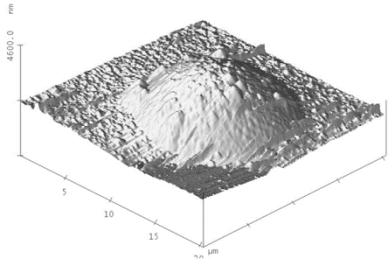

CFA before testing

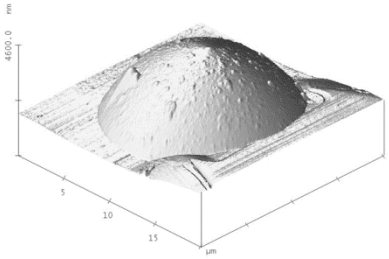

CFA after testing in solution

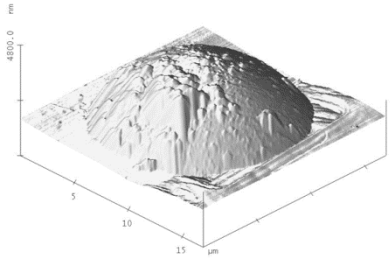

FFA1 before testing

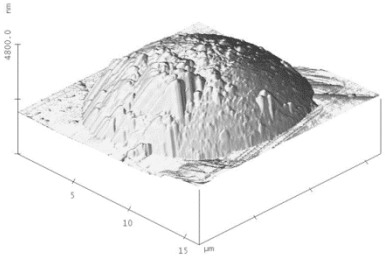

FFA1 after testing in solution

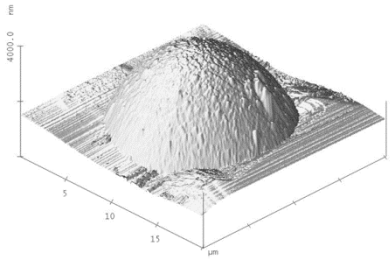

FFA2 before testing

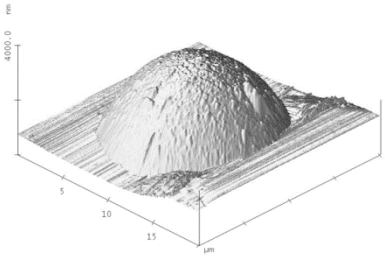

FFA2 after testing in solution

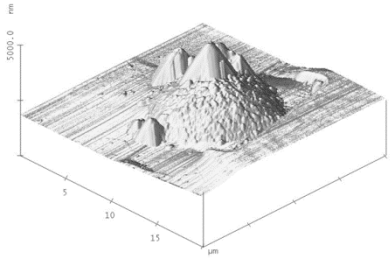

FFA3 before testing

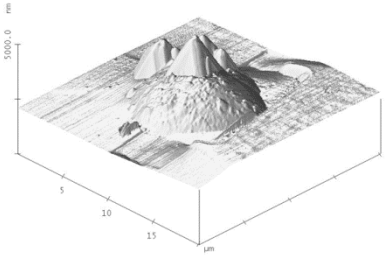

FFA3 after testing in solution

Figure 3.16. AFM scanned image of the AFM probe tips before and after testing

From the pull-off force measured in the tests, the Hamaker constants were calculated using the DMT model of Equation (3.6). The contact radius was calculated to consider multiple asperity contact by an equivalent area method, thus

$$R_{eq} = \left(\sum_{i=1}^{n} R_i^2 \right)^2 . \tag{3.10}$$

The asperities were identified by peak analysis using the software Scanning Probe Image Processor (Image Metrology, 2003). The asperities were peaks of the scanned particle. The radius of each asperity was measured.

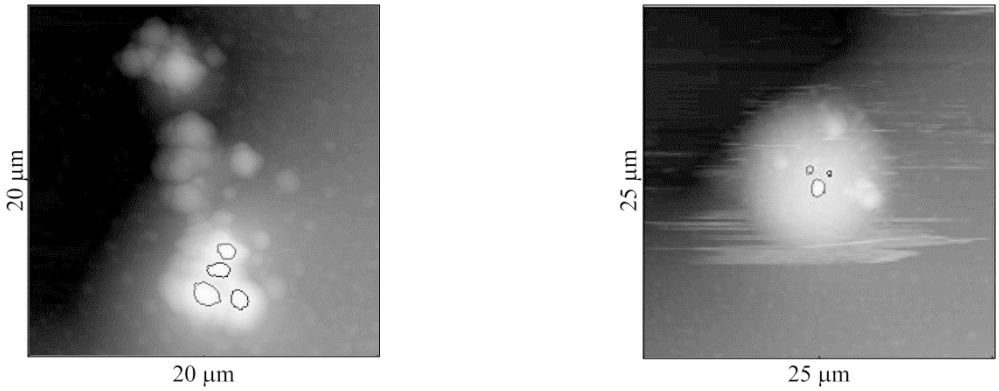

a) Asperities on Portland cement b) Asperities on fly ash

Figure 3.17. Asperities encircled on particle tips attached to AFM probes

The computed Hamaker constants in dry air are shown in Figure 3.18, and the computed Hamaker constant in water (pH 7) and sodium hydroxide solution (pH 8, 9, 11 and 13) Figure 3.19. In the tested materials PC, FFA2 and FFA3 have similar Hamaker constant. The Hamaker constants between dissimilar materials were higher that the individual materials. This may be due to the large difference in the interatomic distance D_0 between similar and dissimilar materials. It should be noted that D_0 was assumed to be the same for all materials because it was not measured in the present method. There was no specific trend in change in Hamaker constant with pH. The Hamaker constant of PC ranges from 0.05 to 0.12 $\times 10^{-20}$J. The Hamaker constants of fly ashes are generally lower than PC at high pH levels and decreases at the pH of 13. Similar to the tests in air, the Hamaker constant of CFA-PC in water is higher than PC-PC and CFA-CFA. A higher Hamaker constant indicates a higher

van der Waals adhesion force. A higher adhesion force would increase yield stress and viscosity. Based on the relative values Hamaker constants of the tested materials, there will be additional viscosity and yield stress because of van der Waals force when CFA is added to PC due to CFA-PC interaction. The van der Waals interaction between PC and GGBFS does not contribute to change in viscosity and yield stress.

Typical values of pH for concrete are 12 to 13. This would mean the values of Hamaker constants in Figure 3.19 that are within this pH range can be used for simulation of flow of cementitious pastes.

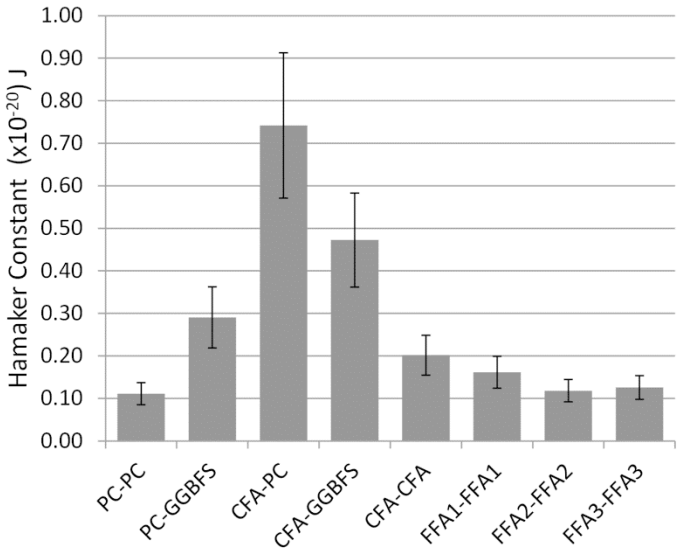

Figure 3.18. Hamaker constants of cementitious materials in dry air

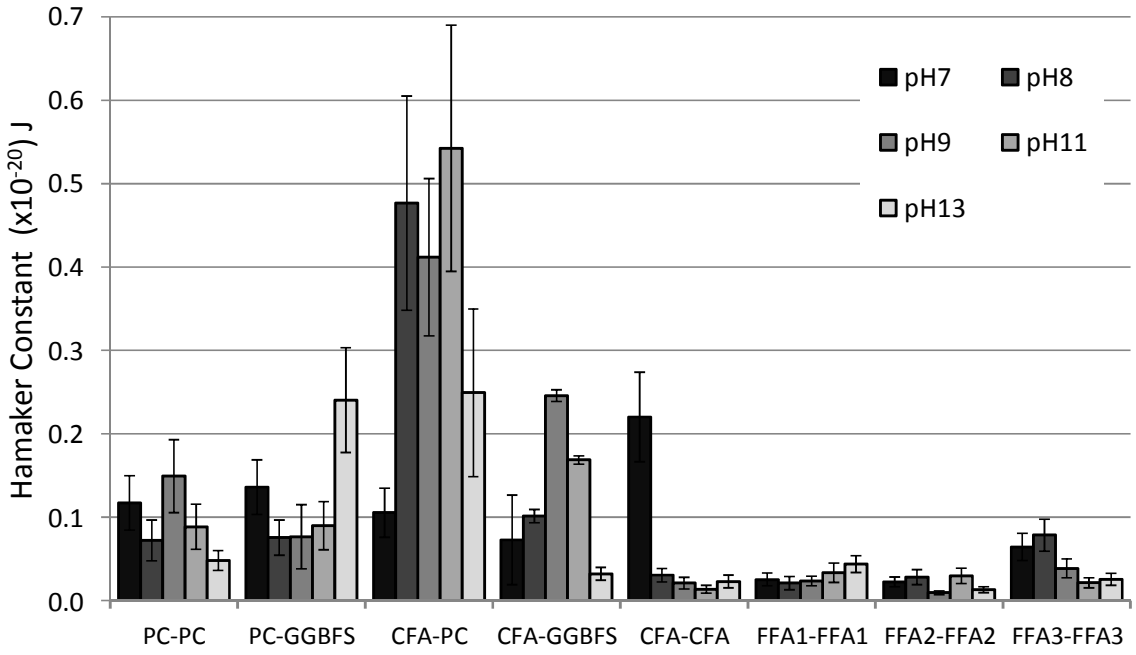

Figure 3.19. Hamaker constants of cementitious materials in water (pH7) and solution of sodium hydroxide (pH 8, 9, 11, 13)

3.5 Friction of Cementitious Materials

3.5.1 AFM probes and sample preparation

The AFM probe and sample preparation are similar to those described in Section 3.4.1. Since friction measurements are to be done by sliding particles against each other, the particles may degrade, and the worn material may transfer between the tip and the sample. Therefore, images of the probes used were taken with an SEM before and after the friction tests to check for the tip wearing or deterioration. There was no deterioration observed in the before and after images of the tips used. Fresh tips were used for each test to avoid material contamination due to material transfer during testing.

3.5.2 Friction measurement

The test method introduced by Ruan and Bushan (1994) using friction force microscopy is employed to determine the coefficient of friction between two cementitious materials at the micro-scale in the present study. To begin the friction force measurement, the

geometry of the probe Lc and ht in equation (2.9) were first determined. Lc was measured with an optical microscope while ht was measured using an SEM.

For the friction tests in dry air, the probe and sample were mounted in the AFM and the AFM chamber was closed and purged with N_2 gas until it had a RH $\leq$ 10%. The probe then was brought down to the sample until the tip contacted the sample, as shown in Figure 3.20. The zero deflection set-point and the pull-off deflection was then determined. When the tip is pressed by the cantilever against the slide sample, the normal force will be the sum of the force exerted by the cantilever and the adhesion force between the tip and the sample. The zero deflection set-point will have a normal force that is only due to adhesion. The pull-off deflection is the amount the AFM cantilever deflects before the tip of the cantilever separates from the sample on the slide as the AFM probe is withdrawn away from the sample. It measures the adhesive force acting between the probe tip and the sample, which is computed from the cantilever pull-off deflection multiplied with the cantilever stiffness.

For the friction test in fluid environment, the test was started with pH 13. Line scans were done on the current solution to obtain friction data. When the line scans were completed in the solution, the pH was then decrease to pH 11. The process was repeated until pH 7 (water) was tested.

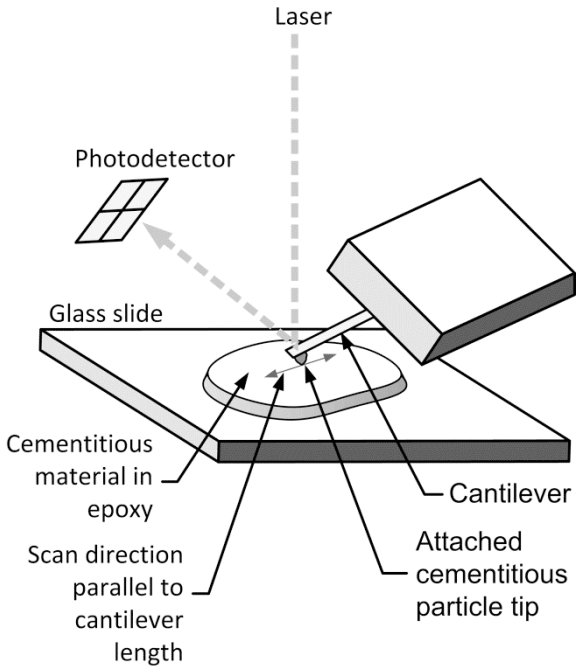

Figure 3.20. Schematic of set-up for friction measurement using AFM

A line scan was then performed on the sample. The sliding distance for the tip was 5 μm. The H_0 and (ΔH_1+ΔH_2) at given deflection set-points were recorded. Five readings were recorded per deflection set-point. H_0, ΔH_1 and ΔH_2 were in units of volts. This was converted to nanometer with the AFM z-scan sensitivity. The deflection set-point was varied for an increasing normal load, from a set-point less than zero (adhesion regime) to ~100 nN exerted by the cantilever. Figure 3.21 shows the increase in normal load with increasing set-point. Figure 3.22 shows the increase (ΔN_1+ΔN_2) with increasing set-point due to increasing normal load and friction force. It can be observed that near the adhesion regime, there is a non-linear increase in (ΔN_1+ΔN_2). This is due to the large change in contact area at very low normal loads. To compare the results with macro-scale coefficient of friction, only the linear part of the curve was used in the calculation of the coefficient of friction.

To calculate the coefficient of friction with equation (2.8), the slope of the curve in Figure 3.21 (ΔN/Δset-point) and the slope of the curve in Figure 3.22 ($\Delta(\Delta N_1+\Delta N_2)$ /Δset-point) are used. Equation (2.8) then becomes

$$\mu = \frac{f}{N} = \frac{\Delta(\Delta N_1 + \Delta N_2)}{\Delta\text{set-point}} \frac{\Delta\text{set-point}}{\Delta N_0} \frac{L}{2l} . \tag{3.11}$$

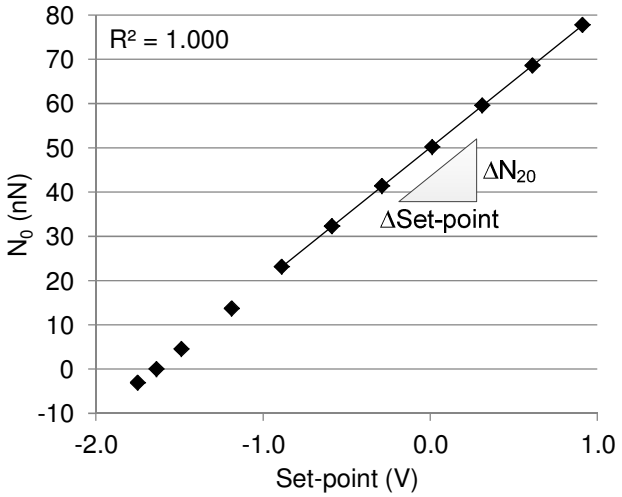

Figure 3.21. Normal force due to cantilever deflection with increasing deflection set-point

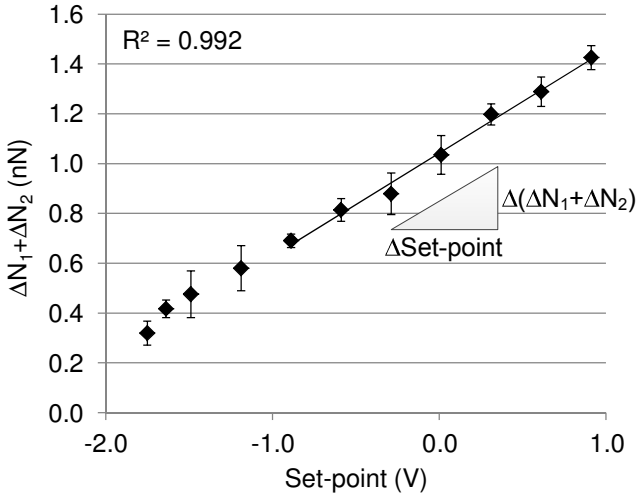

Figure 3.22. Normal force changes when probe is traveling parallel with the probe long axis with increasing deflection set-point

3.5.3 Micro-scale Friction

The micro-scale coefficient of friction for different cementitious material combinations are given in Figure 3.24. The first material in the labels is the particle at the AFM tip and the other is the sample on the slide. The coefficient of friction ranges from 0.020 to 0.059. It can be observed that coefficient of friction involving FA is high. FA against FA has the highest coefficient of friction among the material combinations tested. This may be due to the asperities on the surface of the fly ash particles shown in Figure 3.15c. A schematic drawing of how the surface conditions and asperities of PC and FA tips interact with PC, FA and GGBFS particles on slides is shown in Figure 3.23. . The surface features of the interacting particle affects the frictional resistance of the particle to sliding. PC and GGBFS particles on a slide were polished flat, thus had small asperities. This surface feature offers little resistance to sliding with a PC tip as shown in Figure 3.23. a. In Figure 3.23. b, the asperities on the surface of FA particles tend to hinder sliding because of their hill-like shape, thus resulting in a high coefficient of friction. The additional frictional resistance was attributed by Sundararajan and Bhushan (2000) as the ratchet mechanism of friction and collision force on the asperities. In the case of FA sliding against PC or GGBFS, Figure 3.23. c, the asperities of FA particles collides with the small asperities of PC or

GGBFS causing a resistance to sliding greater than PC-PC or PC-GGBFS, but less than FA-FA.

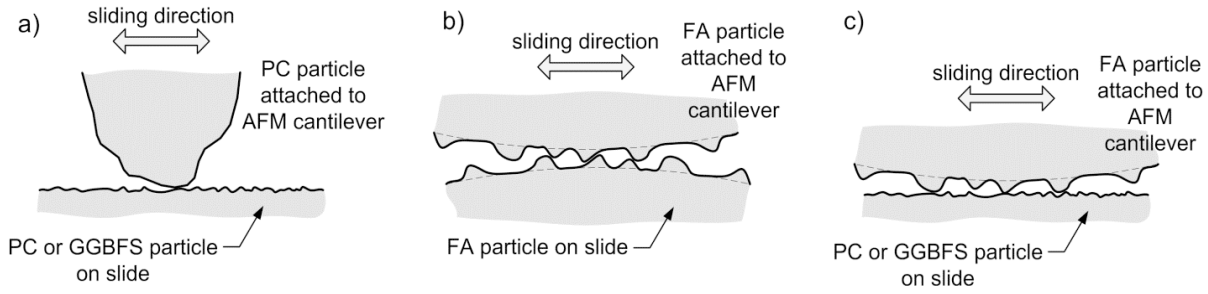

Figure 3.23. Schematic of AFM particle tip sliding against sample on slide; a) PC-PC and PC-GGBFS, b) FA-FA, c) FA-PC and FA-GGBFS

The coefficient of friction is plotted against the pull-off force between the tested materials in Figure 3.25. It can be observed that the pull-off forces are significantly higher for the PC-GGBFS. The pull-off force for the PC-GGBFS ranged from 64.2 to 161.4 nN, while the range of pull-off forces for the other cementitious materials was from 5.9 to 40.5 nN. The pull-off force measures the adhesion force between the tested materials. This force will be present during the coefficient of friction measurement. As observed by Bhushan and Sundararajan (1998), the measured coefficient of friction may be reduced due to high adhesion forces, which may result in the observed low coefficient of friction for PC-GGBFS.

The coefficients of friction in solution with different pH are given in Figure 3.26. There is no significant change in coefficient of friction with change in pH. As shown, the coefficient of friction of PC is higher than other cementitious materials tested. The coefficient of friction of CFA and CFA with GGBFS is second highest compared to PC, which may be due to high average surface roughness given in Figure 3.15. The lowest coefficient of friction is from FFA1, which has the lowest average RMS.

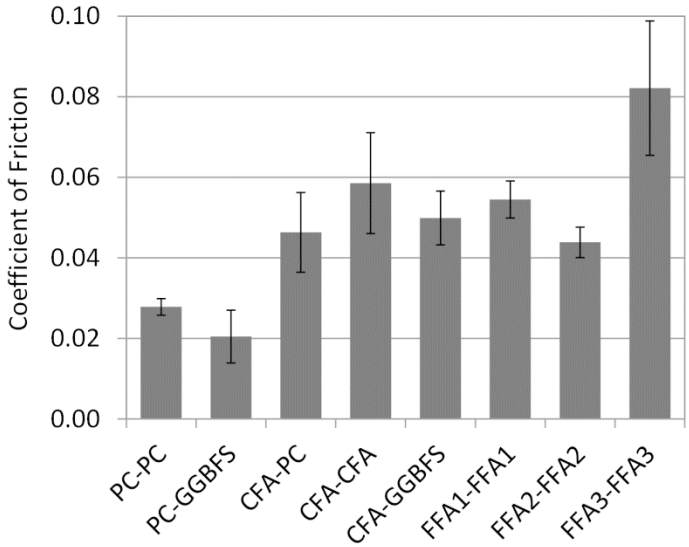

Figure 3.24. Micro-scale coefficient of friction of cementitious materials in dry air

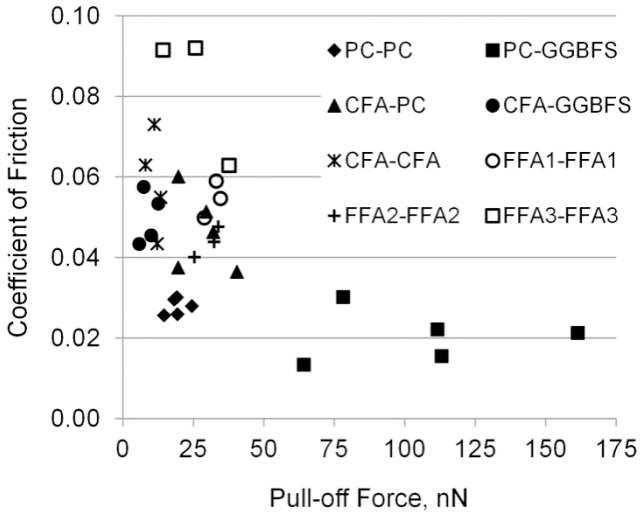

Figure 3.25. Effect of pull-off forces on micro-scale coefficient of friction of cementitious materials

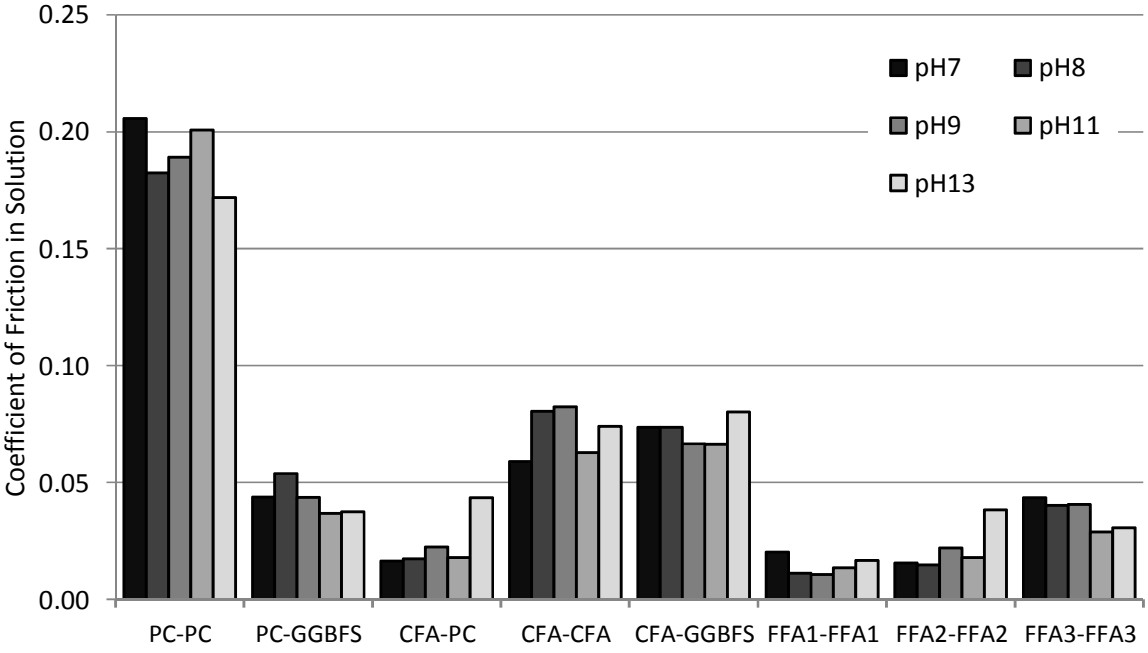

Figure 3.26. Micro-scale coefficient of friction of cementitious materials in solution

CHAPTER 4. RHEOLOGY OF CEMENTITIOUS MATERIALS AT THE MACRO-SCALE

4.1 Introduction

The first part of this Chapter presents the compression and shear behavior of cementitious powders at its dry state. At cement manufacturing and concrete ready mix plants, cementitious materials are often packed in bags or stored in barrels or silos before being transported and distributed. During storage and transport, the bulk materials are subjected to fluffing, consolidation, filling into and discharging from containers. The compression and shear properties of the cementitious materials as well as their friction with contacting walls greatly affect the easy/difficulties of the materials to be handled (Schulze, 2008).

For construction, bulk cementitious materials are transported by rail, truck or ship from manufacturing plants to ready mix concrete plants or construction sites. Pressurized air through pipe is commonly used for loading and unloading of the transport vehicle (Kosmatka et al., 2003). When cementitious materials are passed through a pipe, their flow behavior and the material-pipe interaction are crucial. Research has found that factors affecting the flow behavior of dry materials include particle stiffness (Campbell, 2006; Aarons and Sundaresan, 2006), mean particle size, shape and distribution, bulk and particle density (Littman et al., 1995; Mills, 2004). To ensure proper transportation and avoid blockage, it is required in practice that the pipe used shall be flexible and free to vibrate, sufficient pressure shall be supplied along the pipe, and sharp bends in the pipe shall be prevented.

Although a large amount of cementitious materials are used each year, little is known with regards to their bulk flow and storage properties. Many problems, such as bridging, ratholing, flooding or uncontrolled flow, and caking, have occurred, which negatively impact the material production efficiency (Maynard, 2004).

The second part of the Chapter presents that rheology of freshly mixed cementitious pastes. Cementitious paste in concrete is composed of Portland cement and water, and other types of cementitious materials such as fly ash, ground granulated blast furnace slag and silica fume and other chemical admixtures. In the fresh state of concrete, the paste fills the space between aggregates, suspends the aggregates in place when the concrete is static and promotes flow by providing a distance between aggregates and may also serve as lubrication between contacting aggregates (Kennedy, 1940; Oh et al., 1999). In hardened concrete, it is the matrix that holds the aggregates together.

Paste in fresh concrete contributes to its workability and rheology, which influences concrete placement methods, quality of cast concrete and hardened properties. Rheology parameters could be used to evaluate the flowability and compactability of fresh concrete (Yen et al., 1999; Gjorv, 1998). Rheology parameters in pastes that are of interest are viscosity, yield stress and thixotropy. Factors affecting the rheology of paste include concentration of solids, interparticle forces by cohesion and friction, particle size, distribution and morphology (Ferraris et al., 2001; Cry et al., 2000; Park et al., 2005).

The specific surface area and concentration of solids was shown to influence the viscosity and yield stress of cement pastes (Vom Berg, 1979). The viscosity and yield stress increases with fineness and concentration, which reflects on the dominance of water-cement interface in the system. It has also been shown that fly ash improves workability, which has been attributed to particle geometry (Rudzinski, 1984). Particle size distribution, density and morphology are major factors affecting viscosity (Li et al., 2004). The viscosity and yield stress affect the consistency, stability and consolidation of concrete mixtures.

Thixotropy in cement based materials is mainly attributed to the colloidal interactions of cementitious particles (Coussot, 2005); the aggregates in concrete are inert non-colloidal particles. Cementitious materials build colloidal structures while at rest, either by flocculation or hydration. The colloidal structures are broken by shearing. The structure breaking changes the viscosity of paste during constant shearing, developing a thixotropic paste. Thixotropy of cement base materials is influenced by timescales (Jarny et al., 2005). Reversible flocculation and de-flocculation dominates flow at short timescales, while irreversible hydration process dominates at large timescales. Some of the influences of

thixotropy in concrete construction are formwork pressure, multilayer casting and stability (Roussel, 2006).

4.2 Materials

Four types of cementitious materials were studied, ordinary Portland Cement (PC), Class C Fly Ash (FA), Ground Granulated Blast Furnace Slag (GGBFS) and densified Silica Fume (SF). PC is a hydraulic cement composed primarily of calcium silicates. FA, GGBFS and SF are supplementary cementitious materials. When used in conjunction with PC, they contribute to the properties of the hardened concrete through hydraulic or pozzolanic activity or both. The chemical composition, specific gravity (ASTM C188, 2009) and fineness (ASTM C204, 2011) of the cementitious materials are given in Table 4.1. The chemical composition was obtained by x-ray florescence spectroscopy. PC has the highest specific gravity among the material, while the fineness of PC and GGBBS are similar.

Since the geometry of the materials will have an effect on its bulk density and shearing behavior, scanning electron microscope (SEM) micrographs are shown in Figure 4.1. PC and GGBFS are angular due to grinding during production. FA has spherical shaped particles, which are formed by fusing in suspension of exhaust gases. SF has an irregular and rounded shape. Densified silica fume is an agglomeration of silica fume. Undensified silica fume are condensed from vapor and its particles will a size less than one micron (Holland, 2005).

The cementitious materials were placed in an oven at 212 ºF for 24 hours and allowed to cool in the oven before using in compression and shear testing. The preparation of samples in testing boxes and compression and shear testing were done at a relative humidity of 50% and temperature of 73±3 ºF.

Table 4.1. Chemical components (%), specific gravity and fineness (m^2/kg)

	Material			
	PC	FA	GGBFS	SF
Na_2O	0.1	1.64	0.29	
MgO	3.07	4.87	9.63	
Al_2O_3	4.24	17.68	8.54	
SiO_2	21.16	31.92	36.5	85-97
SO_3	2.63	1.68	0.6	
K_2O	0.66	0.43	0.44	
CaO	64.39	30.9	41.1	<1
Fe_2O_3	3.07	6.54	0.83	
Others	0.68	4.34	2.07	
Specific Gravity	3.14	2.52	2.95	2.21
Fineness (m^2/kg)	452.7	419.6	455	314.8

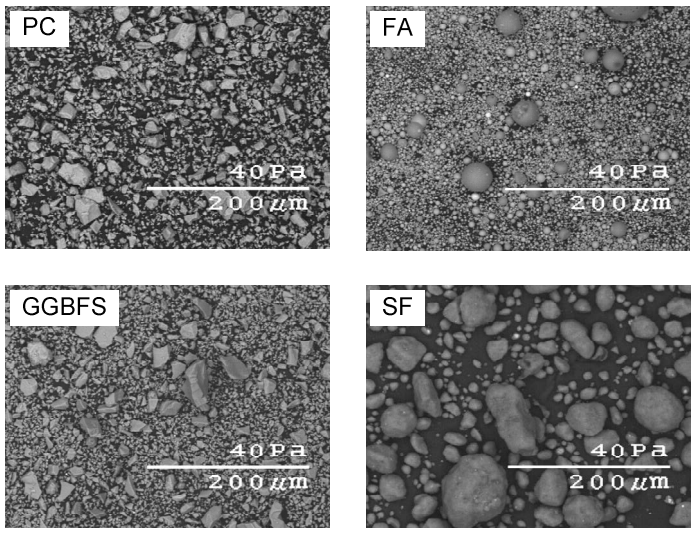

Figure 4.1. SEM micrograph of cementitious powders

4.3 Compression and Cementitious Materials in Dry State

Prior to performing the compression loading of the cementitious materials, the densities of the bulk materials were measured after the samples were prepared for testing.

The compression test was to determine the compressibility and stiffness modulus (E) of cementitious materials. The test was confined and uniaxial. The material was placed in a rigid box and was loaded in only one direction. The materials were tested pure and blended. The blended materials were PC with FA, GGBFS or SF. The amounts of FA, GGBFS and SF in the blended materials were 20, 40, 60 and 80 % by weight.

4.3.1 Compression Test Methods

Bulk Density Measurement

The bulk densities of the cementitious materials were determined using a 100×100×50 mm rigid box. The bulk density is measured after the sample has been prepared for compression, prior to loading. Simple pluviation of the cementitious material in the box produced a very compressible sample because the materials were in loose dry powder form. The initial deformation of the sample was too high to be measured with an LVDT. To reduce the initial compression, the sample was pluviated and consolidated in three layers in the box. The consolidation pressure was 4.1 kPa. The sample was then vibrated for one minute with 4.1 kPa pressure as shown in Figure 4.2. The sample was then weighed and the height at four corners was measured. The dimensions were measured using a caliper.

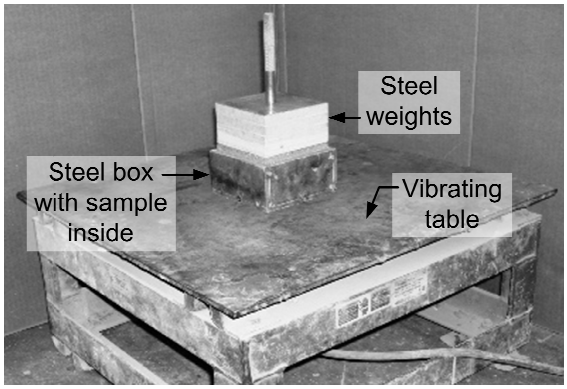

Figure 4.2. Setup for consolidation and vibration for sample preparation

The bulk density ρ_b was calculated as the weight of the prepared sample W_{sample} divided by its volume. The height of the sample h_{ave} was the average of the heights measured

at four corners of the box. The width w and length l of the sample were the inner width and length of the box.

$$\rho_b = \frac{W_{sample}}{w \times l \times h_{ave}} \tag{4.1}$$

Since the samples tested were composed of one or two types of materials with different specific gravities, the amount of voids in the samples gives an indication of the degree of packing and the amount a sample may compress. Reduction in bulk volume is predominantly reduction in volume of voids V_v (Lambe and Whitman, 1969). The void ratio e of a sample can be solved by

$$e = \frac{V_v}{V_s} = \left[\left(\frac{W_{OPC} + W_2}{\rho_b} \right) \Big/ \left(\frac{W_{OPC}}{G_{OPC}\rho_{water}} + \frac{W_2}{G_2 \rho_{water}} \right) \right] - 1 \tag{4.2}$$

V_s is the volume of cementitious materials. W_{PC} is the percentage of PC by weight and W_2 is the percentage of FA, GGBFS or SF by weight. G is specific gravity given in Table 4.1 and ρ_{water} is the density of water.

Compression testing

The setup for the uniaxial compression test is shown in Figure 4.3. The cementitious material to be tested was placed and covered with a rigid box and plate. The interior dimensions of the box was 100×100×50 mm. Steel plates were placed on a hanger to produce the compressive load. The sample deformation was measured using a Linear Variable Differential Transducer (LVDT). The LVDT was set at the center of the sample. An increasing compressive load at 6.1, 8.9, 15.2, 27.8 and 52.4 kPa was then placed on the sample. Deformation readings were taken on the LVDT every five seconds. The final deformation for the respective load was recorded when there was no change in five consecutive readings. After loading to 52.4 kPa, the sample was subjected to a cyclic loading of 6.1 kPa to 52.4 kPa. The displacement for each cycle was recorded. The test was stopped when there was no significant change between two consecutive cycles.

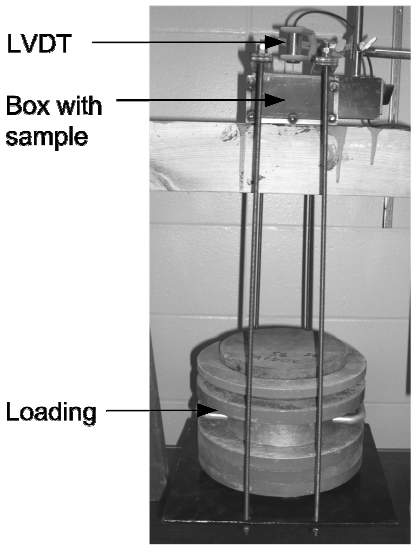

Figure 4.3. Setup for compression of bulk cementitious materials

A stress-strain curve was produced when the sample was loaded compression as shown in Figure 4.4. The sample strain (ε) was the sample deformation divided by the height of the sample before loading. The three segments in the graph can be described by two characteristic behaviors, the normal compression line (NCL) and the swelling and recompression line (SRL) (Whitlow, 2001). NCL represents loading to stresses higher than any previous value on the sample. When the sample was unloaded, it swelled along the SRL and when reloaded it compressed along the same path. When the sample was compressed and was along the NCL, the sample strains from particle rearrangement due to sliding or fracturing. The strain due to rearrangement was not recoverable. The portion of strain that was recovered and exhibited by the SRL during unloading was caused by the elastic energy within individual particles as the sample was loaded (Makkawi et al., 2006). The rearrangement and fracture of particles in the NCL versus mainly elastic deformation in the SRL also explains why the slope of a NCL was less than the slope of a SRL. Thus, the sample became behaves stiffer when loads are lower than previous loads it had experienced. SRL_1 was due to the loading from sample preparation while SRL_2 was due to the cyclic loading applied.

Typical SRL_2 of samples is shown in Figure 4.5. The graph shows two cycles of recompression and swelling, curves a-b-c and c-d-e. The recompression portion of the graph

(a-b and c-d) showed a nonlinear relationship between stress and strain while the stress-strain relation in the swelling line was linear, when plotted in the log(σ)-strain axes. There was a small amount of unrecoverable strain during recompression and swelling, distances a-c and c-e.

Four parameters were calculated to describe the compression properties of the bulk cementitious materials, the compression index C'_c, the swell index C'_s, the recompression index C'_r and stiffness modulus E_s. The compression index is the slope of the NCL shown in Figure 4.4. The swell and recompression indices are the slopes of the recompression and swell lines in the SRL shown in Figure 4.5, respectively. The stiffness modulus is the ratio of the increment in stress to the increment in strain. The amount of compressibility in a given state of the cementitious material, normal compression, swell or recompression is proportional to the corresponding index, and the stiffness modulus. The formula for C'_c, C'_s and $C'r$ are similar. The following equations for the four parameters apply:

$$C'_c = \frac{\Delta\varepsilon}{\log(\sigma_2/\sigma_i)}, \quad C'_r = \frac{\Delta\varepsilon}{\log(\sigma_2/\sigma_i)}, \quad C'_s = \frac{\Delta\varepsilon}{\log(\sigma_2/\sigma_i)} \tag{4.3}$$

$$E_s = \frac{d\sigma}{d\varepsilon} = \frac{\sigma_2}{C'_s} \tag{4.4}$$

$\Delta\varepsilon$ is the change in strain from σ_2 to σ_i, where σ_i is any stress along the appropriate curve. For this study, σ_2 was 52.4 kPa. To calculate C'_c in each sample, σ_i was 15.2 kPa and $\Delta\varepsilon$ was the change in strain from 27.8 to 52.4 kPa. C'_r and C'_s in each sample were calculated as the average from the two hysteresis in Figure 4.5. $\Delta\varepsilon$ for C'_r were ε_b-ε_a and ε_d-ε_c and $\Delta\varepsilon$ for C'_s were ε_b-ε_c and ε_d-ε_e. σ_i for C'_r and C'_s was 6.1 kPa. E_s was the calculated from the swell line of SRL_2.

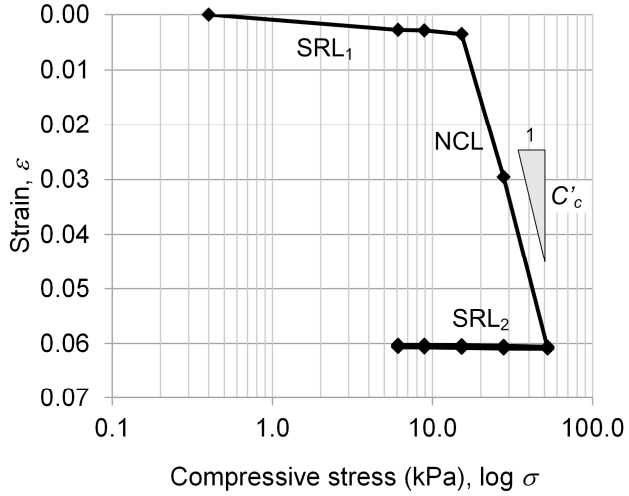

Figure 4.4. Strain vs. log(stress) curve of cementitious sample under compression loading

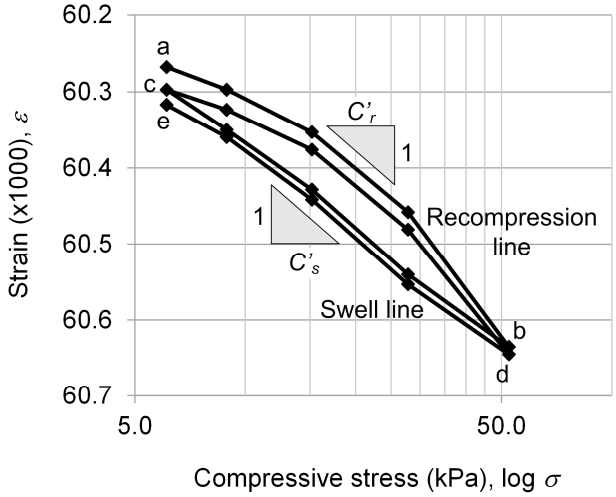

Figure 4.5. SRL strain vs. log(stress) curve of cementitious sample

4.3.2 Compression Test Results

Bulk density results

The bulk density of the pure cementitious materials and the combination of PC with FA, GGBFS or SF are presented in Figure 4.6. Zero percent PC content indicates pure FA, GGBFS or SF. The results show that the density of PC with FA does not change with

increasing FA content. The replacement with GGBFS or SF reduces bulk density, with greater reduction for SF compared to GGBFS.

The void ratios of samples computed with equation (4.2) are given in Figure 4.7. The void ratio of pure materials PC, GGBFS and SF is greater than one. The amount of voids is lowest for FA which may be due to its spherical shape. The amount of voids for GGBFS is greater than PC. GGBFS has similar fineness compared to PC, but a smaller specific gravity. This would indicate that GGBFS would have a higher angularity and would thus create larger voids compared to PC. The densified silica fume SF has the largest amount of voids because of the densified particles.

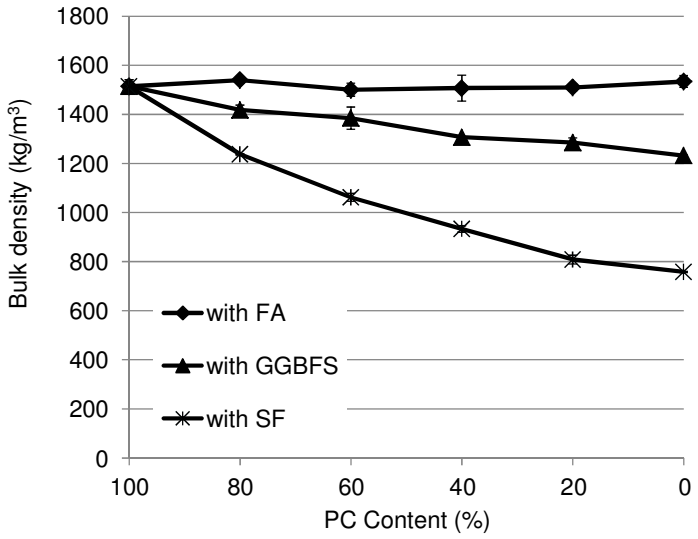

Figure 4.6. Bulk density of cementitious materials

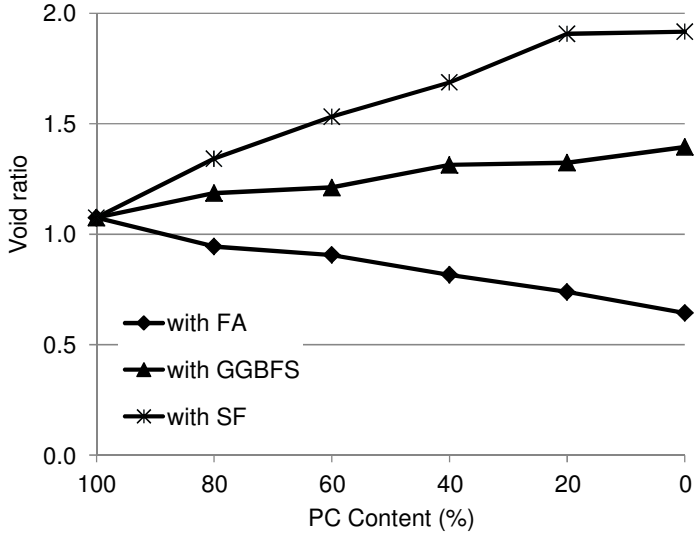

Figure 4.7. Void ratio of cementitious materials

Table 4.2. Bulk density, void ratio, compression/recompression/swell indices, stiffness modulus and coefficient of friction of PC with SF

PC Content (%)	ρ_b (kg/m^3)	e	C'_c	C'_r (×1000)	C'_s (×1000)	E_s (MPa)	μ
90	1368.4	1.20	0.234	1.159	0.996	73.206	0.74
95	1412.3	1.18	0.264	0.801	0.716	52.600	0.75

Compression test results

The compression, recompression and swell indices and the stiffness modulus of the cementitious materials are given in Figure 4.8 to Figure 4.11, respectively. The compression index does not change increasing FA content. From the initial condition of PC- FA blends having decreasing void ratio with increasing FA content in Figure 4.7 and the trend of compression index with increasing FA content, the replacement with FA contributes to good packing of particles when loose and when subjected to compressive loads. This may be attributed to its spherical shape. There is a significant increase in compression index with increasing GGBFS content. This indicates that GGBFS has a large voids when loosely placed but is susceptible to packing when subjected to compressive loads. The compression index

decreases with increasing SF content. Since the void ratio increases and the compression index decreases with increasing SF content, SF inhibits packing whether loosely placed or consolidated with compressive loads. This is due to the higher particle size of the densified SF compared to the other cementitious materials.

In storage of cementitious blends, the upper portion of the materials would follow the density trends shown in Figure 4.6, however, the deeper part of the materials in silos will be more consolidated due to overburden pressure. Since the compression index of PC-FA blends do not change, increase in the amount of FA in a blend will give similar densities for the same overburden pressure. For PC-GGBFS blends, it will compress less with increasing GGBFS and would have lesser density for a given overburden pressure. This may lead to greater materials storage for PC-FA blends compared to PC-GGBFS blends.

The trends of C'_r and C'_s in Figure 4.9 and Figure 4.10 of the cementitious materials are similar. The indices are not changed with increasing FA content, slightly increases with increasing GGBFS content and significantly increases with SF content. In all cases, C'_r is slightly higher than C'_s. This would be due to a slight unrecoverable strain during the recompression and swell hysteresis. The amount of elastic energy that can be stored in PC and FA are similar. GGBFS can store up to 38% lesser elastic energy compared to PC, while SF stores up to 450% lesser elastic energy compared to PC.

Since the stiffness of the bulk materials is inversely proportional to the swell index in equation (4.4), the stiffness decreases with replacement with GGBFS and SF. The stiffness of SF is much less than the stiffness of PC, FA and GGBFS. This is mostly related to the poor packing of SF compared to the other cementitious materials.

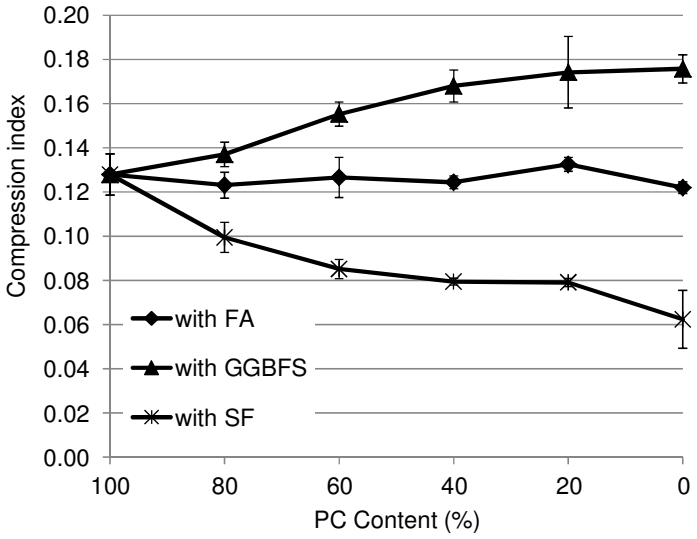

Figure 4.8. Compression index of cementitious materials

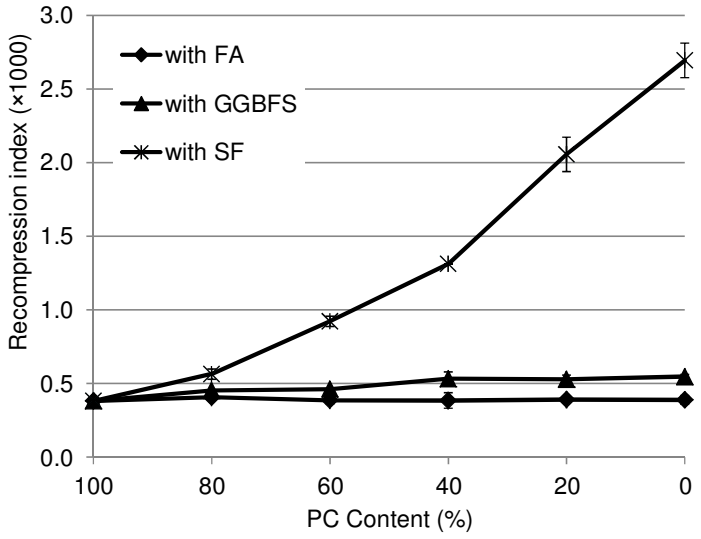

Figure 4.9. Recompression index of cementitious materials

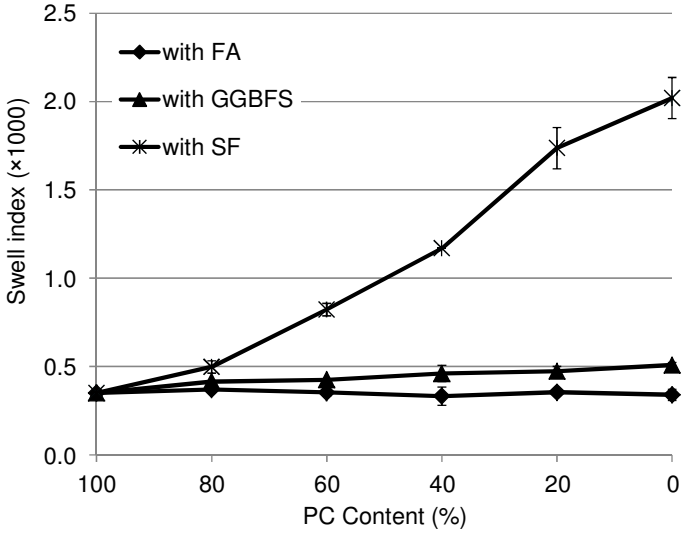

Figure 4.10. Swell index of cementitious materials

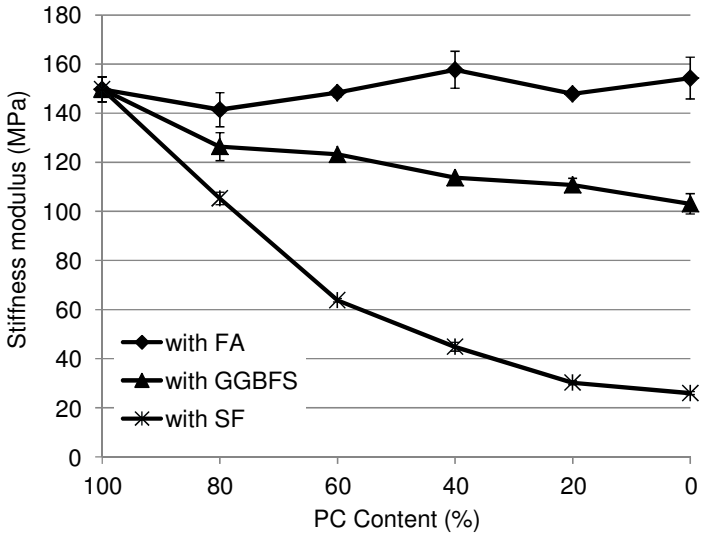

Figure 4.11. Stiffness modulus of cementitious materials at σ = 52.4 kPa

4.4 Shear of Cementitious Materials in Dry State

The shear test was conducted to determine the bulk coefficient of friction (μ). The test was by direct shearing at different normal loads. The material combinations are the same as the test for compression in Section 4.3.

4.4.1 Shear test method

The setup for the uniaxial compression test is shown in Figure 4.12. The shear box used was 100×100×50 mm. When a sample was sheared, the lower half of the box moved forward while the upper half remained stationary. The lower half of the box was moved by a motor and the shearing force was measured with a load cell. Three LVDTs were used in the setup, two for the vertical displacement and one for the horizontal displacement. The normal load was applied with steel plates through a hanger.

The samples were consolidated in three layers in the shear box with a pressure of 4.1 kPa and then vibrated while maintaining the pressure. The two LVDTs for the vertical displacement were position above the sample along the sample, 25 mm from each edge. The sample vertical displacement was taken as the average of the readings from the LVDTs. The LVDT for the horizontal displacement was position in front of the lower portion of the shear box. A normal load was then placed on the sample. The normal loads for three shear tests of a sample were 13.1, 26.0 and 51.8 kPa. The shearing rate was 1 mm per minute. Displacement and force readings were taken every 15 seconds. The shearing was stopped when the lower portion of the box had moved 12.5 mm.

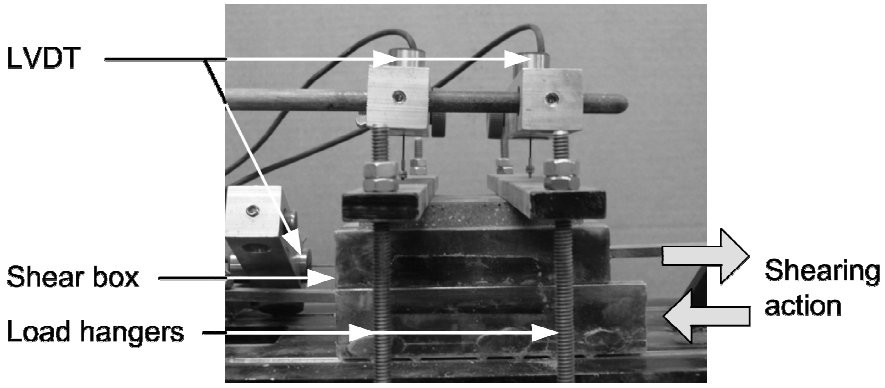

Figure 4.12. Setup for direct shear test of bulk cementitious materials

The typical increase in shear stress with increase in shearing displacement and normal loads for the cementitious materials tested is shown in Figure 4.13. The gradual increase in shear stress until it reaches its ultimate shear stress and stays at the peak value is typical of a loosely consolidated dry material, Lambe and Whitman (1969). The typical decrease in height of the samples tested is shown in Figure 4.14. This occurs due to net effect of large numbers of cementitious particles roll about and fall into voids in an initially loose arrangement. The change in sample height ε_h was expressed in terms of the change in height Δh and the original height h_0 of the sample after the placement of the normal stress, before the application of the shearing stress.

$$\varepsilon_h = \frac{\Delta h}{h_0} \tag{4.5}$$

To compute for the bulk coefficient of friction, the peak shear stresses τ_u were plotted against its corresponding normal stress (N) as shown in Figure 4.15. The bulk coefficient of friction μ is the slope of the regression line along the three points.

$$\mu = \frac{d\tau_u}{dN} \tag{4.6}$$

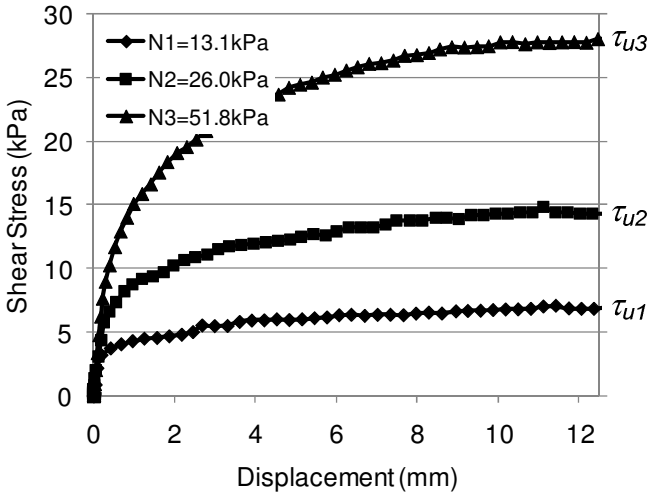

Figure 4.13. Shear stress vs. displacement curve of at increasing normal loads

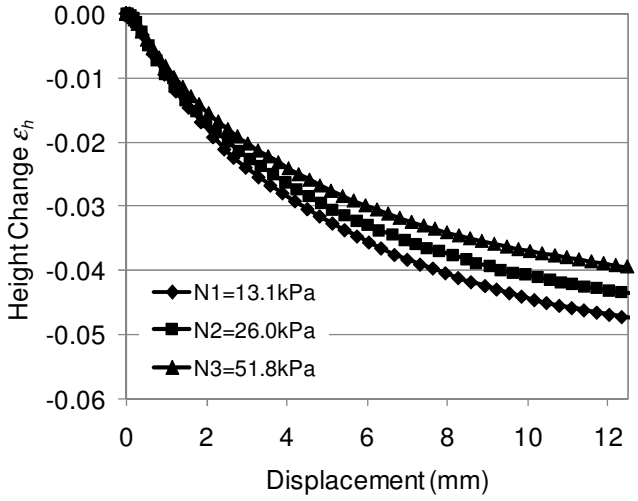

Figure 4.14. Change in height vs. displacement curve at increasing normal loads

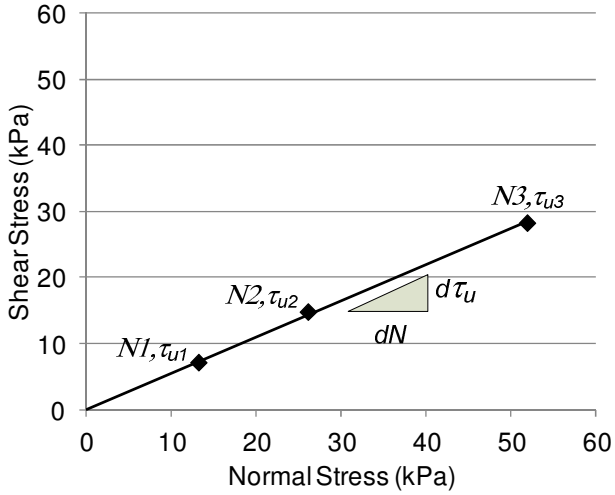

Figure 4.15. Peak shear stress vs. normal stress of cementitious sample

4.4.2 Shear Test Results

The results for coefficient of friction of the cementitious materials and PC combined with other cementitious materials are given in Figure 4.16. The coefficient of friction of FA is much less compared to the coefficient of friction of PC. There is a linear decrease in coefficient of friction of PC-FA blend and the FA. Although FA has a slightly larger average particle size compared to PC, based on the material fineness, FA particles has a spherical shape while PC has angular shape particles. The angular shape has a higher potential for

particle interlocking which may contribute to the higher coefficient of friction, while a spherical shape makes particles easy to move and pack.

The coefficient of friction of GGBFS is slightly less than that of PC. This is mainly because both are ground and have similar fineness. The increase in void ratio (in Figure 4.7) and decreasing bulk coefficient of friction with increase in GGBFS replacement indicate that the resistance of the blends to packing with small pressure may also be attributed to other factors such as the particle shape or angularity. The coefficient of friction of SF is greater than PC. When SF is combined with PC, the coefficient of friction of the combined materials reduces up to 60% replacement (40% PC content) but increases sharply increases after 60% replacement. The sudden increase may be due to the larger size of densified SF particles compared to PC particles that the interactions between SF particles dominate the shearing behavior while PC particles fill the voids between the SF particles. Due to the decreasing coefficient of friction with increasing replacement with FA and GGBFS, the dry flowability of PC-FA and PC-GGBFS blends will also increase. Only a slight increase in flowability is expected with increasing GGBFS, while a substantial increase is expected with increasing FA content.

The change in height of the samples at 12.5 mm shear displacement calculated by equation (4.5) is given in Figure 4.17. The change in sample height generally decreases with increasing FA, GGBFS or SF content. The behavior of PC with FA and SF are very similar while the decrease of change in height with addition in SF is greater, which is due to the difference in particle sizes.

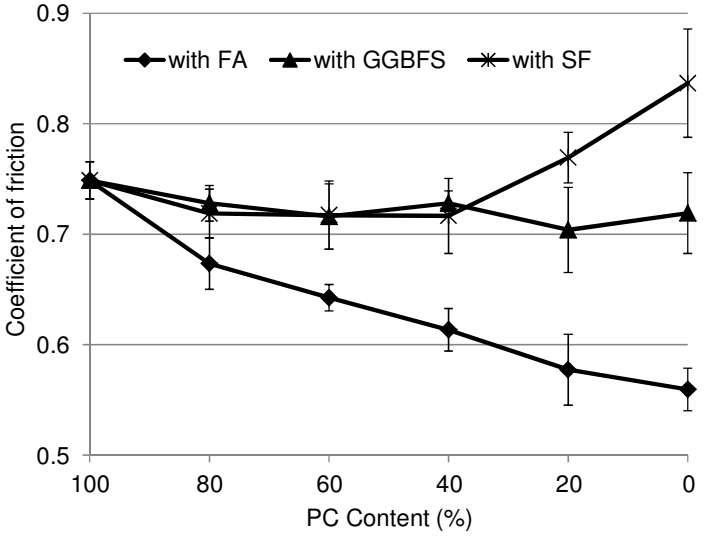

Figure 4.16. Macro-scale coefficient of friction of bulk cementitious materials

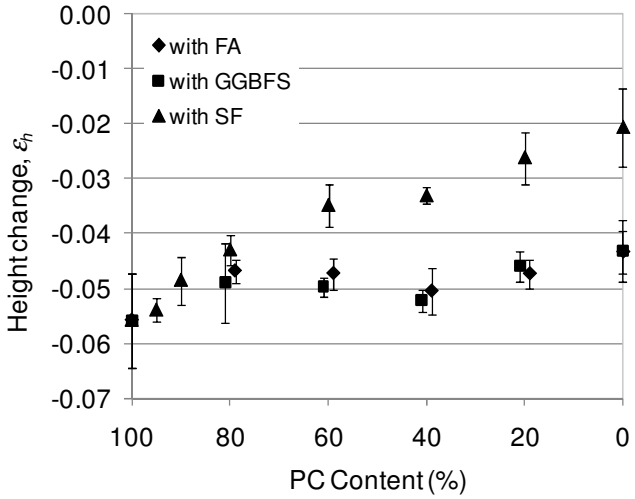

Figure 4.17. Change in height Δh/h0 of cementitious materials under shear at 12.5 mm shear displacement

Comparing the micro-scale coefficient of friction obtained by AFM given in Figure 3.24 and the macro-scale coefficient of friction obtained by direct shear of bulk cementitious material given in Figure 4.16, the micro-scale coefficients of friction are an order of magnitude smaller than the macro-scale coefficients of friction, shown in Figure 4.18. At the macro-scale, contributing factors to the bulk coefficient of friction are particle interlock and

the interfacial shear of sliding particles. Sliding of bulk materials occurs when particle interlocks are overcome by material yield at the points of contact of particles (Bowden and Tabor, 1950 and 1964). The yield stress of a material may be approximated by its indentation hardness (Whitlow, 2001). Nanoindentation of Portland cement phases indicates hardness values of 8.0-10.8 GPa (Velez, et al., 2001). Thus, for a direct shear test with a normal stress of 13.1 kPa, the true contact area between particles may be as little as 1.2×10^{-6} of the superficial area. With the small contact areas and very low loads in the AFM micro-scale coefficient of friction measurements, contact stresses do not exceed sample hardness, minimizing plastic deformation (Bhushan and Sundararajan, 1998). Lack of plastic deformation greatly reduces frictional force, making the micro-scale coefficient of friction much lower than the macro-scale coefficient of friction. It was shown in by Bhushan and Sundararajan that at contact stresses exceeding the material hardness, the coefficient of friction increases towards values comparable to those of macro-scale measurements.

It can also be observed that FA-FA macro-scale coefficient of friction is lower than the PC-PC macro-scale coefficient of friction, while the micro-scale coefficient of friction of PC-PC is lower than micro-scale FA-FA. This may be attributed to the shape of the particles, where FA are spherical and will flow much easier when sheared as a bulk material. In rheology or friction of bulk materials are modeled by particle behavior, the micro-scale coefficient of friction should be used because particle shape and stiffness have separate contributions to the overall macro deformations and stresses (Jones, et al., 2004).

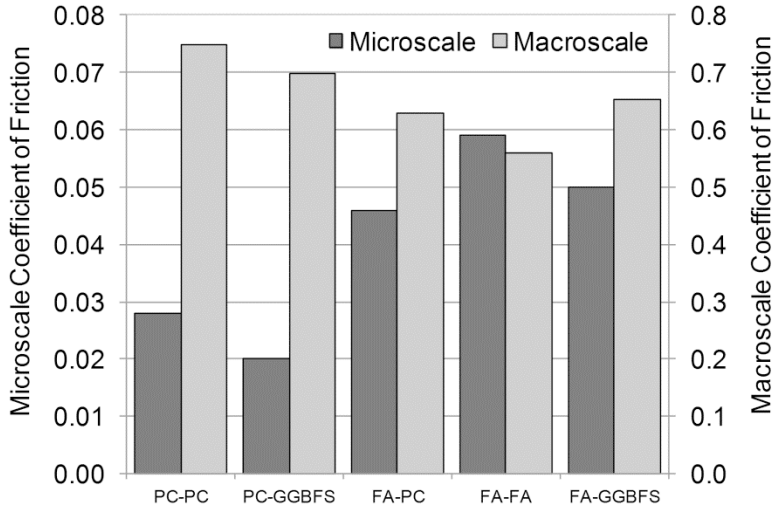

Figure 4.18. Micro- and macro-scale coefficient of friction of cementitious materials

4.5 Rheological Properties of Pastes

This section presents study of the viscosity, yield stress and thixotropy of cementitious pastes. The cementitious materials are unary, binary, ternary and quaternary combinations of PC, FA, GGBFS and densified SF. Water-to-binder ratios were varied from 0.35, 0.45 and 0.55. In the analysis of the rheological properties, statistical models were developed to determine effects of material addition.

4.5.1 Paste Rheology Test Methods

A mixture of cementitious materials (also called binder) and water were prepared to form pastes. The water-to-binder ratios (w/b) were 0.35, 0.45 and 0.55, by weight. The binders were either unary, binary, ternary or quaternary combinations of cementitious materials. Unary pastes were 100% PC or FA or GGBFS with water. Percentages of SF greater than 60% were too viscous to test, thus, a unary SF paste was not presented. Binary pastes were binders with PC and 20, 40, 60 or 80 % FA or GGBFS or SF. When PC was combined with SF, the percentages of SF were 5, 10, 20, 40 and 60 %. Ternary combinations were binders with PC and FA-GGBFS mixes. The combinations FA-GGBFS in percent of total cementitious were 10:10, 15:15, 20:20, 25:25, 30:30, 10:30, 15:25, 25:15 and 30:10. Quaternary combinations were binders with PC and three, five and eight percent SF and

10:10, 15:15, 20:20 and 25:25 % FA-GGBFS combinations. The list of cementitious materials and respective w/b are listed in Table 4.3.

Table 4.3. Paste mixture proportions

w/c	PC	FA	GGBFS	SF	w/c	PC	FA	GGBFS	SF
Unary					Quaternary				
0.35/0.45/0.55	100				0.35	77	10	10	3
0.35/0.45/0.55		100			0.35	67	15	15	3
0.35/0.45/0.55			100		0.35	57	20	20	3
Binary					0.35	47	25	25	3
0.35/0.45/0.55	80	20			0.45/0.55	77	10	10	3
0.35/0.45/0.55	60	40			0.45/0.55	75	10	10	5
0.35/0.45/0.55	40	60			0.45/0.55	72	10	10	8
0.35/0.45/0.55	20	80			0.45/0.55	67	15	15	3
0.35/0.45/0.55	80		20		0.45/0.55	65	15	15	5
0.35/0.45/0.55	60		40		0.45/0.55	62	15	15	8
0.35/0.45/0.55	40		60		0.45/0.55	57	20	20	3
0.35/0.45/0.55	20		80		0.45/0.55	55	20	20	5
0.35/0.45/0.55	95			5	0.45/0.55	52	20	20	8
0.35/0.45/0.55	90			10	0.45/0.55	47	25	25	3
0.35/0.45/0.55	80			20	0.45/0.55	45	25	25	5
0.45/0.55	60			40	0.45/0.55	42	25	25	8
0.55	40			60					
Ternary									
0.35/0.45/0.55	80	10	10						
0.35/0.45/0.55	70	15	15						
0.35/0.45/0.55	60	30	10						
0.35/0.45/0.55	60	25	15						
0.35/0.45/0.55	60	20	20						
0.35/0.45/0.55	60	15	25						
0.35/0.45/0.55	60	10	30						
0.35/0.45/0.55	50	25	25						
0.35/0.45/0.55	40	30	30						

The pastes tested were prepared following ASTM C305 (2011). Immediately after mixing, a sample was poured in a 50 mm diameter by 100 mm high cylinder and tested using an R/S SST2000 Brookfield rheometer with a V30-15 vane spindle. The vane was completely submerged at the center of the cylinder. It was then rotated with an increasing shear rate of zero to 100 s^{-1} in 60 seconds and subsequently decreased to zero s^{-1} within 60 seconds. The shear stress for the applied shear rate was recorded.

The paste viscosity and yield stress were calculated from the down curve of the flow curve. The down curve follows a Bingham model. To calculate for the paste viscosity, a regression line was made from 20 s^{-1} to 80 s^{-1}. The slope of the regression line was the paste viscosity. The zero intercept of the regression line was the calculated yield stress. The paste thixotropy was calculated as the area between the up-curve and down-curve, between the strain rates 20 s^{-1} to 80 s^{-1}.

4.5.2 Results and Discussions

In the analysis of the rheology test results, statistical models were developed for viscosity, yield stress and thixotropy of binary, ternary and quaternary mixes at w/b of 0.35 to 0.55. In the statistical models, up to third order variables and interactions between cementitious materials and w/b were considered. The final models presented below are those with only statistically significant variables. The units of FA, GGBFS and SF are in percent. The statistical program JMP (SAS, 2010) was used for model development and analysis. The R^2 value for each model determines how well the model approximates the given data. The closer the R^2 value is to one, the better the prediction ability of the model.

Binary mixes

All the models in the binary mixtures have an $R^2 \geq 0.94$, indicating a very good fit for the models. In general, the increase in w/b decreases the measured rheological parameters. The results of the binary PC-FA pastes are shown in Figure 4.19. The replacement of PC with FA tends to reduce the viscosity, yield stress and thixotropy of pastes. These trends have been commonly observed and are attributed to its spherical shape (Ferraris et al., 2001). The thixotropy of PC-FA pastes converges at 100% FA at different w/b, which may indicate weak colloidal structure. The statistical models for binary pastes of PC and FA are

$$\begin{aligned}
\eta &= 6.238 - 0.028FA - 20.488(w/b) + 0.051(FA)(w/b) + 16.833(w/b)^2 \qquad R^2 = 0.95 \\
\sigma_0 &= 481.59 - 1.73FA - 1616.22(w/b) + 3.05(FA)(w/b) + 1372.83(w/b)^2 \qquad R^2 = 0.98 \\
A &= 21751.6 - 224.5FA - 83263.0(w/b) + 848.8(FA)(w/b) + 79861.8(w/b)^2 \quad R^2 = 0.98 \\
&\quad - 804.2(w/b)^2(FA)
\end{aligned} \tag{4.7}$$

The models provide average values of viscosity, yield stress and thixotropy as a function of supplementary cementitious material replacement for a w/b in the range of 0.35 to 0.55. Based on the models, viscosity decreases up to 0.010 Pa-s, yield stress decreases 0.05-0.66 Pa and thixotropy decreases 1.0-26.0 Pa/s for every 1 percent increase in FA replacement.

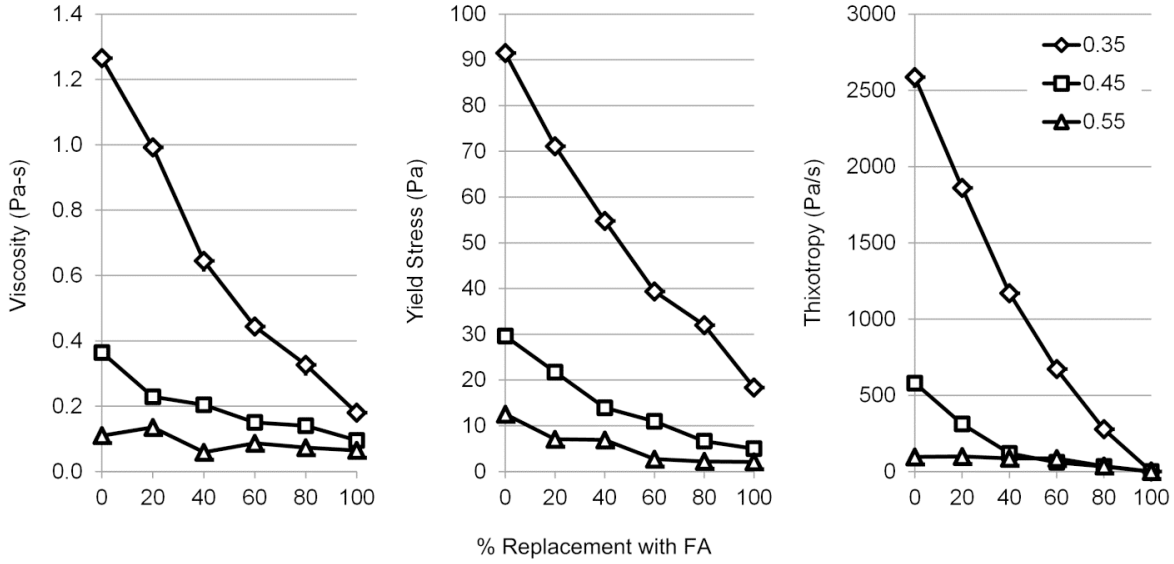

Figure 4.19. Viscosity, yield stress and thixotropy of PC-FA pastes

The results of the binary PC-GGBFS pastes are shown in Figure 4.20. The replacement of PC with GGBFS tends to increase the viscosity, yield stress and thixotropy of pastes. Viscosity increases up to 0.018 Pa-s, yield stress increases up to 0.28 Pa and thixotropy increases up to 25.56 Pa/s for every 1 percent increase in GGBFS. Different from the decreasing trend results in Park, et al. (2005) that used 'roughly spherical' and fine blast furnace slag, GGBFS is angular and has a similar fineness with PC. The models for the rheological properties of PC-GGBFS binary pastes are as follows:

$$\begin{aligned}
&\eta = 13.033 + 0.050GGBFS - 51.934(w/b) - 0.090(GGBFS)(w/b) + 52.083(w/b)^2 && R^2 = 0.96\\
&\sigma_0 = 705.22 + 0.78GGBFS - 2567.48(w/b) - 1.42(GGBFS)(w/b) + 2369.58(w/b)^2 && R^2 = 1.00\\
&A = 36548.6 + 77.9GGBFS - 150196.0(w/b) - 149.3(GGBFS)(w/b) && R^2 = 0.98\\
&\quad + 153200.0(w/b)^2
\end{aligned} \tag{4.8}$$

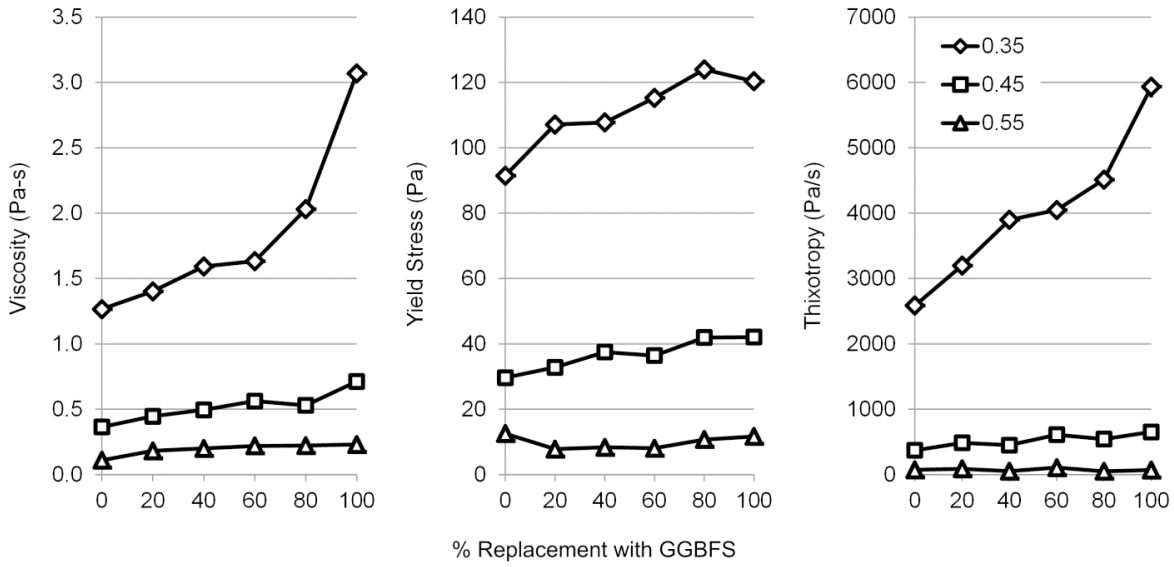

Figure 4.20. Viscosity, yield stress and thixotropy of PC-GGBFS pastes

The results of the binary PC-SF pastes are shown in Figure 4.21. The replacement of PC with SF tends to rapidly increase the viscosity, yield stress and thixotropy of pastes. This is due to the high specific surface of SF particles when it has dispersed in paste (Ferraris et al., 2001). Viscosity and thixotropy increases nonlinearly with increase in SF replacement. Yield Stress increases 1.94 to 4.97 Pa for every 1 percent increase in SF replacement. The models for the rheological properties of PC-SF binary pastes are as follows:

$$\begin{aligned}
&\eta = 13.709 - 0.462SF - 53.723(w/b) + 0.001(SF)^2 + 2.579(SF)(w/b) && R^2 = 0.97\\
&\quad - 3.245(SF)(w/b)^2 + 53.004(w/b)^2\\
&\sigma_0 = 1135.50 + 10.28SF - 15.16SF(w/b) - 4411.37(w/b) + 4268.77(w/b)^2 && R^2 = 0.95\\
&A = 36420.9 + 289.2SF - 574.5SF(w/b) + 1.6SF^2 - 144640.0(w/b) + 142973.0(w/b)^2 && R^2 = 0.98
\end{aligned} \tag{4.9}$$

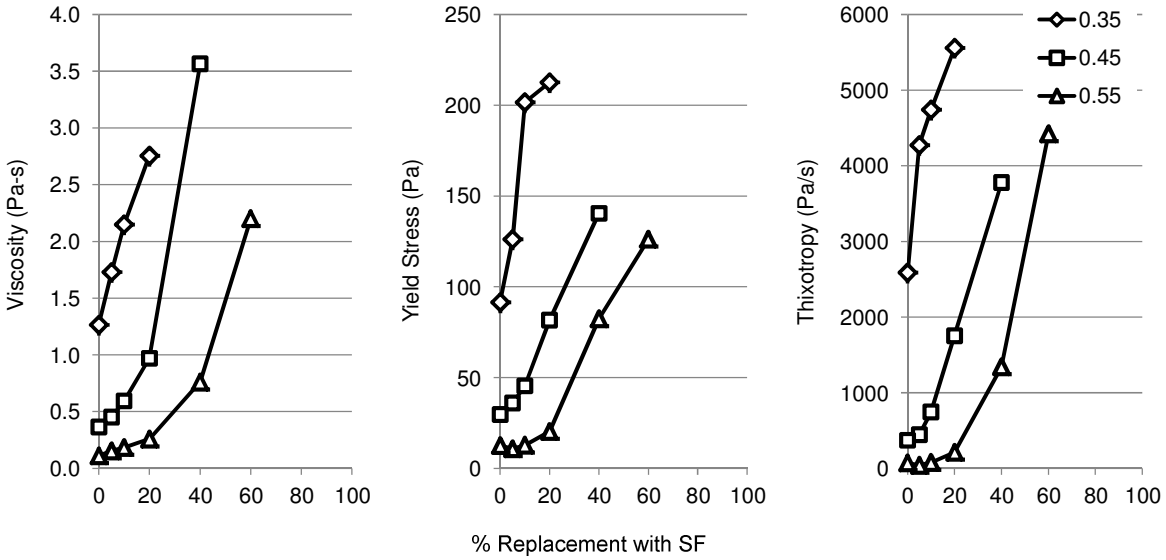

Figure 4.21. Viscosity, yield stress and thixotropy of PC-SF pastes

Ternary mixes

The results for the ternary PC-FA-GGBFS pastes are shown in Figure 4.22 to Figure 4.24 for paste viscosity, yield stress and thixotropy, respectively. The points are result data and the surface plot is generated using the model equations. The models for the rheological properties of PC-FA-GGBFS ternary pastes are as follows:

$$\begin{aligned}
\eta &= 7.994 - 0.041FA + 0.012GGBFS - 28.476(w/b) + 0.074(FA)(w/b) \qquad R^2 = 0.99 \\
&\quad -0.021(GGBFS)(w/b) + 25.651(w/b)^2 \\
\sigma_0 &= 2202.24 - 2.76FA + 0.20GGBFS - 414.88(w/b) + 4.91(FA)(w/b) \qquad R^2 = 0.99 \\
A &= 6104.0 - 21723.6(w/b) - 25.1FA + 19535.4(w/b)^2 + 45.3(w/b)(FA) \qquad R^2 = 0.97
\end{aligned} \tag{4.10}$$

Viscosity decreases up to 0.15 Pa-s per percent increase in FA, and increases up to 0.004 Pa-s for every percent increase in GGBFS. Yield stress decreases 0.06 to 1.04 Pa per percent increase in FA replacement but increases by 0.20 Pa per percent increase in GGBFS. Thixotropy decreases 0.1 to 9.2 Pa/s per 1 percent increase in FA replacement The replacement with GGBFS does not have a significant effect on thixotropy of pastes when combined with FA. The contribution of FA and GGBFS are significant on viscosity and yield stress, while the contribution of FA dominates thixotropy when combined with GGBFS.

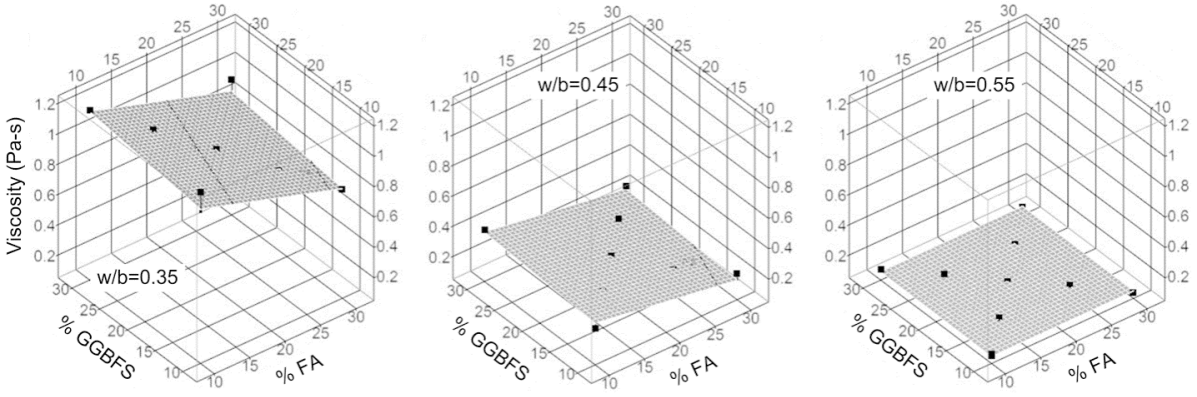

Figure 4.22. Viscosity of PC-FA-GGBFS pastes

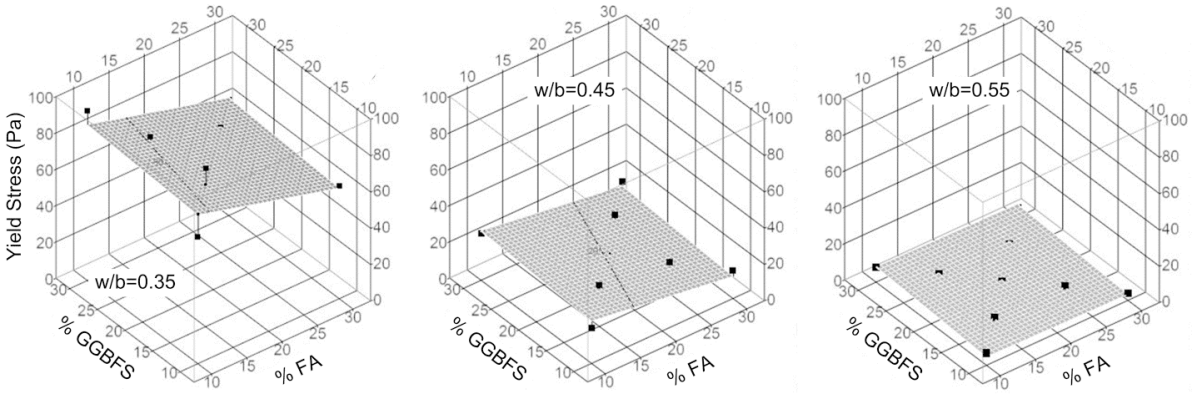

Figure 4.23. Yield stress of PC-FA-GGBFS pastes

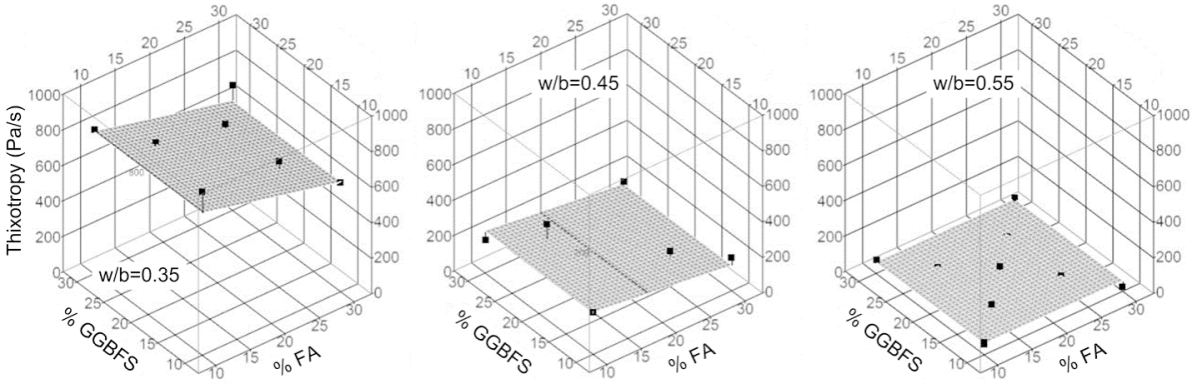

Figure 4.24. Thixotropy of PC-FA-GGBFS pastes

Quaternary mixes

The results of the quaternary PC-FA-GGBFS-SF pastes are shown in Figure 4.25 to Figure 4.27 for paste viscosity, yield stress and thixotropy, respectively. The test were such that FA was equal to GGBFS, thus FA and GGBFS are in one axis in Figure 4.25to Figure 4.27 and are presented as (FA,GGBFS) in the models. The rheology models for quaternary mixes are as follows:

$$\begin{aligned}
\eta &= 6.871 - 0.039(FA,GGBFS) + 0.013SF - 22.384(w/b) + \\
&\quad 0.070(FA,GGBFS)(w/b) + 18.244(w/b)^2 && R^2 = 0.99 \\
\sigma_0 &= 722.83 - 2.92(FA,GGBFS) + 12.09SF - 2615.20(w/b) + \\
&\quad 5.44(FA,GGBFS)(w/b) - 20.77(SF)(w/b) + 2381.44(w/b)^2 && R^2 = 1.00 \quad (4.11) \\
A &= -3145.9 + 19.8SF + 15813.1(w/b) - 18342.0(w/b)^2 && R^2 = 0.88
\end{aligned}$$

Viscosity decreases up to 0.014 Pa-s per percent increase in FA and GGBFS, and increases by 0.013 Pa-s per percent increase in SF. Yield stress increases by 0.06 Pa per percent increase in FA and GGBFS at w/b of 0.55, but decreases from 0.48 to 1.02 Pa per unit increase in FA and GGBFS when w/b is decreased from 0.45 to 0.35. It also increases from 0.66 to 4.82 Pa per unit increase in SF when w/b is decreased from 0.55 to 0.35. Thixotropy increases by 19.8 Pa/s per percent increase in SF. The replacement with FA and GGBFS does not have a significant effect on thixotropy when combined with SF.

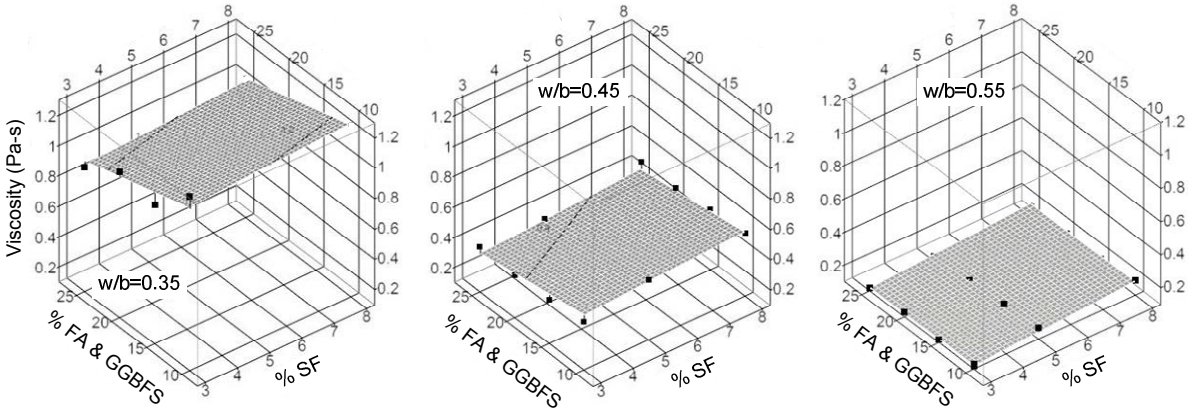

Figure 4.25. Viscosity of PC-FA-GGBFS-SF pastes

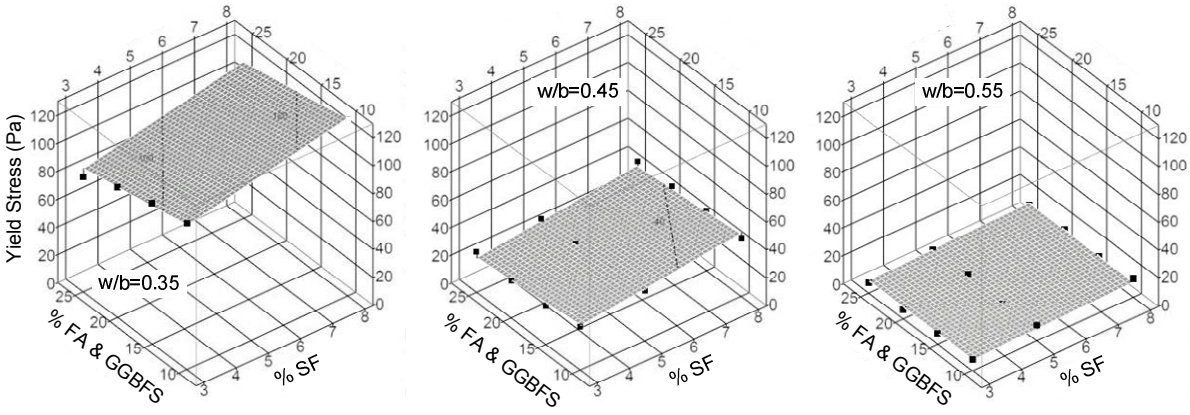

Figure 4.26. Yield stress of PC-FA-GGBFS-SF pastes

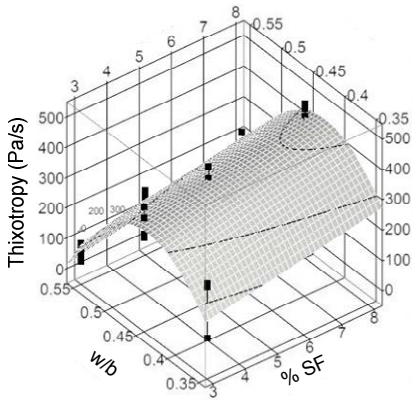

Figure 4.27. Thixotropy of PC-FA-GGBFS-SF pastes

4.6 Relating Paste Viscosity to Dry Properties

Although paste yield stress and thixotropy can be obtained from the rheology tests conducted, these are not presented in this section to focus mainly on correlating paste viscosity to properties of cementitious materials in their dry state. Yield stress and thixotropy are influenced by flocculation of cementitious materials. This phenomenon would not be accounted for when correlating the influence of properties of cementitious materials in their dry state, whereas viscosity measurements are at a state when flocs have been sheared.

For comparing paste rheology results with dry properties, the paste was first pre-sheared before the shear loading. The sample was pre-shear was at a strain rate of 30 s-1 for one minute. The vane was then stopped for one minute. After the rest, the sample was

sheared with an increasing strain rate from 0 to 100 s-1 for one minute. The strain rate was subsequently reduced from 100 to 0 within one minute. The proportions of water-to-binder (w/b) materials were 0.45 and 0.55 by weight.

The viscosity of the pastes for w/b of 0.55 and 0.45 are shown in Figure 4.28 and Figure 4.29, respectively. The viscosity for PC with 5 and 10 % SF are given in Table 4.4. Due to the very high viscosity brought by replacement with SF and the limit of the rheometer, only up to 20 % SF was measured. In both cases, the addition of FA decreases viscosity while the addition of GGBFS or SF increases viscosity. In all cases, a lower w/b has a higher paste viscosity.

As shown in Figure 4.30, an increase in void ratio (Figure 4.7) relates to an increase in viscosity. This indicates that factors that influence the arrangement and packing of particles in its dry state also influences paste rheology. These factors may be particle shape, size, distribution, coefficient of friction and stiffness. Figure 4.31 shows that a significant change in coefficient of friction would influence the viscosity of pastes as in the case of FA replacement. With the replacement of FA, there is a decrease in viscosity as coefficient of friction decreases. Lesser friction between particles would allow the paste to flow easier. For GGBFS replacement, the viscosity seem to decrease with increase in coefficient of friction but it should be noted that the change in coefficient of friction is small (less than 10%) and that viscosity values overlap for a given coefficient of friction. This would mean that factors other than coefficient of friction of GGBFS influence these trends. Figure 4.32 shows decreasing paste viscosity with increasing stiffness modulus. A higher stiffness would reduce collision times or contact durations between particles, thus reducing viscosity. The strong correlation of the coefficient of friction to viscosity compared to stiffness indicates that friction has a greater influence on viscosity for pastes with PC and FA, while the strong correlation of stiffness to viscosity compared to friction indicates that stiffness has a greater influence on viscosity for pastes with PC and GGBFS. The coefficient of friction of dry samples with varying GGBFS and SF content and stiffness modulus for dry samples with varying FA content does not significantly change, thus, not significantly correlating to viscosity.

In its dry state, a blended cementitious material with FA may be easier to transport through pipes compared to a blended cement with GGBFS due to the decrease in coefficient of friction with addition of FA. Since the addition of FA does not change the bulk density of the cementitious materials when consolidated, there may be no change in the mass stored of blended PC with increasing FA, but the amount of cementitious materials that can be stored will decrease with increasing GGBFS addition. Based on the results of paste viscosity, addition of FA will increase fresh concrete flowability, while increase in GGBFS will improve stability against segregation. Based on the correlation of viscosity with void ratio and coefficient of friction, when packing is improved and friction decreases due to blending of cementitious materials, paste viscosity would tend to decrease. Based on the correlation of viscosity to stiffness modulus, when friction does not significantly change such that it affects viscosity, the increase in stiffness modulus would increase paste flowability.

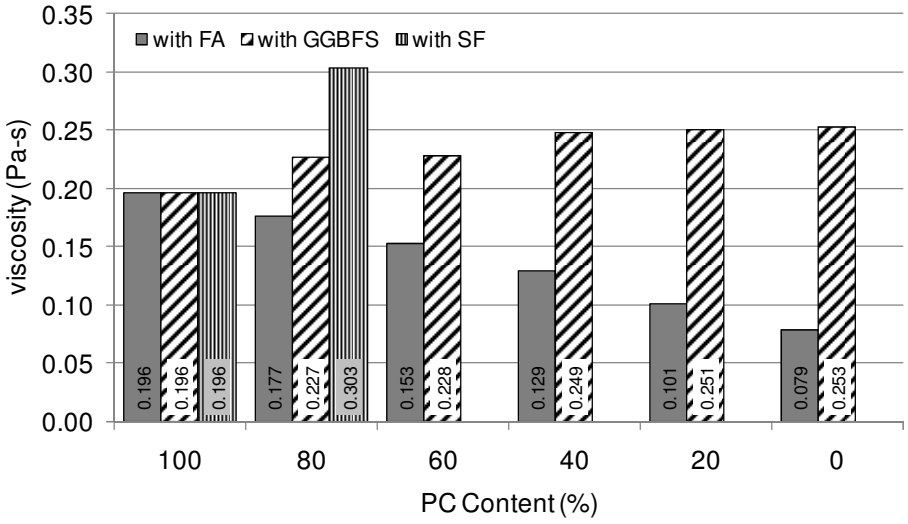

Figure 4.28. Paste viscosity at w/b = 0.55

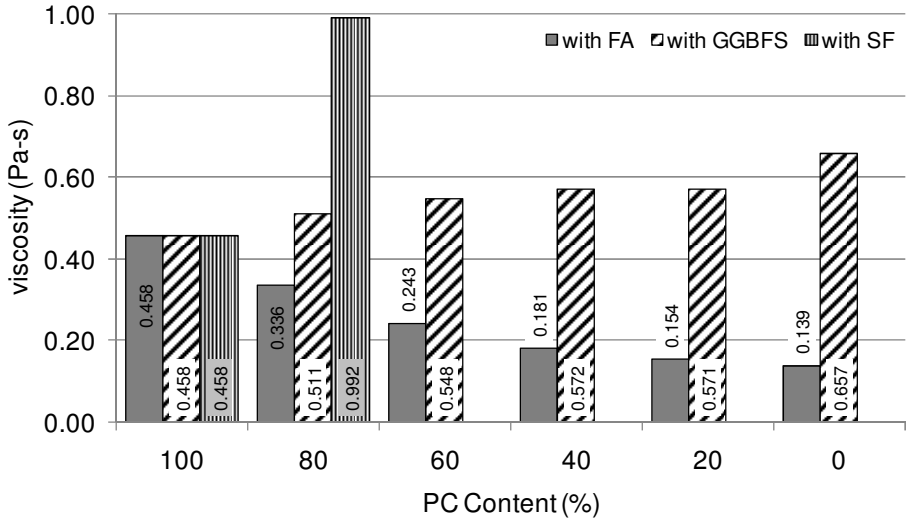

Figure 4.29. Paste viscosity at w/b = 0.45

Table 4.4. Viscosity of pastes of PC with 5 and 10% SF (Pa-s)

PC Content (%)	w/b	
	0.55	0.45
90	0.205	0.682
95	0.181	0.529

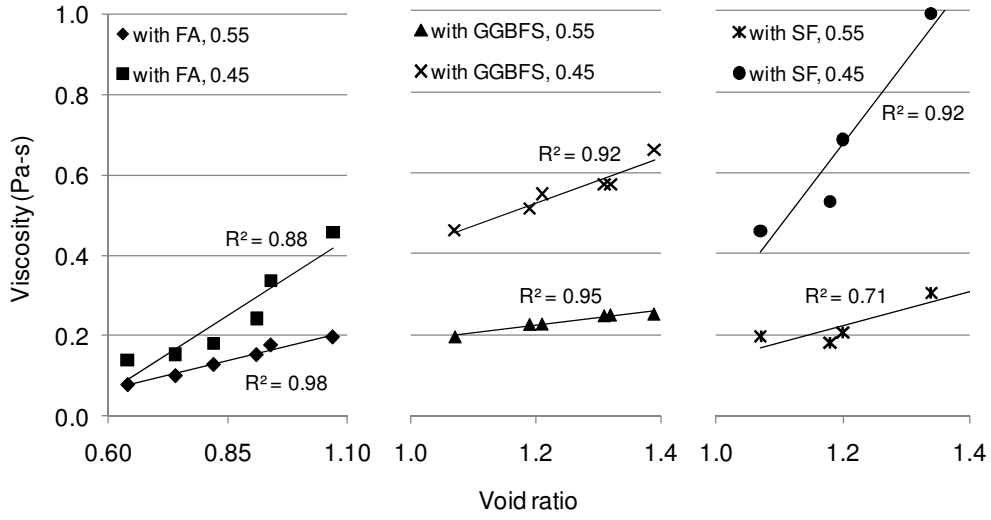

Figure 4.30. Viscosity of pastes vs. void ratio

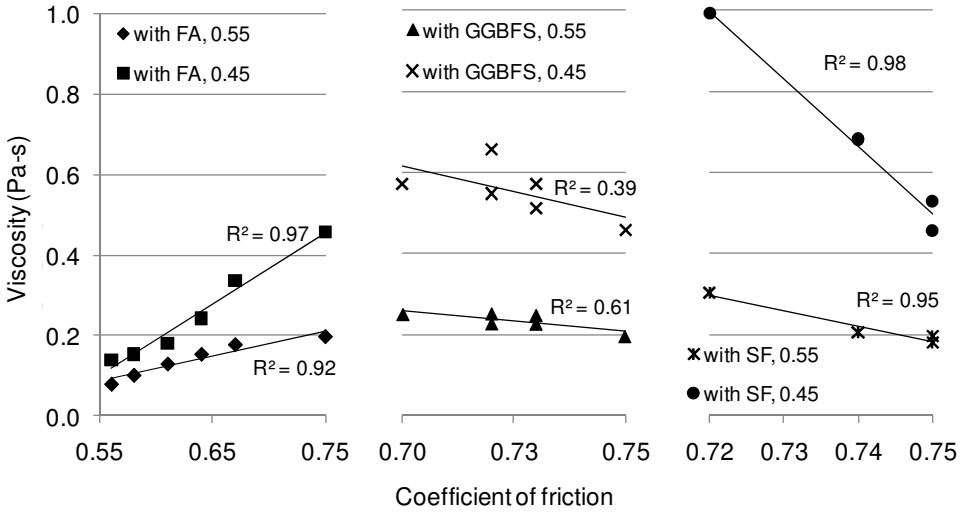

Figure 4.31. Viscosity of pastes vs. coefficient of friction

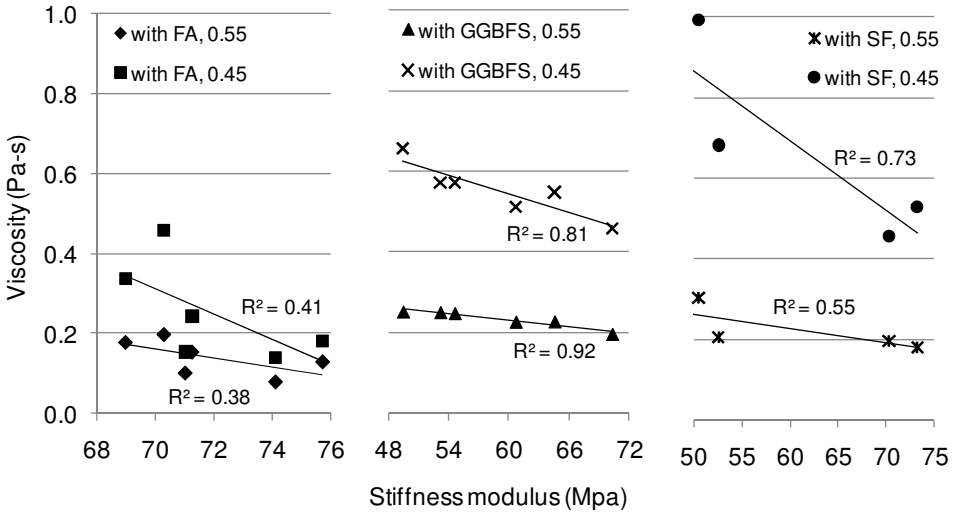

Figure 4.32. Viscosity of pastes vs. stiffness modulus

CHAPTER 5. DEM SIMULATION OF CEMENTITIOUS MATERIALS

5.1 Introduction

Cementitious materials testing in dry state were numerically simulated using DEM. The platform used is MFiX (Multiphase Flow with Interphase eXchanges). MFiX is a general-purpose computer code developed at the National Energy Technology Laboratory (NETL) for describing the hydrodynamics, heat transfer and chemical reactions in fluid-solid systems, Syamlal, et al. (1993). The following theoretical background is based on the DEM formulation for MFiX. The simulations were run on a twelve core Beowulf cluster, 3.0GHz/core.

5.2 Theoretical Background

The soft-sphere model based on the spring-dashpot was first proposed by Cundall and Strack (1978), and was adopted here to model the flow of cementitious materials. In the model, the particles deform and can have enduring, multi-particle contacts, as opposed to hard-sphere model (Allen and Tildesley, 1989) where collisions are binary and instantaneous. The soft-sphere model is suitable for dense systems. Figure 5.1 shows the schematic of two particles i and j in contact. The particles have radius R_i and R_j, and linear and angular velocities $\mathbf{V}_i$, $\mathbf{V}_j$ and $\boldsymbol{\omega}_i$, $\boldsymbol{\omega}_j$, respectively. The positions of the particles are given by $\mathbf{X}_i$ and $\mathbf{X}_j$. The distance between the particle centers is D_{ij}. The normal overlap between the particles is calculated as

$$\delta_n = R_i + R_j - \left|\mathbf{X}_j - \mathbf{X}_i\right| \tag{5.1}$$

The unit vector along the line of contact pointing from particle i to particle j is

$$\eta_{ij} = \frac{\mathbf{X}_j - \mathbf{X}_i}{\left|\mathbf{X}_j - \mathbf{X}_i\right|} \tag{5.2}$$

The relative velocity at the point of contact is

$$\mathbf{V}_{ij} = \mathbf{V}_i - \mathbf{V}_j + (1/2)\left(L_i\boldsymbol{\omega}_i + L_j\boldsymbol{\omega}_j\right)\times\boldsymbol{\eta}_{ij} \tag{5.3}$$

where L_i and L_j are the distance of the contact point from the center of the particles i and j, respectively. They are given by

$$L_i = \frac{\left|\mathbf{X}_j - \mathbf{X}_i\right|^2 + R_i^2 - R_j^2}{2\left|\mathbf{X}_j - \mathbf{X}_i\right|}, \qquad L_j = \left|\mathbf{X}_j - \mathbf{X}_i\right| - L_i \tag{5.4}$$

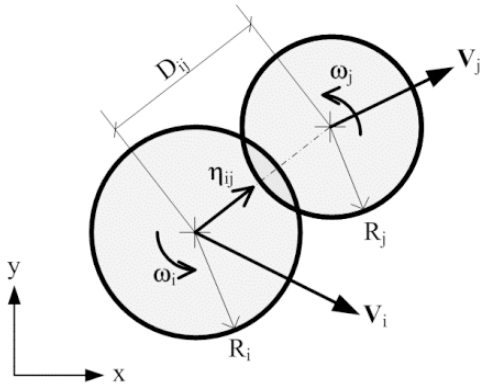

Figure 5.1. Schematic of two particles i and j in contact

The normal velocity $\mathbf{V}_{nij}$ and tangential $\mathbf{V}_{tij}$ components of the contact velocity are

$$\mathbf{V}_{nij} = \mathbf{V}_{ij}\cdot\eta_{ij}\eta_{ij} \equiv \left(\mathbf{V}_i - \mathbf{V}_j\right)\cdot\eta_{ij}\eta_{ij}, \qquad \mathbf{V}_{tij} = \mathbf{V}_{ij} - \mathbf{V}_{ij}\cdot\eta_{ij}\eta_{ij} \tag{5.5}$$

and the tangent to the plane of contact $\mathbf{t}_{ij}$ is

$$\mathbf{t}_{ij} = \frac{\mathbf{V}_{tij}}{\left|\mathbf{V}_{tij}\right|} \tag{5.6}$$

The overlap between the two particles is modeled by a system of springs and dashpots show in Figure 5.2, in both the normal and tangential directions. The normal and tangential stiffness (k_n and k_t) causes rebound. The dashpots provide dissipation of kinetic energy that occurs in inelastic collisions. The dashpot damping coefficients for normal and tangential directions are denoted as η_n and η_t, respectively.

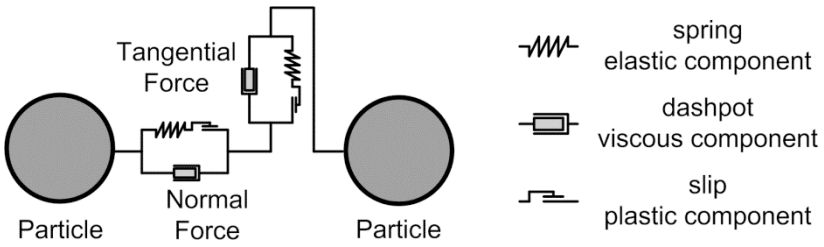

Figure 5.2. Schematic of spring-dashpot system to model particle contacts

The normal and tangential components of the contact force $\mathbf{F}_{ij}$ between particle *i* and *j* at time *t* are composed of the spring force $\mathbf{F}_{ij}^{S}$ and dashpot force $\mathbf{F}_{ij}^{D}$.

$$\mathbf{F}_{nij}(t) = \mathbf{F}_{nij}^{S}(t) + \mathbf{F}_{nij}^{D}(t), \qquad \mathbf{F}_{tij}(t) = \mathbf{F}_{tij}^{S}(t) + \mathbf{F}_{tij}^{D}(t) \tag{5.7}$$

The normal and tangential spring forces are calculated based on the overlap δ_n given in equation (3.1) and δ_t by

$$\mathbf{F}_{nij}^{S} = -k_n \delta_n \boldsymbol{\eta}_{ij}, \qquad \mathbf{F}_{tij}^{S} = -k_t \delta_t \tag{5.8}$$

The tangential displacement at the initiation of contact is calculated as

$$\delta_t = \mathbf{V}_{tij} \min\left(\frac{|\delta_n|}{\mathbf{V}_{ij} \cdot \boldsymbol{\eta}_{ij}}, \Delta t \right) \tag{5.9}$$

and the tangential displacement at time $t + \Delta t$ is

$$\delta_t(t + \Delta t) = \delta_t(t) + \mathbf{V}_{tij} \Delta t - \left(\delta_t(t + \Delta t) \cdot \eta_{ij} \right) \eta_{ij} \tag{5.10}$$

The damping coefficient η and coefficient of restitution *e* in the normal direction are related by

$$\eta_n = \frac{2\sqrt{m_{eff} k_n}\,|\ln e_n|}{\sqrt{\pi^2 + \ln^2 e_n}} \tag{5.11}$$

where $m_{eff} = m_i m_j / (m_i + m_j)$. A similar expression can be written for η_t.

The cohesion model adopted for the DEM simulation is the Hamaker model for van der Waals forces. The force between two spherical particles is given by the expression

$$F_{vdW} = \frac{AR_{eq}}{12D^2} \tag{5.12}$$

where $R_{eff} = R_i R_j / (R_i + R_j)$ is the effective radius, A is the Hamaker constant and D is the surface-to-surface separation distance between two particles. Equation (5.12) approaches infinity as the separation distance approaches zero. The singularity is avoided by introducing a "cutoff" distance D_0. For separation distances below the cutoff distance, the interparticle cohesive force is given by a surface adhesion force (F_{ad}) model

$$F_{ad} = 2\pi R_{eq} \gamma_{ad} \tag{5.13}$$

where γ_{ad} is the surface energy per unit area. When asperities are considered, the contact radius is reduced to the actual contact radius. This can be 30 percent of R_{eq}.

5.3 Numerical Simulation

5.3.1 Single Particle Cohesion

The pull-off force measurement with AFM was simulated using DEM to verify the implementation of van der Waals cohesion model given in equations (5.12) and (5.13). The results are compared to actual AFM results. The DEM model was composed of three particles, and they represented the AFM piezo, the probe cantilever and the attached particle tip, respectively, as shown in Figure 5.3. The boundary below the particles is the sample surface. The particle that models the piezo is moved downward at 1μm/s until the tip particle comes to contact with the sample surface and is move downward further to simulate positive

cantilever deflection of an AFM cantilever. The piezo particle is then moved upward for a piezo withdrawal motion. The particle diameters and densities are 20e-6 m and 3150 kg/m^3, respectively. The time increment is Δt=2.5e-9 s. The stiffness of the model spring particle is 0.31 N/m, the same as spring constant of the probe used in the actual AFM test. The piezo particle and tip particle stiffness are varied to 0.31, 3.1, 31 and 310 N/m to check for convergence. This is done because the stiffness of the actual tip particle is much greater than the stiffness of the actual probe. The Hamaker constant between the tip particle and the sample surface is 0.111e-20 J, which is the calculated Hamaker constant from the AFM test. The Hamaker constant between particles is 1.110e-20 J; this ensures that the particles are glued together. The inner cutoff distance D_0 = 0.165e-9 m. To consider the contact due to asperities from the actual AFM experiment, the contact radius for the tip particle was taken as 33.2 percent of the particle radius.

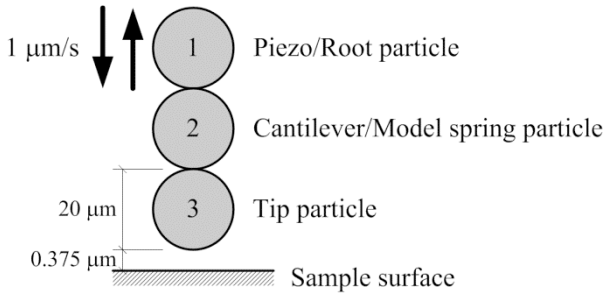

Figure 5.3. Schematic for AFM pull-off deflection DEM model

Four conditions of the pull-off measurement simulation are shown in Figure 5.4 with the typical AFM pull-off force curve. Position a) is the approach while the tip is not yet in contact with the sample surface. At this position the three particles towards the sample surface at a velocity of 0.0001 cm/s. Once the tip particle contacts the sample surface, its velocity is reduced to zero while the piezo particle continues to move without change in velocity. Position c) is where the piezo particle moves away from the sample surface at a velocity of 0.0001 cm/s. The tip particle continues to be in contact with the surface due to adhesion between the tip particle and the surface. At position d), the tip particle had

separated from the surface and the three particles are moving 0.0001 cm/s away from the sample surface.

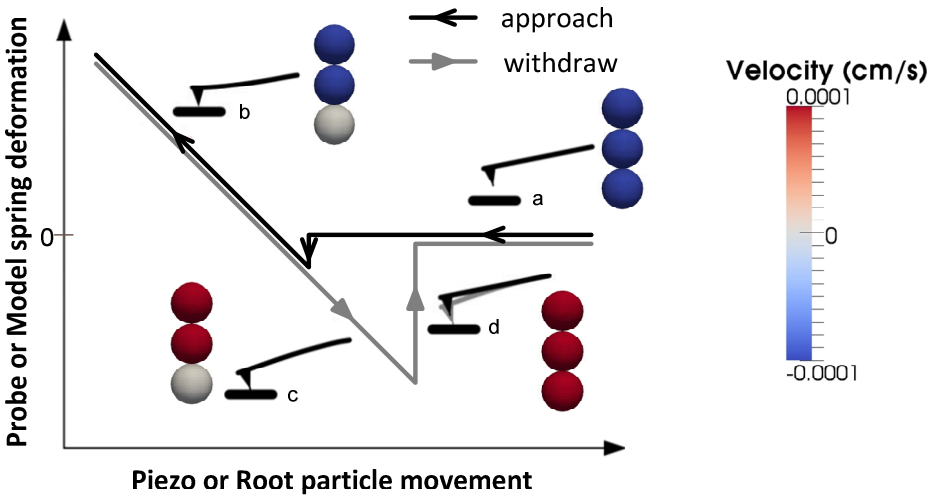

Figure 5.4. Particle velocity diagrams at different positions in the AFM pull-off simulation

The spring deformation in the DEM model is taken as the change in distance between the peizo and tip particles. The simulated force curve with varying piezo and tip stiffness are shown in Figure 5.5. The slope of the simulated force curve is lower than the experiment data because it includes the deformation of the piezo and tip particles. As the piezo and tip particle becomes much stiffer, the DEM force curve converges to the experiment force curve.

The pull-off deflection from the DEM simulations was also obtained with the different particle stiffness. These were plotted against the average pull-off deflection from AFM experiments. The results showed that convergence is achieved with increasing stiffness of piezo and tip particles while maintaining the stiffness of the model spring particle the same as the actual probe stiffness. Based in the results of the simulation, the adhesion behavior of single particle contact can be modeled using DEM. The difference between the particle radius and asperities contact radii is resolved by considering the contact radius as a percentage of the particle radius. This will preserve the actual size and mass of the particle.

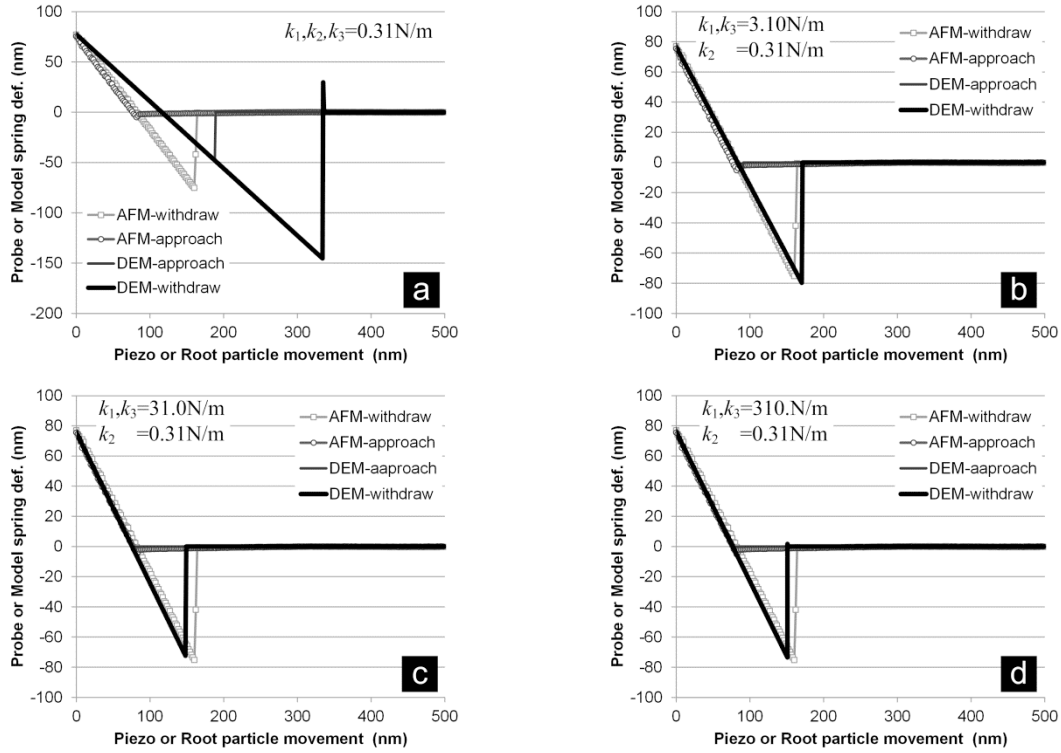

Figure 5.5. Force curves of actual AFM experiment on PC-PC and DEM simulation.

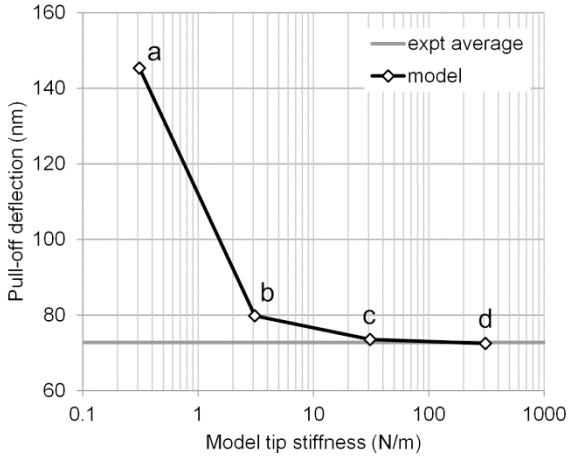

Figure 5.6. Convergence of pull-off deflection simulation

5.3.2 Compression Test

The uniaxial compression experiment discussed in Section 4.3 is simulated with DEM. The box width is 10 cm. It is filled to a height of 3.82 cm to model the cementitious powder in the box. Pouring particles into the box resulted in a lattice arrangement as shown in Figure 5.7. The diameter of the particles is 0.2083 cm. An additional three layers of particles were added to model the plate used in loading. The density of the bulk powder particles is 2.503 g/cm^3. To simulate the increasing load made in the compression experiment, the density of the plate particles were increased to 192.7, 281.1, 480.1, 878.2 and 1655.23 g/cm^3. The compressive stress is computed as the total weight of plate particles divided by the width of the box and particle diameter. The corresponding compressive strain is equal to the change in height divided by the original height of the bulk powder.

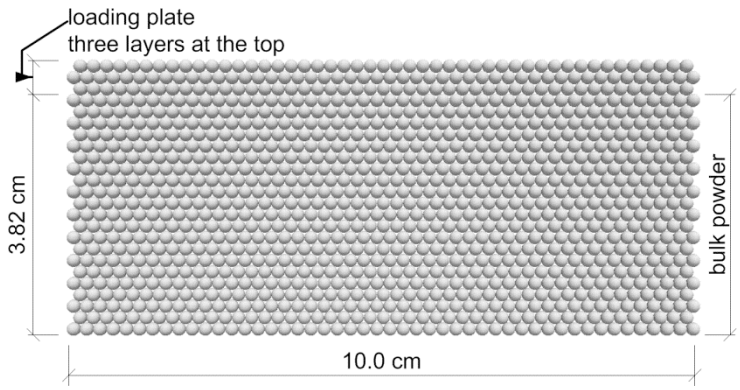

Figure 5.7. Geometry of compression test using DEM

The stiffness of the particles were varied to k = 1, 20, 40 and 60 GN/m. The plot of bulk stiffness (E) vs. particle stiffness (k) is shown Figure 5.8. There is a linear relation between E and k; the bulk stiffness increases 2.79 MPa per MN/m increase in particle stiffness. The plot of compressive stress vs. compressive strain for the DEM simulation with the experimental result for PC compression is shown in Figure 5.9. Based on the relation given in Figure 5.8 and the results of the PC compression, the required particle stiffness was computed and used for simulating the PC compression. The compressive stress vs. strain is

also plotted in Figure 5.9. The simulation curve follows the experiment recompression part (Figure 4.5) of the experiment curve.

Using a particle stiffness k = 40 MN/m, the effect of coefficient of friction on bulk stiffness is plotted in Figure 5.10. The range of friction coefficient is 0.01 to 1.0. The bulk stiffness increases rapidly with the coefficient of friction when it is increased from 0.01 to 0.25 and maintains as bulk stiffness between 120 to 122 GPa after 0.25. The increase in coefficient of friction provides additional resistance to deformation, thus increasing the bulk stiffness. The overall change is 9.2% of the maximum bulk stiffness.

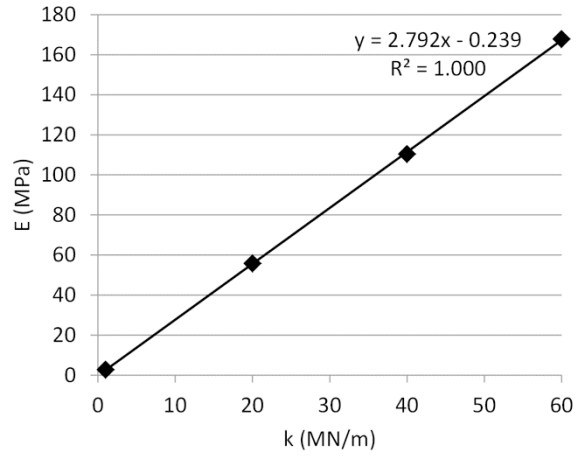

Figure 5.8. Relation of model particle stiffness *k* with measured bulk stiffness *E*

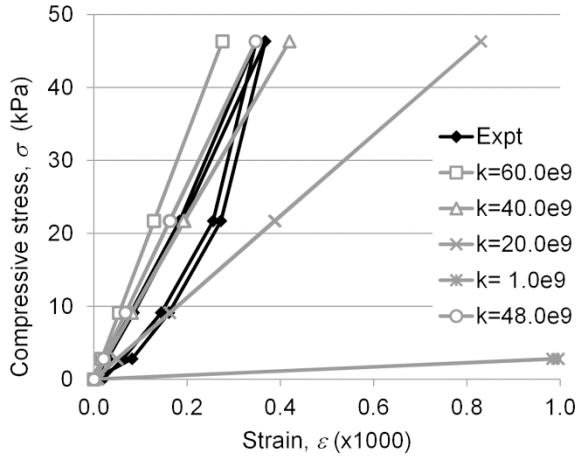

Figure 5.9. Compressive stress vs. strain at different particle stiffness

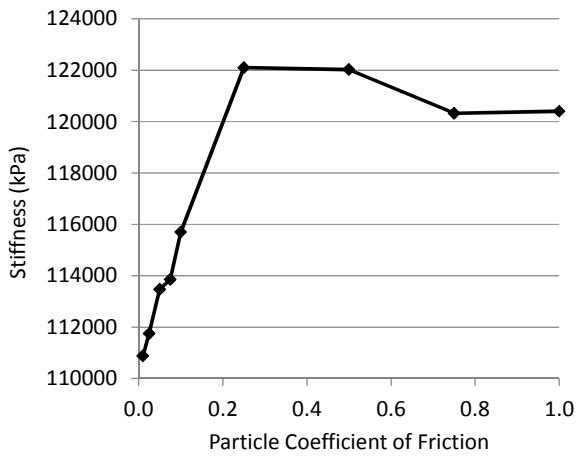

Figure 5.10. Effect of particle coefficient of friction to model bulk stiffness

CHAPTER 6. SUMMARY AND CONCLUSIONS

6.1 Summary

In this study, the rheological properties of cementitious materials have been investigated at the micro- and macro-scales. The cementitious materials used were Portland cement, fly ash, ground granulated slag and silica fume.

At the micro-scale, atomic force microscopy was used to study the adhesion and friction behavior of the cementitious materials in both dry air and fluid environments. For the adhesion study, a method of measurement of Hamaker constant was developed. The adhesion forces between the cementitious materials were also measured. For the friction study, the coefficients of friction between cementitious materials were measured.

At the macro-scale, the cementitious materials were studied in its dry state and paste form. In its dry state, the compression and shear behavior of bulk materials were studied. The effect on compression, recompression, swell, stiffness and coefficient of friction of blended cementitious materials were considered. In paste form, the rheological properties of binary, ternary and quaternary mixture with w/b of 0.35, 0.45, and 0.55 were measured. The influence of supplementary cementitious material replacement was discussed.

Numerical simulationa were also performed on AFM pull-off force measurement in dry air and compression of bulk powders. For the pull-off force measurement simulation validates the implementation of van der Waals model to particle adhesion, considering asperity contact radius. The bulk compression simulation relates particle stiffness to bulk stiffness.

6.2 Findings

The major findings of this study are as follows:

1. Adhesion and Friction at the Micro-scale
    - The method for determining Hamaker constant of cementitious materials contains two steps (1) measuring the adhesion force between the tested material and a selected probe using atomic force microscopy (AFM) and (2) predicting Hamaker constant of

the tested material based on the measured adhesion force and using JKR or DMT models. The consistency of results on reference materials with published results indicates that the present method is valid and reliable. The method has a resolution that can differentiate phases in cement. Sample surface roughness can have a significant effect on the adhesion force measurement. To minimize the effect of surface roughness, samples shall have an RMS less than 20 nm in a 5μm×5μm surface scan.

- Because of double layer effects, Hamaker constants of materials under a water environment cannot be directly measured. Only an effective Hamaker constant can be calculated.
- The adhesion force measurements obtained from AFM are dependent upon the accuracy of experimental measurements for the probe stiffness, probe tip radius, pull-off deflection and cut-off distance. The random errors, or uncertainties, of these measurements should be considered in the calculation of the Hamaker constant.
- Atomic force microscopy can be used for determining the micro-scale friction commercially available cementitious materials. The micro-scale coefficient of friction of tested cementitious materials ranges 0.020 to 0.059. PC-GGBFS had the lowest micro-scale coefficient of friction, while CFA-CFA had the highest.
- The micro-scale surface properties of cementitious materials may affect the micro-scale coefficient of friction as demonstrated by the surface properties of CFA particles. The micro-scale coefficient of friction of CFA with other cementitious materials is higher than the micro-scale coefficient of friction of cementitious materials without CFA.

2. Rheology at the Macro-scale
    - The bulk density of loosely compacted PC is similar to CFA, higher than that of GGBFS. Replacing PC (angular particles) with CFA (spherical particles) reduces the initial void ratio, while replacing PC with GGBFS (angular particles) increases the void ratio of the blended material.
    - Compression behavior of the materials is characterized by the compression, recompression and swell indices as well as stiffness modulus. The indices of PC-CFA

blends do not change with CFA replacement, while the compression indices of PC-GGBFS blends increase with GGBFS replacement.

- The macro-scale coefficient of friction of tested cementitious materials ranges from 0.56 to 0.75. PC-PC has the highest macro-scale coefficient of friction and CFA-CFA has the lowest. The coefficient of friction of PC-CFA and PC-GGBFS blends decreases with CFA or GGBFS replacement, which results in increased flowability of dry PC-CFA and PC-GGBFS blends. Particle shape plays a significant contribution to the macro-scale coefficient of friction. The angular shape has a higher potential for particle interlocking which may contribute to the higher coefficient of friction, while a spherical shape makes particles easier to move and pack.
- In cementitious pastes, replacement with CFA decreases rheological parameter values, while replacement with GGBFS and SF increases rheological parameters. Viscosity and yield stress varies linearly with FA and GGBFS replacement. The viscosity and thixotropy increases quadratically, while yield stress increases linearly with an increase in SF replacement in binary pastes. Rheological parameters change linearly with SF replacement when combined with FA and GGBFS in quaternary pastes. Thixotropy is dominated by FA in ternary pastes and is dominated by SF in quaternary pastes.

3. DEM Simulation
    - The force-curve obtained by AFM can be modeled with DEM using the van der Waals adhesion force model. The contact due to asperities is incorporated by considering the asperities as a percentage of the radius of the contacting particles.
    - The compression behavior and stiffness of bulk cementitious materials can be obtained with DEM simulations. The calculated bulk stiffness has a direct relation to particle stiffness. Based on the relation, particle stiffness can be obtained for a given bulk stiffness.

6.3 Recommendations

The following recommendations are given to improve or extend the present research:

1. Modern concrete often includes chemical admixtures such as water reducers, viscosity and rheology modifiers. These admixtures interact with cementitious materials to change the rheological properties of concrete mixtures (ACI 212.3R-10). The method of sample and probe preparation and measurement of adhesion and friction forces in fluid environments with AFM discussed may be used to study the effects of chemical admixtures at the particle level. The change in adhesion and coefficient of friction can be determined. The force curves from AFM will also give insight into the change in force with respect to distance from the particle. Because of different types of admixtures produced and Portland cements from different manufacturers, incompatibilities have also been reported (Dodson and Hayden, 1989). Mechanisms of incompatibility of admixture to cementitious material may also be studied.
2. The study of the elastic modulus of cementitious particles will contribute to understanding the rheology of cement based materials. The mechanical properties of particles play an important role in paste rheology because of the collisions between particles during shearing. Indentation at the micro-scale is often used on cement hydration products (Mondal, et al., 2006). It may be used to measure the hardness of particles and calculation of elastic modulus. In its fresh state, unhydrated cementitious materials are abundant and have to be considered.
3. The DEM simulations conducted in the present study may be improved by increasing the number of particles in the simulation. This will provide a better representation of the particle interaction in a cement paste system. Because of the irregular shape of Portland cement particles, the representation of these particles may be improved by clumping (Ashmawy, et al., 2003).
4. Further work for the current study is the simulation of wet rheology, i.e. pastes, mortar and concrete mixtures. MFiX is capable of multiphase simulation, DEM as solid particles in a fluid environment. In the simulation of pastes, the DEM particles will represent cementitious materials. The stiffness may be the same as those studied in Chapter 5, and adhesion parameters will be those measured with the AFM in Chapter 3. The fluid phase

will be water. For mortar flow simulations, the solid particles will be fine aggregates and the fluid phase will be cementitious paste. The DEM parameters of fine aggregates are available in literature (Iwashita and Oda, 1998). The viscosity of the paste may be taken from the results of Chapter 4. For the simulation of concrete flow, the DEM parameters for coarse aggregates may be taken from Yan and Ji (2010) and the fluid phase will be mortar, where the viscosity may be from taken from Hu (2005).

REFERENCES

1. Aarons, L. and Sundaresan, S., 2006, Shear Flow of Assemblies of Cohesive and Non-Cohesive Granular Materials, Powder Technology, 169(1):10-21.
2. ACI 212, 2012, Report on Chemical Admixtures for Concrete, ACI 212.3R-10, American Concrete Institute, 38800 Country Club Drive Farmington Hills, MI 48331,U.S.A.
3. Allen, M. P. and Tildesley, D. J., 1989, Computer Simulation of Liquids, Oxford University Press Inc., New York.
4. Anderson, D.M., McFadden, G.B. and Wheeler, A.A., 1998. Diffuse Interface Methods in Fluid Mechanics. Annu. Rev. Fluid Mech. 30:139-165.
5. Ashmawy, A.K., Sukumaran, B., and Hoang, V.V., 2003, Evaluating the influence of particle shape on liquefaction behavior using discrete element modeling, Proceedings of The Thirteenth International Offshore and Polar Engineering Conference, Honolulu, Hawaii, The International Society of Offshore and Polar Engineers.
6. Assaad, J., Khayat, K.H. and Daczko, J., 2004. Evaluation of static stability of self-consolidating concrete. ACI Materials Journal. 101(3):207-215.
7. ASTM C188, 2009, Standard Test Method for Density of Hydraulic Cement, Annual Book of Standards, Vol. 4.01, ASTM International, West Conshohocken, PA.
8. ASTM C204, 2009, Standard Test Methods for Fineness of Hydraulic Cement by Air-Permeability Apparatus, Annual Book of Standards, Vol. 4.01, ASTM International, West Conshohocken, PA.
9. ASTM C305, 2009, Standard Practice for Mechanical Mixing of Hydraulic Cement Pastes and Mortars of Plastic Consistency, Annual Book of Standards, Vol. 4.01, ASTM International, West Conshohocken, PA.
10. Atzeni, C., Massida, L. and Sanna, U., 1985. Comparison between rheological models for portland cement pastes. Cemement and Concrete Research. 15(3):511-519.
11. Badger, D.H., Mette, R. and Rune, M.J., 2004. Rheology of self-compacting mortars – Influence of particle grading. Nordic Concrete Research. No. 26.

12. Banfill, P.F.G., “The rheology of fresh cement and concrete - a review,” Proceedings of the 11th International Congress on the Chemistry of Cement, Durban, South Africa, (Grieve, G., Owens, G., editors). V.1, 2003, pp. 50-62.
13. Banfill, P.F.G., 2003, The rheology of fresh cement and concrete - a review, Proceedings of the 11th International Congress on the Chemistry of Cement, Durban, South Africa, (Grieve, G., Owens, G., editors). 1:50-62.
14. Bergstrom, L., 1996, Hamaker constants of inorganic materials, Advances in Colloid and Interface Science, 70:125-169.
15. Bhattacharya, S.N., Kamal, M.R. and Gupta, R.K., 2008, Polymeric Nanocomposites: Theory and Practice. Hanser Gardner Publications, Inc., Cincinnati, Ohio, USA.
16. Bhushan, B. and Ruan, J.A., 1994, Atomic-Scale Friction Measurements Using Friction Force Microscopy: Part II – Application to Magnetic Media, Journal of Tribology 116(2):389-396.
17. Bhushan, B. and Sundararajan, S., 1998. Micro/nanoscale friction and wear mechanisms of thin films using atomic force and friction force microscopy, Acta Materialia. 46(11):3793-3804.
18. Bosbach, D. and Enders M., 1998. Microtopography of high-calcium fly ash particle surfaces. Advances in Cement Research. 10(1):17-23.
19. Bowden, F.P. and Tabor, D., 1950 and 1964, The friction and lubrication of solids, Parts I and II, Oxford University Press, London.
20. Butt, H.J., Cappella, B. and Kappl, M., 2005, Force measurements with the atomic force microscope:Technique, interpretation and applications, Surface Science Reports 59:1–152
21. Campbell, C.S., 2006, Granular Material Flows – An Overview , Powder Technology, 162(3):208-229.
22. Campbell, C.S., Brennen,C.E., 1985. Computer simulation of granular shear flows. J. Fluid Mech. 151:167–188.
23. Cappella, B. and Dietler, G., 1999. Force-distance curves by atomic force microscopy, Surface Science Reports. 34:1-104.

24. Carpick, R.W. and Salmeron, M., 1997, Scratching the surface: Fundamental investigations of tribology with atomic force microscopy, Chemical Reviews, 97(4):1163-1194.
25. Carpick, R.W., Agraït, N., Ogletree, D.F. and Salmeron, M., 1996, Measurement of interfacial shear (friction) with an ultrahigh vacuum atomic force microscope, J. Vac. Sci. Technol. B 14 (2):1289-2772.
26. Carpinlioglu, M.Ö., Özbelge, T.A. and Oruc, V., 2002, Flow frictional resistance in pneumatic conveying of solid particles through inclined lines, Powder Technology, 125(2-3):292-297.
27. Chia, K.S. and Zhang, M.H., 2004. Effect of chemical admixtures on rheological parameters and stability of fresh lightweight aggregate concrete. Magazine of Concrete Research. 56(8):465-473.
28. Chik Z. and Vallejo, L.E., 2005, Characterization of the angle of repose of binary granular materials, Canadian Geotechnical Journal, 42(2):683-692.
29. Chu, H. and Machida, A., 1996, Numerical simulation of fluidity behavior of fresh concrete by 2D distinct element method. Transactions of the Japan Concrete Institute, 18.
30. Chu, H., Machida, A. and Suzuki, N., 1996, Experimental investigation and dem simulation of filling capacity of fresh concrete. Transactions of the Japan Concrete Institute, 16:9-14.
31. Cleary, P.W., Sinnott, M.D. and Morrison, R.D., 2008, DEM prediction of particle flows in grinding processes, Int. J. Numer. Meth. Fluids, 58:319–353.
32. Coetzee, C.J., Basson, A.H. and Vermeer P.A., 2007. Discrete and continuum modelling of excavator bucket filling. Journal of Terramechanics. 44(2):177-186
33. Coussot, P., 2005, Rheometry of Pastes, Suspensions, and Granular Materials: Applications in Industry and Environment, John Wiley & sons, New Jersey.
34. Cry, M., Legrand, C. and Mouret, M., 2000, Study of the shear thickening effect of superplasticizers on the rheological behavior of cement pastes containing or not mineral additives, Cement and Concrete Research, 30(9):1477-1483.
35. Cundall, P.A., Strack, O.D.L., 1979, A discrete numerical model for granular assemblies. Geotechnique. 29 (1):47– 65.

36. De Larrard, F., 1999. Concrete mixture proportioning – A scientific approach. E & FN Spon.
37. de Larrard, F., Ferraris, C.F. and Sedan, T., 1988. Fresh concrete: A Herschel-Bulkley material. Materials and Structures. 31(211):494-498.
38. Demanet, C.M., 1995. Atomic force microscopy determination of the topography of fly-ash particles. Applied Surface Science, Letter to the editor. 89(1):97-101.
39. Derjaguin, B.V., Muller, V.M. and Toporov, Y.P., 1975, Effect of contact deformation on the adhesion of particles, Journal of Colloid and Interface Science, 53(2):314-320.
40. Di Renzo, A., and Di Maio, F.P., 2004. Comparison of contact-force models for the simulation of collisions in DEM-based granular flow codes. Chemical Engineering Science, 59(3):525–541.
41. Dodson, V.H. and Hayden T.D., 1989, Another look at the Portland Cement / Chemical admixture incompatibility problem, Cement and Concrete Research 19:52 – 56.
42. Drescher, A., 1998, Some aspects of flow of granular materials in hoppers, Phil. Trans. R. Soc. Lond., 356:2649-2666.
43. Eastman, T. and Zhu, D.M., 1996, Adhesion forces between surface-modified AFM tips and mica surface, Langmuir 12:2859-2862.
44. Ferrari, L., Kaufmann, J., Winnefeld, F. and Plank, J., 2010, Interaction of cement model system with superplasticizer investigated by atomic force microscopy, zeta potential, and absorption measurements, Journal of Colloid and Interfacial Science 347:15-24.
45. Ferraris, C.F., 1999. Measurement of the rheological properties of high performance concrete: State of the art report. Journal of Research of the National Institute of Standards and Technology. 104(5): 461-478.
46. Ferraris, C.F., Obla, K.H. and Hill, R., 2001, The influence of mineral admixtures on the rheology of cement paste and concrete, Cement and Concrete Research, 31(2):245-255.
47. Flatt, R.J., 2004, Dispersion forces in cement suspensions, Cement and Concrete Research 34(3):399-408.
48. Fukuhara, M. and Sanpei, A., 1994, High temperature-elastic moduli and internal dilational and shear frictions of fused quartz, Japanese Journal of Applied Physics, 33:2890-2893.

49. Garg, R., Tenneti, S. , Mohd.-Yusof, J. and Subramaniam, S., 2010, Direct numerical simulation of gas-solids flow based on the immersed boundary method, in "Computational Gas-Solids Flows and Reacting Systems: Theory, Methods and Practice.", eds, Pannala, S., Syamlal, M. and O'Brien, T. 245-276.
50. Geiker, M.R., Brandl, M., Thrane, L.N. and Nielsen, L.F., 2002. On the effect of coarse aggregate fraction and shape on the rheological properties of self-compacting concrete. Cement, Concrete and Aggregate. 24(1):3-6.
51. Ghazavi, M., Hosseini, M. and Mollanouri, M., 2008, A comparison between angle of repose and friction angle of sand, The 12th International Conference of International Association for Computer Methods and Advances in Geomechanics (IACMAG), Goa, India.
52. Gjorv M.R., 1998, Workability: an new way of testing, Concrete International, 20(9):57-60
53. Golaszewski, J. and Szwabowski, J., 2004. Influence of superplasticizers on rheological behavior of fresh cement mortars. Cement and Concrete Research. 34(2):235-248.
54. Gu, Z.H., Arnold, P.C. and McLean, A.G., 1992, Consolidation-related bulk density and permeability models for bulk solids, Powder Technology, 72(1):39-44.
55. Gunda, R. and Volinsky, A.A., 2008, Tip-induced calcite single crystal nanowear, Mater. Res. Soc. Symp. Proc. 1049:AA5.15.
56. Heltai L., 2007, On the stability of the finite element immersed boundary method, J. Comput. Struc., 86:598-617.
57. Hertz, H., 1882. Uber die Beruhrung fester elastischer Korper (On the contact of elastic solids. Journal fur die Reine und Angewandte Mathematik. 92:156–171.
58. Hill, J.C., Foulk, J.W. III, Klein, P.A. and Chen, E.P., 2001, A three-dimensional validation of crack curvature in muscovite mica, Computer Methods and Advances in Geomechanics, Desai, et al. (eds), Balkema, Rotterdam, 505-508.
59. Hobbs, D.W., 1976. Influence of aggregate volume concentration upon the workability of concrete and some predictions from viscosity – elasticity analogy. Magazine of Concrete Research. 28(97)191-202.

60. Holland, T.C., 2005, Silica Fume User's Manual, Silica Fume Association, Report No. FHWA-IF-05-016.
61. Hoomans, B.P.B., Kuipers, J.A.M., Briels, W.J. and Van Swaaij, P.M., 1996. Discrete particle simulation of bubble and slug formation in a two-dimensional gas-fluidised bed: a hard-sphere approach. Chemical Engineering Science. 51(1):99–118.
62. Hu, C., de Larrad, F. and Gjorv, O.E., 1995. Rheological testing and modeling of fresh high performance concrete. Materials and Structures/Materiaux et Constructions. 28(175):1-7.
63. Hu, J., 2005, A study of effects of aggregate on concrete rheology, PhD dissertation, Iowa State University.
64. Hu, J., Xiao, X., Ogletree, D.F. and Salmeron, M., 1995, Atomic scale friction and wear of mica, Surface Science, 327:358-370.
65. Image Metrology, 2003, Lyngsø Alle 3A, DK-2970 Hørsholm, Denmark, http://www.imagemet.com/
66. Israelachvili, J., 1991, Intermolecular and Surface Forces, Academic Press Inc., San Diego, CA.
67. Iwashita, K. and Oda, M., 1998, Rolling resistance at contacts in simulation of shear band development by DEM, Journal of Engineering Mechanics-ASCE, 124(3):285-292.
68. Jarnya, S., Roussel, N., Rodtsa, S., Bertranda, F., Leroy, R. and Coussot, P., 2005, Rheological behavior of cement pastes from MRI velocimetry, Cement and Concrete Research 35:1873-1881
69. Johnson, K.L., Kendall, K. and Roberts, A.D., 1971, Surface energy and the contact of elastic solids, Proc. R. Soc. Lond. A. 324:301-313.
70. Jones, M.G. and Williams, K.C., 2003, Solids friction factors for fluidized dense-phase conveying, Particulate Science and Technology, 21:45-56.
71. Jones, R. and Hodges, C.S., 2004, Applications of atomic force microscopy to granular materials: inter-particle forces in air, in Granular Materials-Fundamentals and Applications, S.J. Antony, W. Hoyle and Y. Ding Eds, The Royal Society of Chemistry, 229-254.

72. Jones, R., Pollock, H.M., Geldart, D., Verlinden-Luts, A., 2004. Frictional forces between cohesive powder particles studied by AFM. Ultramicroscopy. 100(1-2):59–78
73. Jyotsna, R. and Kesava Rao, K., 1997, A frictional-kinetic model for the flow of granular materials through a wedge-shaped hopper, J. Fluid Mech., 346:239-270.
74. Karuppiah, K.S.K., Bruck, A.L. and Sundararajan, S., 2009, Evaluation of Friction Behavior and Its Contact-Area Dependence at the Micro- and Nano-Scales, Tribology Letters 36:259–267.
75. Kauppi, A., Andersson, K.M. and Bergström, L., 2005. Probing the effect of superplasticizer adsorption on the surface forces using the colloidal probe AFM technique. Cement and Concrete Research. 35(1):133-140
76. Kaye, G.W.C., 1996, Tables of physical and chemistry constants and some material functions, 13th ed., Longmana Green and Co., Ltd., London.
77. Kennedy C.T., 1940, The design of concrete mixes, Journal of the American Concrete Institute, 36: 373-400.
78. Kim, K.-S., Lin, Z., Shrotriya, P., Sundararajan, S. and Q. Zou, 2008. Iterative control approach to high-speed force-distance curve measurement using AFM: Time dependent response of PDMS example. Ultramicroscopy. 108:911-920.
79. Kosmatka, S.H., Kerkhoff, B. and Panarese, W.C., 2003, Design and Control of Concrete Mixtures, 4th ed, Portland Cement Association, Skokie, IL.
80. Laarz, E., Meurk, A., Yanez, JA., Bergstrom, L., 2001. Silicon nitride colloidal probe measurements: Interparticle forces and the role of surface-segment interactions in polyacrylic acid adsorption from aqueous solution. Journal of the American Ceramic Society 84 (8): 1675-1682.
81. Lachemi, M., Hossain, K.M.A., Lambros, V., Nkinamubanzi, P.C. and Bouzoubaa, N., 2004. Self-consolidating concrete incorporating new viscosity modifying admixtures. Cement and Concrete Research. 34(6):917-926.
82. Lambe, T.W. and Whitman, R.V., 2001, Soil Mechanics, John Wiley & Sons, Inc, 1969.
83. Lesko, S, Lesniewska, E., Nonat, A., Mutin, J.C. And Goudonnet J.P., 2001. Investigation by atomic force microscopy of forces at the origin of cement cohesion. Ultramicroscopy. 86(1-2):11-21.

84. Li, Y., Zhou, S., Yin, J. and Gao, Y., 2004, The effect of fly ash on fluidity of cement paste, mortar and concrete, in International Workshop on Sustainable Development and Concrete Technology, Beijing, China, K. Wang, Ed..
85. Lian, G., Thornton, C. and Adams, M.J., 1993. A theoretical study of the liquid bridge forces between two rigid spherical bodies. Journal of Colloid Interface Science. 161:138–147.
86. Liang, Y., Hilal, N; Langston, P., Starov, V., 2007. Interaction forces between colloidal particles in liquid: Theory and experiment. Advances in Colloid and Interface Science 134-35: 151-166.
87. Limtrakul, S., Rotjanavijit, W., Vatanatham, T., 2007. Lagrangian modeling and simulation of effect of vibration on cohesive particle movement in a fluidized bed. Chemical Engineering Science. 62(1-2):232-245.
88. Littman, H., Morgan, M.H. III, Jovanovic, S.Dj., Paccione, J.D., Grbavcic, Z.B. and Vukovic, D.V., 1995, Effect of particle diameter, particle density and loading ratio on the effective drag coefficient in steady turbulent gas-solids transport, Powder Technology, 84(1):49-56.
89. Lu, G., Wang, K. and Rudolphi, T., 2008, Modeling rheological behavior of highly flowable mortar using concepts of particle and fluid mechanics. Cement & Concrete Composites. 30(1):1-12.
90. Lyklema, J., 2005, Fundamentals of Interface and Colloid Science, Academic Press.
91. Makkawi, Y.T., Wright, P.C. and Ocone, R., 2006, The effect of friction and inter-particle cohesive forces on the hydrodynamics of gas–solid flow: A comparative analysis of theoretical predictions and experiments, Powder Technology, 163(1-2):69-79.
92. Malhotra, V.M. and Metha, P.K., 1996, Pozzolanic and Cementitious Materials, in Advances in Concrete Technology, Volume 1, Gordon and Breach Science Publishers SA.
93. Malone, K.F., Xu, B.H., 2008. Determination of contact parameters for discrete element method simulations of granular systems. Particuology. 6:521–528
94. Marcus, R.D., Leung, L.S., Klinzing, G.E. and Rizk, F., 1990, Pneumatic conveying of solids, Chapman and Hall, London.

95. Mate, C.M., McClelland, G.M., Erlandsson, R. and Chiang, S., 1987, Atomic-Scale Friction of a Tungsten Tip on a Graphite Surface, Physical Review Letters, 59:1942-1945.
96. Matsuoka, H., Ono, K. and Fukui, S., 2010, A new evaluation method of surface energy of ultra-thin film, Microsyst Technol, 16:73-76.
97. Maynard, E.P., 2004, Practical solutions for solving bulk solids flow problems, Cement Industry Technical Conference, IEEE-IAS/PCA.
98. McNeil, L.E. and Grimsditch, M., 1993, Elastic modulus of muscovite mica, J. Phys.: Condens. Matter 5:1681-1690.
99. Mehrotra, A., Chaudhuri, B., Faqih, A., Tomassone, M.S. and Muzzio F.J., 2009. A modeling approach for understanding effects of powder flow properties on tablet weight variability. Powder Technology. 188(3): 295-300.
100. Metha, P.K. and Monteiro, P.J.M., 1993. Concrete – structure, properties and materials, 2nd ed. Prentice Hall.
101. Mills, D., 2004, Pneumatic conveying design guide, second edition, Elsevier Butterworth-Heinemann, Burlington, MA.
102. Mindlin, R.D., Deresiewicz, H., 1953. Elastic spheres in contact under varying oblique forces. Transactions of ASME, Series E. Journal of Applied Mechanics. 20, 327–344.
103. Mishraa, S.R., Kumarb, S., Waghc, A., Rhoc, J.Y. and Ghey, T., 2003. Temperature-dependent surface topography analysis of Illinois class F fly ash using ESEM and AFM. Materials Letters. 57(16-17):2417-2424.
104. Mitchell, L. D., Prica, M., and Birchall, J. D., 1996. Aspects of Portland cement hydration studied using atomic force microscopy. Journal of Materials Science. 31(16):4207-4212.
105. Mittal, R. and Iaccarino, G., 2005. Immersed Boundary Methods, Annu. Rev. Fluid Mech. 37:239-261.
106. Mondal, P., Shah, S.P. and Marks, L.D., 2006. Use of atomic force microscopy and nanoindentation for characterization of cementitious materials at the nanoscale, in Proceedings of ACI Session on “Nanotechnology of Concrete: Recent Developments and Future Perspectives”, Denver, USA.

107. Moreno-Atanasio, R., Xu, B.H., Ghadiri, M., 2007. Computer simulation of the effect of contact stiffness and adhesion on the fluidization behaviour of powders. Chemical Engineering Science. 62(1-2):184-194.
108. Nabeta, K., 1994, Flow simulation of fresh concrete by distinct element method. Proceedings of the JCI, 16(1):479-484 (in Japanese)
109. Nakamura, H., Tokuda, T., Iwasaki, T. and Watano, S., 2007. Numerical analysis of particle mixing in a rotating fluidized bed. Chemical Engineering Science. 62(11):3043-3056
110. Nehdi, M. and Rahman, M.A., 2004. Estimating rheological properties of cement pastes using various rheological models for different test geometry, gap and surface friction. Cement and Concrete Research. 34(11):1993-2007.
111. Nielsen, J., 1998, Pressure from flowing granular solids in silos, Phil. Trans. R. Soc. Lond., 356:2667-2684.
112. Noor, M.A. and Uomoto, T., 1999, Three-dimensional discrete element simulation of rheology tests of self-compacting concrete. Self-Compacting Concrete, Proceedings of the First International RILEM Symposium, Stockholm, 35-46.
113. Oh, S.G., Noguchi, T. and Tomosawa, F., 1999, Toward mix design for rheology of self-compacting concrete, Proceedings of the First International RILEM Symposium on Self-Compacting Concrete, Stockholm, Sweden, 361-372.
114. Pan, R., 1999, Material properties and flow modes in pneumatic conveying, Powder Technology, 104:157-163.
115. Papadakis, V.G., Pedersen, E.J. and Lindgreen, H., 1999. An AFM-SEM investigation of the effect of silica fume and fly ash on cement paste microstructure. Journal of Materials Science. 34(4):683-690.
116. Papo, A., 1988. Rheological models for cement pastes. Materials and Sructures. 21(121):41-46.
117. Park, C.K., Noh, M.H. and Park, T.H., 2005, Rheological properties of cemtitious materials containing mineral admixtures, Cement and Concrete Research, 35(5):842-849.

118. Pendersen, H.G. and Bergström, L., 1999, Forces measured between zirconia surfaces in poly(acrylic acid) sulutions, J. Am. Ceram. Soc. 82 (5):1137-1145.
119. Peskin, C.S., 1972. Flow patterns around heart valves: a numerical method, J. Comput. Phys. 10:252–271.
120. Petersson, O. and Hakami, H., 2001, Simulation of SCC – laboratory experiments and numerical modeling of slump flow and l-box tests. Proc. Of the 2nd Int. RILEM Symp. on SCC, Coms Engineering Corporation, Tokyo.
121. Petersson, O., 2003, Simulation of self compacting concrete – laboratory experients and numerical modeling of testing methods, j-ring and l-box tests. Proceedings of the Third International Symposium on SCC, Reykjavik, Iceland, 202-207.
122. Plassard, C., Lesniewska, E., Pochard I. and Nonat, A., 2005, Nanoscale experimentation investigation of particle interactions at the origin of the cohesion of cement, Langmuir 21:7263-7270.
123. Ploya, G. and Szego, G., 1951, Isoperimetric inequalities in mathematical physics, Princeton Univ. Press, Princton, NJ.
124. Puri, U.C. and Uomoto, T., 2002, Characterization of distinct element modeling parameters for fresh concrete and its application in shotcrete. Journal of Materials Engineering, 14(2):137-144.
125. Ramachandran, V.S., 1995, Concrete admixtures handbook, Properties, Science and Technology, Noyes Publications, Park Ridge, NJ.
126. Rognon, P.G., Roux, J.N., Naaim, M. and Chevoir, F., 2008, Dense flows of cohesive granular materials, J. Fluid Mech. 596: 21-47.
127. Roshavelov, T., 2005. Prediction of fresh concrete flow behavior based on analytical model for mixture proportioning. Cement and Concrete Research. 35(5):831-835.
128. Rosquoet, F., Alexis, A., Kjelidj, A. and Phelipot, A. 2003. Experimental study of cement grout: Rheological behavior and sedimentation. Cement and Concrete Research. 33(5):713-722.
129. Roussel, N., 2006, A thixotropy model for fresh fluid concretes: Theory, validation and applications, Cement and Concrete Research 36:1797–1806.

130. Ruan, J.A. and Bhushan, B., 1994, Atomic-Scale Friction Measurements Using Friction Force Microscopy: Part I - General Principles and New Measurement Techniques, Journal of Tribology 116(2):378-389.
131. Rudzinski, L., 1984, Effect of fly ash on the rheological behavior of cement pastes, Materials and Structures, 17(101):369-373.
132. SAS Institute Inc., 2010, http://www.jmp.com/.
133. SBO Research Technical Support, July 12, 2010, email communications.
134. Scardovelli, R. and Zaleski, S., 1999. Direct Numerical Simulation of Free-Surface and Interfacial Flows. Annu. Rev. Fluid Mech. 31:567-603.
135. Schulze D., 2008, Powders and bulk solids: Behavior, characterization, storage and flow, Springer-Verlag Berlain Heidelberg.
136. Senden, T.J. and Drummond, C.J., 1995, Surface chemistry and tip-sample interactions in atomic force microscopy, Colloids and Surfaces A: Physiocochemical and Engineering Aspects 94:29-51.
137. Sindel, U; Zimmermann, I. 2001, Measurement of interaction forces between individual powder particles using an atomic force microscope. Powder Technology 117 (3): 247-254.
138. Sobolev, K., 2004, The development of a new method for the proportioning of high-performance concrete mixtures, Cement and Concrete Composites, 26(7):901-907.
139. Sun, F. Battaglia and S. Subramaniam, Dynamics and Structures of Segregation in a Dense, Vibrating Granular Bed, Physical Review E, 74(6):061307–13, (2006)
140. Sundararajan, S. and Bhushan, B., 2000, Topography-induced contributions to friction forces measured using an atomic force/friction force microscope, J. Appl. Phys., 88(8):4825-4831.
141. Sundararajan, S. and Bhushan, B., 2001, Development of a continuous microscratch technique in an atomic force microscope and its application to study scratch resistance of ultra-thin hard amorphous carbon coatings, Journal of Materials Research. 16:437-445.
142. Sundararajan, S. and Kanaga Karuppiah, K.S., 2008. Evaluating tribological properties of materials for total joint replacements using scanning probe microscopy in Applied

Scanning Probe Methods VIII, B. Bhushan, H. Fuchs, M. Tomitori (Eds.), Springer-Verlag, New York.

143. Sundararajan, S., Bhushan, B., Namazu, T. and Isono, Y., 2002. Mechanical property measurements of nanoscale structures using an atomic force microscope. Ultramicroscopy. 91(1-4):111-118.
144. Sundaresan, S., Tardos, G. I., and Subramaniam, S., Annual Report on "Rheological behavior of dense assemblies of granular materials", DE-FG26-07NT43070, National Energy Technology Laboratory, Department of Energy, Morgantown, WV
145. Svermova, L., Sonebi, M. and Bartos, P.J.M., 2003. Influence of mix proportions on rheology of cement grouts containing limestone powder. Cement and Concrete Composites. 25(7):737-749.
146. Syamlal, M., Rogers, W. and O'Brien, T.J., 1993, MFIX Documentation Theory Guide, DOE, METC-94, 1004, U.S. Department of Energy.
147. Tabor, D., 1977, The hardness of solids, J. Colloid Interface Sci., 58(2):145-179.
148. Tao, D. Fan, MM. and Jiang, XK., 2009, Dry coal fly ash cleaning using rotary triboelectrostatic separator, Mining Science and Technology, 19:642-647.
149. Tattersall, G.H. and Banfil,l P.F.G., 1983, The rheology of fresh concrete, Pitman, 356.
150. Tibor J. Goda, T.J. and Ebert, F., 2005. Three-dimensional discrete element simulations in hoppers and silos. Powder Technology. 158(1-3):58-68
151. Topcu, I.B. and Kocataskin, F., 1995. A two-phase composite materials approach to the workability of concrete. Cement and Concrete Composites. 17(4):319-325.
152. Torii, A., Sasaki, M., Hane, K. and Okuma, S., 1996, A method for determining the spring constant of cantilevers for atomic force microscopy, Meas. Sci. Technol. 7:179-184.
153. U.S. Geological Survey, Mineral commodity summaries 2011: U.S. Geological Survey, 2011, 198 p.
154. Uchikawa, H., Hanehara, S. and Sawaki, D., 1997. The role of steric repulsive force in the dispersion of cement particles in fresh paste prepared with organic admixture. Cement and Concrete Research. 27(1):37-50.

155. van Oss, H.G., 2009, Minerals Yearbook: Slag, Iron and Steel [Advance Release], U.S. Geological Survey.
156. Velez, K., Maximilien, S., Damidot, D., Fantozzi, G. and Sorrentino F., 2001, Determination by nanoindentation of elastic modulus and hardness of pure constituents of Portland cement clinker, Cement and Concrete Research 31:555-561
157. Vom Berg, W., 1979, Influence of specific surface and concentration of solids upon the flow behavior of cement pastes, Magazine of concrete research, 31(109):211-216.
158. Vu-Quoc, L. and Zhang, X., 1999. An accurate and efficient tangential force–displacement model for elastic frictional contact in particle-flow simulations. Mechanics of Materials. 31:235–269.
159. Walton, O.R. and Braun, R.L., 1986. Viscosity, granular-temperature, and stress calculations for shearing assemblies of inelastic, frictional disks. Journal of Rheology. 30:949–980.
160. Weihs, T.P., Nawaz, Z., Jarvis, S.P. and Pethica, J.B., 1991, Limits of imaging resolution for atomic force microscopy of molecules, Appl. Phys. Lett. 59:3536.
161. Whitlow, R., 2001, Basic Soil Mechanics 4th ed, Pearson Education Ltd., England.
162. Wilson, D.L., Dalal, P., Kump, K.S., Benard, W., Xue, P., Marchant, R.E. and Eppell, S.J., 1996, Morphological modeling of atomic force microscopy imaging including nanostructure probes and fibrinogen molecules, J. Vac. Sci. Technol. B 14 (4):2407-2416.
163. Wilson, K.C. and Addie, G.R., 1997, Coarse-particle pipeline transport: Effect of particle degradation on friction, Powder Technology, 94:235-238.
164. Yan, Y. and Ji, SY., 2010, Discrete element modeling of direct shear test for granular material, 34(9):978-990.
165. Yang, T., Keller, B. and Magyari, E., 2002. AFM investigation of cement paste in humid air at different relative humidities. J. Phys. D: Appl. Phys. (Rapid Communication). 35(8):L25-L28.
166. Yang, T., Keller, B., Magyari, E., Hametner, K. and Günther, D., 2003. Direct observation of the carbonation process on the surface of calcium hydroxide crystals in

hardened cement paste using an Atomic Force Microscope. Journal of Materials Science. 38(9):1909-1916.

167. Yen, T., Tang, C., Chang, C. and Chen, K., 1999, Flow behavior of high strength high-performance concrete, Cement and Concrete Composites, 21(5-6):413-424.
168. Zhang, W., Noda, R. and Horio, M., 2005. Evaluation of lubrication force on colliding particles for DEM simulation of fluidized beds. Powder Technology. 158(1-3): 92-101

APPENDIX A. PULL-OFF FORCE MEASUREMENT DATA

The following are the distribution of data for the AFM probe pull-off deflection during the pull-off force measurements in dry air with Si_3N_4.

Mica/ Si_3N_4

Mean	104.54
Std Dev	4.31
Conf. Int.	1.40

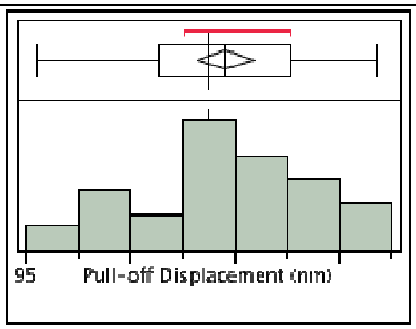

Silica/ Si_3N_4

Mean	30.23
Std Dev	3.89
Conf. Int.	1.17

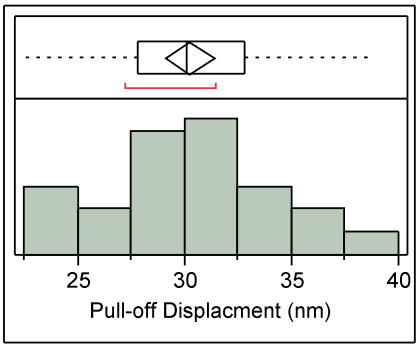

Calcite/ Si_3N_4

Mean	21.02
Std Dev	3.68
Conf. Int.	1.14

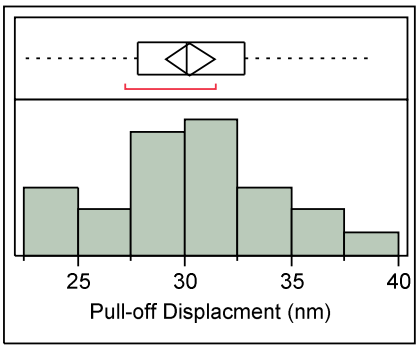

PC/ Si_3N_4

Mean	36.93
Std Dev	3.69
Conf. Int.	1.38

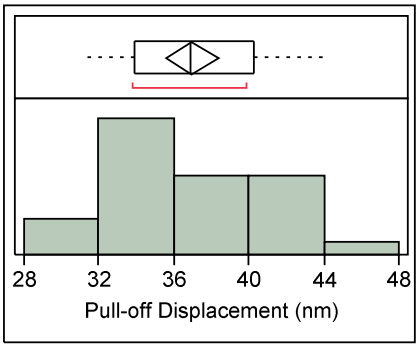

Mean	116.33
Std Dev	16.24
Conf. Int.	6.06

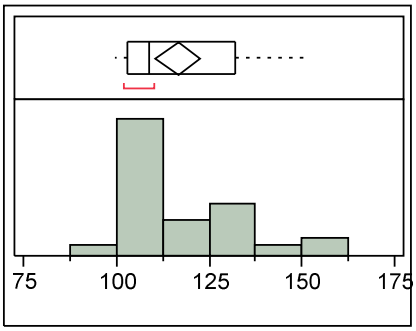

GGBFS/ Si_3N_4

Mean	20.29	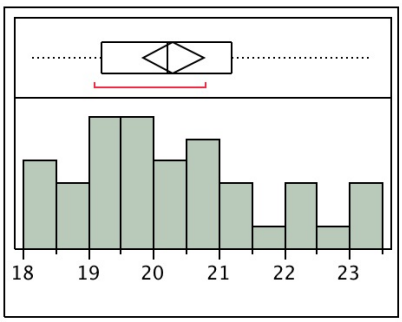
Std Dev	1.44	
Conf. Int.	0.46	

The following are the distribution of data for the AFM probe pull-off deflection during the pull-off force measurements in water with Si_3N_4.

Silica/ Si_3N_4

Mean	3.57	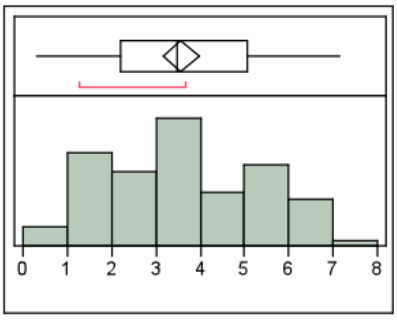
Std Dev	1.72	
Conf. Int.	0.395	

Calcite/ Si_3N_4

Mean	8.02	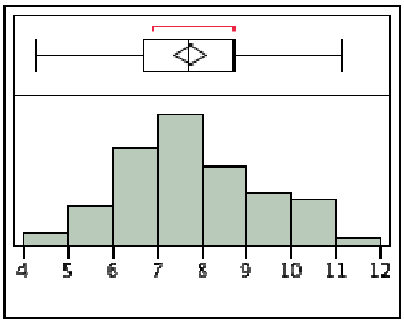
Std Dev	1.58	
Conf. Int.	1.96	

PC/ Si_3N_4

Mean	28.9	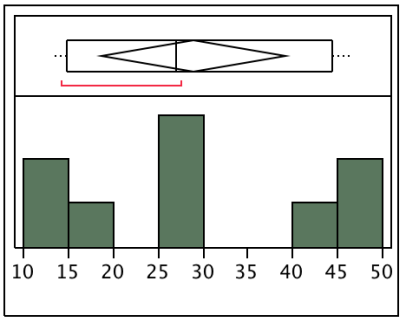
Std Dev	13.39	
Conf. Int.	10.29	
Mean	5.02	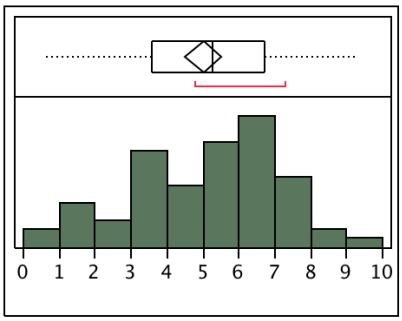
Std Dev	2.04	
Conf. Int.	0.50	

GGBFS/ Si_3N_4

Mean	13.60	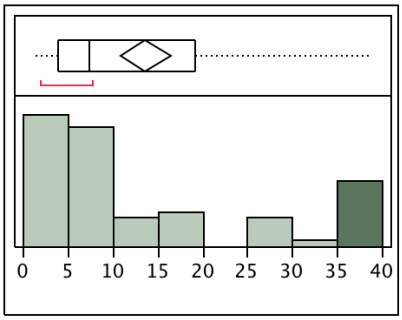
Std Dev	12.43	
Conf. Int.	2.86	

The following are the Hamaker constant and coefficient of friction values of cementitious materials in dry air, water and solution with different pH values.

Table A.1. Hamaker constant ($\times 10^{-20}$ J) of cementitious materials in different environments

	Dry air	pH7	pH8	pH9	pH11	pH13
PC/PC	0.111	0.117	0.072	0.149	0.089	0.048
PC/GGBFS	0.291	0.136	0.076	0.077	0.090	0.240
CFA/PC	0.742	0.105	0.477	0.412	0.542	0.249
CFA/GGBFS	0.473	0.073	0.101	0.246	0.169	0.032
CFA/CFA	0.202	0.220	0.031	0.021	0.014	0.023
FFA1/FFA1	0.161	0.025	0.021	0.024	0.033	0.044
FFA2/FFA2	0.118	0.023	0.028	0.010	0.030	0.013
FFA3/FFA3	0.126	0.064	0.079	0.039	0.021	0.026

Table A.2. Coefficient of friction of cementitious materials in different environments

	Dry air	pH7	pH8	pH9	pH11	pH13
PC/PC	0.028	0.206	0.182	0.189	0.201	0.172
PC/GGBFS	0.020	0.044	0.054	0.044	0.037	0.037
CFA/PC	0.046	0.016	0.017	0.022	0.018	0.044
CFA/GGBFS	0.059	0.059	0.081	0.082	0.063	0.074
CFA/CFA	0.050	0.074	0.074	0.067	0.066	0.080
FFA1/FFA1	0.054	0.020	0.011	0.011	0.013	0.017
FFA2/FFA2	0.044	0.016	0.015	0.022	0.018	0.038
FFA3/FFA3	0.082	0.043	0.040	0.041	0.029	0.031

APPENDIX B. BULK PROPERTIES OF CEMENTITIOUS MATERIALS IN DRY STATE

The following are the tabulated results of the compression and shear testing of bulk cementitious materials in their dry state.

Table B.1. Bulk density of cementitious materials (kg/m^3)

PC Content (%)	with FA	with GGBFS	with SF
100	1513.6	1513.6	1513.6
80	1539.5	1418.1	1237.0
60	1500.4	1384.5	1061.7
40	1506.9	1306.8	933.1
20	1509.4	1285.2	808.2
0	1533.8	1231.9	757.8

Table B.2. Void ratio of cementitious materials

PC Content (%)	with FA	with GGBFS	with SF
100	1.075	1.075	1.075
80	0.944	1.186	1.341
60	0.905	1.211	1.531
40	0.816	1.313	1.687
20	0.738	1.323	1.907
0	0.643	1.395	1.916

Table B.3. Compression index of cementitious materials

PC Content (%)	with FA	with GGBFS	with SF
100	0.128	0.128	0.128
80	0.123	0.137	0.099
60	0.127	0.155	0.085
40	0.124	0.168	0.079
20	0.132	0.174	0.079
0	0.122	0.176	0.062

Table B.4. Recompression index (×1000) of cementitious materials

PC Content (%)	with FA	with GGBFS	with SF
100	0.381	0.381	0.381
80	0.405	0.452	0.563
60	0.385	0.461	0.921
40	0.384	0.532	1.311
20	0.390	0.528	2.055
0	0.389	0.546	2.693

Table B.5. Swell index (×1000) of cementitious materials

PC Content (%)	with FA	with GGBFS	with SF
100	0.350	0.350	0.350
80	0.371	0.415	0.498
60	0.353	0.425	0.822
40	0.332	0.461	1.169
20	0.354	0.473	1.736
0	0.340	0.508	2.020

Table B.6. Stiffness modulus (MPa) of cementitious materials at σ = 52.4 kPa

PC Content (%)	with FA	with GGBFS	with SF
100	150	150	150
80	141	126	105
60	148	123	64
40	158	114	45
20	148	111	30
0	154	103	26

Table B.7. Macro-scale coefficient of friction of bulk cementitious materials

PC Content (%)	with FA	with GGBFS	with SF
100	0.75	0.75	0.75
80	0.67	0.73	0.72
60	0.64	0.72	0.72
40	0.61	0.73	0.72
20	0.58	0.70	0.77
0	0.56	0.72	0.84

APPENDIX C. RHEOLOGICAL PROPERTIES OF CEMENTITIOUS MATERIALS IN WET STATE

The following are tabulated values of viscosities, yield stresses and thixotropies of unary, binary, ternary and quaternary cementitious pastes.

Table C.1. Viscosity, yield stress and thixotropy of PC-FA pastes

% Replacement	Viscosity (Pa-s)	Yield Stress (Pa)	Thixotropy (Pa/s)	w/b
100	0.18	18.35	0.00	0.35
80	0.33	32.00	277.23	0.35
60	0.44	39.38	671.99	0.35
40	0.64	54.78	1169.31	0.35
20	0.99	71.13	1860.00	0.35
0	1.27	91.47	2586.52	0.35
100	0.10	5.01	0.00	0.45
80	0.14	6.65	33.22	0.45
60	0.15	10.99	60.51	0.45
40	0.20	13.93	119.44	0.45
20	0.23	21.75	311.79	0.45
0	0.36	29.63	580.12	0.45
100	0.06	2.12	0.00	0.55
80	0.07	2.21	35.86	0.55
60	0.09	2.71	85.63	0.55
40	0.06	6.92	86.96	0.55
20	0.14	7.05	99.10	0.55
0	0.11	12.54	95.93	0.55

Table C.2. Viscosity, yield stress and thixotropy of PC-GGBFS pastes

% Replacement	Viscosity (Pa-s)	Yield Stress (Pa)	Thixotropy (Pa/s)	w/b
100	3.07	120.37	5934.16	0.35
80	2.03	123.96	4513.00	0.35
60	1.63	115.27	4047.82	0.35
40	1.59	107.75	3897.50	0.35
20	1.40	107.11	3197.22	0.35
0	1.27	91.47	2586.52	0.35
100	0.71	42.06	653.05	0.45
80	0.53	41.93	543.56	0.45
60	0.56	36.42	610.29	0.45
40	0.49	37.50	450.84	0.45
20	0.45	32.80	485.39	0.45
0	0.36	29.63	371.42	0.45
100	0.23	11.68	123.36	0.55
80	0.22	10.72	89.71	0.55
60	0.22	8.05	106.00	0.55
40	0.20	8.33	70.46	0.55
20	0.18	7.78	86.79	0.55
0	0.11	12.54	71.91	0.55

Table C.3. Viscosity, yield stress and thixotropy of PC-SF pastes

% Replacement	Viscosity (Pa-s)	Yield Stress (Pa)	Thixotropy (Pa/s)	w/b
20	2.75	212.58	5557.06	0.35
10	2.15	201.63	4740.74	0.35
5	1.73	126.06	4273.17	0.35
0	1.27	91.47	2586.52	0.35
40	3.56	161.53	3778.04	0.45
20	0.97	81.63	1752.93	0.45
10	0.59	45.40	746.44	0.45
5	0.45	35.99	446.68	0.45
0	0.36	29.63	371.42	0.45
60	2.20	126.20	4421.23	0.55
40	0.76	82.38	1343.22	0.55
20	0.26	20.26	212.12	0.55
10	0.18	12.77	77.73	0.55
5	0.15	10.79	40.05	0.55
0	0.11	12.54	71.91	0.55

Table C.4. Viscosity, yield stress and thixotropy of ternary mixtures

PC%	FA%	GGBFS%	Viscosity (Pa-s)	Yield Stress (Pa)	Thixotropy (Pa/s)	w/b
80	10	10	1.046	82.26	923.1	0.35
70	15	15	0.970	78.35	680.3	0.35
60	30	10	0.769	62.27	613.0	0.35
60	25	15	0.860	64.08	709.2	0.35
60	20	20	0.965	71.82	594.9	0.35
60	15	25	1.070	81.73	765.8	0.35
60	10	30	1.170	93.29	810.6	0.35
50	25	25	0.893	68.21	614.7	0.35
50	25	25	0.891	69.12	689.2	0.35
40	30	30	0.937	64.07	705.6	0.35
40	30	30	0.832	61.24	560.4	0.35
80	10	10	0.287	19.68	236.9	0.45
70	15	15	0.294	22.79	126.4	0.45
60	30	10	0.217	15.57	186.3	0.45
60	25	15	0.223	17.30	198.3	0.45
60	20	20	0.279	18.63	171.8	0.45
60	15	25	0.283	18.62	298.8	0.45
60	10	30	0.388	25.85	186.4	0.45
50	25	25	0.283	20.56	151.8	0.45
40	30	30	0.248	18.64	159.5	0.45
80	10	10	0.113	6.62	71.2	0.55
80	10	10	0.102	6.98	60.6	0.55
70	15	15	0.101	5.72	29.4	0.55
70	15	15	0.115	6.17	79.5	0.55
60	30	10	0.092	3.97	23.7	0.55
60	25	15	0.097	3.43	45.1	0.55
60	25	15	0.106	5.36	65.1	0.55
60	20	20	0.084	5.51	87.8	0.55
60	20	20	0.102	5.59	23.3	0.55
60	15	25	0.091	7.02	58.5	0.55
60	15	25	0.116	6.55	34.7	0.55
60	10	30	0.119	8.35	74.6	0.55
50	25	25	0.095	4.94	52.2	0.55
40	30	30	0.096	5.25	70.3	0.55

Table C.5. Viscosity, yield stress and thixotropy of quaternary mixtures

PC%	FA%	GGBFS%	SF%	Viscosity (Pa-s)	Yield Stress (Pa)	Thixotropy (Pa/s)	w/b
77	10	10	3	1.245	105.39	253.3	0.35
67	15	15	3	1.017	101.17	494.0	0.35
57	20	20	3	1.057	93.97	84.3	0.35
47	25	25	3	0.922	82.72	265.9	0.35
77	10	10	3	0.421	30.96	362.2	0.45
75	10	10	5	0.504	35.71	397.3	0.45
72	10	10	8	0.524	41.86	401.1	0.45
67	15	15	3	0.392	27.75	259.0	0.45
65	15	15	5	0.425	31.46	358.0	0.45
62	15	15	8	0.497	43.55	443.0	0.45
57	20	20	3	0.385	26.73	325.7	0.45
55	20	20	5	0.396	32.64	347.9	0.45
52	20	20	8	0.474	42.12	460.2	0.45
47	25	25	3	0.398	28.75	271.5	0.45
45	25	25	5	0.393	31.47	292.7	0.45
42	25	25	8	0.467	40.89	417.7	0.45
77	10	10	3	0.116	8.08	65.2	0.55
77	10	10	3	0.132	8.00	84.9	0.55
75	10	10	5	0.166	11.32	148.0	0.55
72	10	10	8	0.186	12.74	160.8	0.55
67	15	15	3	0.120	8.17	28.8	0.55
65	15	15	5	0.163	8.08	163.2	0.55
62	15	15	8	0.160	10.40	208.6	0.55
57	20	20	3	0.129	6.67	62.9	0.55
55	20	20	5	0.138	10.32	128.4	0.55
52	20	20	8	0.164	10.92	71.0	0.55
47	25	25	3	0.124	7.45	49.8	0.55
45	25	25	5	0.130	9.53	94.2	0.55
42	25	25	8	0.159	10.48	98.4	0.55

ACKNOWLEDGEMENTS

I would like to sincerely thank Prof. Kejin Wang for her mentorship, support and the opportunity to obtain my second PhD. Working with her on various aspects of concrete research and professional development has been a wonderful experience. I would also like to thank Dr Sriram Sundararajan who had generously included me in his research group and thought me atomic force microscopy, tribology and experimentation at the micro-scale, Dr Shankar Subramaniam for his helpful discussions and suggestions, Prof. Christopher Williams and Prof Vernon Schaefer for their unwavering support and providing valuable suggestions on my research.

I would also like to express my gratitude to lab managers Robert Steffes and Dr Curtis Mosher of the Portland Cement Concrete Research Laboratory and Roy J. Carver Laboratory for Ultrahigh Resolution Biological Microscopy, respectively, for their technical support. I would also like to acknowledge the help of laboratory staffs Jeremy McIntyre and Bryan Zimmerman.

This dissertation would not have been possible without the support of my beloved wife Melissa. Her love, support and understanding have been most valuable during this journey. I would also like to thank my father Angel Lomboy and my sister Ate Russel and brother Angelo for their support. To my fellow research group members these five years, some had left after completing their degree, thank you very much for your help with my research and most of all your friendship.

Finally, I would like to acknowledge the support of the National Science Foundation, Grant No 0927660. Other agencies that supported research projects that enabled me to complete my studies in Iowa State University are the Iowa Department of Transportation and the Federal Highway Administration.